Experimental Study of Diffusive Oil Recovery during Low Salinity Waterflooding and Miscible CO₂ Injection in Sandstones and Shales

Master Thesis in Reservoir Physics

Sunniva Brudvik Fredriksen

Department of Physics and Technology

University of Bergen

November 2014

Executive summary

This experimental thesis presents a study of two diffusive EOR techniques; low salinity waterflooding in 2D sandstone silicon wafer micromodels and miscible CO_2 injection in tight shale core samples. Tests were conducted using both refined oils and crude oil. During low salinity waterflooding, a salinity gradient was set up between low salinity water injected through a fracture and a porous network partially saturated with high salinity brine. Primary drained oil acted as a semi-permeable membrane between the two aqueous phases. As part of a recently started CO_2 project, experiments involved injection of liquid and supercritical CO_2 through tight shale cores to produce oil primarily by molecular diffusion.

Osmotic diffusion in presence of a salinity gradient resulted in increased water flux and oil mobilization, visualized within separate pores and in networks of interconnected pores. Diffusive transport mechanisms were identified as water diffusion through film-flow and osmosis. Two effective processes were observed by the identified mechanisms, 1) water dispersion and water droplet growth and 2) residual oil displacement and mobilization. Water flux through a refined oil membrane increased with brine salinity and decreased with increasing oil carbon number. Highest oil displacement and mobilization was observed with low carbon numbered oil (n-Hexane) and moderate high salinity brine (5%wtNaCl). Water diffusion film-flow caused oil mobilization and redistribution in a continuous crude oil membrane. Expansion in a residual crude oil membrane was caused by osmosis.

Initial oil recovery results during CO_2 injection in tight shales are reported. Shale permeabilities during CO_2 injection were estimated to be of $10^{-2}\mu$D range. Recovery from miscible CO_2 injection in tight shale samples ranged from 76% to 114%OOIP including both refined and crude oil. Recovery exceeded 100%OOIP for the n-Decane experiments due to residual production of immobile crude oil. Errors associated with density of the produced fluids and the porosity estimates of shale cores provide basis for large experimental uncertainties. Dynamic production results showed gas breakthrough after 1 PV CO_2 injected, the effective recovery mechanism being molecular diffusion to displace unrecovered oil. Approximately 60 PVs were injected to obtain a recovery of 71%OOIP using n-Decane. Miscible CO_2 injection could have the potential of producing 100%OOIP given large enough quantities of CO_2.

Acknowledgements

First I would like to thank my supervisors Professor Arne Graue and Associate Professor Martin Fernø at the Department of Physics and Technology, University of Bergen. Thank you for giving me the opportunity to work on interesting and challenging research subjects and for discussions and guidance along the way.

I would also like to thank Phd Candidates Jarand Gauteplass, Lars Petter Hauge and Øyvind Eide. Jarand, thank you for sharing your knowledge and for patience and help in teaching me the works of the Microfluidic Lab. Lars Petter and Øyvind, thank you both for keeping your doors open when I needed help and for answering questions.

A special thank goes to my lab partner and fellow master student Arthur Uno Rognmo! Arthur, thank you for the many hours at the lab doing things we didn't really know how to do, and for eventually solving them. Thank you for taking responsibility and for literally doing all the heavy lifting! I really appreciated our collaborations.

Thanks to all my friends and fellow students at UoB, to the ones who were there from the start and the ones who joined along the way. Thank you all for fun times, laughter and encouragement, and for making these years memorable!

Special thanks go to my sister and mother. Christina, thank you for knowing me and for all the good you bring. Marita, thank you for your endless love, support, and laughter.

Finally, I would like to give my deepest appreciation to my father. Hans Petter, thank you for all the help you have given through all my years of learning and studying. Thank you for all your support, for lifting me up, and for the opportunities ahead. I would not have reached so far if it wasn't for you.

Bergen, November 2014

Table of Contents

4

Introduction

The worldwide energy demand is steadily increasing and fossil fuels are likely to remain among the main energy resources in the foreseeable future. As recovery from conventional high quality resources (*i.e.* sandstones) is declining, the industry turns towards more challenging reserves such as heterogeneous carbonate and tight-shale formations employing unconventional methods. Heterogeneity is an important reservoir characteristic that affects fluid flow through reservoirs and the amounts of residual oil left after production. In conventional recovery by secondary waterflooding, volumes of residual oil may be bypassed by viscous fingering because of unfavorable mobility ratios, or saturations may be trapped by snap-off due to capillary pressure. By secondary gasflooding, gravity segregation or channeling because of the high mobility and low density of gas may result in decreased recovery potential. While only up to 35-55%OOIP (original oil in place) can be produced by conventional methods, another 5-15 % may be recovered at the end of life for an oilfield by unconventional methods (Tzimas *et al.,* 2005).

By unconventional methods, or enhanced oil recovery (EOR) techniques, chemically altered compositions not originally present in the reservoir are injected to increase reservoir displacement efficiency, *i.e.* the recovery factor. Reservoir displacement efficiency is strongly dominated by capillary number (ratio of viscous to capillary forces) and the mobility ratio between the displacing fluids, and is a product of microscopic sweep efficiency and macroscopic displacement efficiency. The microscopic sweep efficiency is the factor that determines the amount of residual oil left after conventional flooding. Increasing the microscopic sweep is one of the main focuses of EOR. In this thesis, the effect of EOR on microscopic sweep has been investigated implementing the unconventional methods of low salinity waterflooding (LSW) in sandstones and miscible CO_2 injection in tight shales.

Where conventional waterflooding use formation brine or seawater to maintain reservoir pressure, LSW will in addition improve microscopic sweep by injecting diluted water concentrations. The low salinity effect (LSE) due to LSW has been widely researched, but because it occurs under a variety of circumstances a theory has so far not been established. The general assumption is that LSW alters the reservoir wettability towards water-wet conditions for favourable recovery, though it has been suggested that more than one underlying mechanism may be present. Based on the results provided by the LSE visualisation study performed by Emadi and Sohrabi (2013), and the work put forward by Sandengen and Arntzen (2013) on osmosis, it is suggested that osmotic diffusion may be one possible mechanism contributing to the LSE. To investigate the effect of osmosis during LSW, micro-scale visualisation is required to identify and observe pore level fluid-fluid interactions and displacement processes in the presence of an osmotic gradient. The experiments were conducted at the Microfluidic Laboratory at the Dept. of Physics and Technology, University of Bergen (UoB), using silicon wafer micromodels representing a porous media. As the majority of experiments conducted on LSW are based on core flooding of sandstone, the micromodels were constructed based on a thin section of Berea sandstone with 2D replicated pore structures and flow paths for micro-scale visualisation.

Implementing CO_2 gas under miscible conditions has been extensively studied and applied in field recovery for over 40 years. The majority of the EOR projects in carbonates and other rocks (*e.g.* shale) have been studied based on CO_2 injection. Ongoing research at the UoB Dept. of Physics and

Technology focuses mainly on the implementation of CO_2 gas for EOR and for carbon storage during production. In miscible CO_2 injection, CO_2 will mix with resident oil by molecular diffusion promoting oil swelling and oil mobilisation. Results have been successful from both simulations and experimental studies of shale. Core-scale experiments were hence conducted at the UoB Dept. of Physics and Technology using reservoir core samples of low porosity, low permeable shale (tight shale). By inducing CO_2 in a miscible injection scheme, potential oil recovery was quantified and flow capacity was estimated.

1 Reservoir Scaling Techniques

The growing oil and gas industry is associated with large investments towards the development and operation of world hydrocarbon resources. It is an overall requirement that operations are carried out in a cost-effective, reliable and sustainable manner. One side of today's international oil business focuses on the complex and hard to develop offshore resources often located far from land and kilometers below the seabed, e.g. North Sea fields. Another focus is the situation in North America, where production of unconventional land-based oils is reshaping the way oil is transported, stored and marketed (IEA, 2013). A considerable amount of this new oil is coming from the US onshore tight shale formations and Canadian oil sand reservoirs.

Challenges like those mentioned above, has led the industry to engage in research and development programs using suitable scaling techniques to uncover the underlying mechanisms of reservoir management. The objective of the investigations is to provide insight into the strengths and weaknesses of different recovery parameters (Zitha *et al.,* 2011). The analyses range from pore to field scale and involve experimentation and modelling (*cf.* Figure 1.1). Fluid properties, reservoir transport and recovery mechanisms are simulated and investigated at controlled conditions to describe the complexity of field scale flow. One can for example:

- Study flow on a microscopic scale to visualize fluid-fluid interactions in different reservoir rocks.
- Analyze the effect of single parameters (*e.g.* pressure and temperature) on flow and recovery potential.
- Assess the impact of structural heterogeneities and displacement behaviour on flow and recovery.
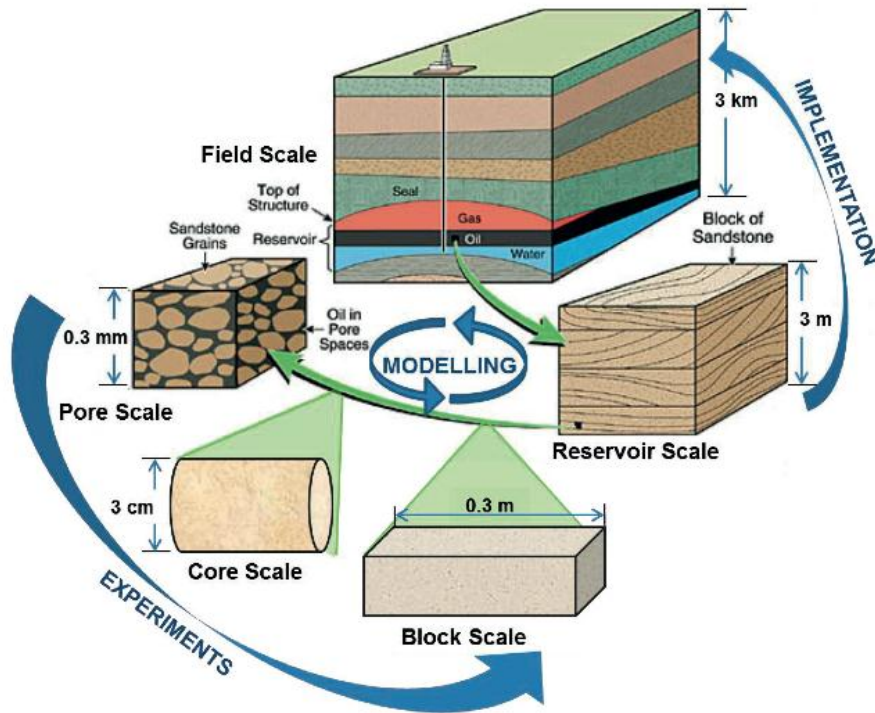
Figure 1.1 - Various scaling techniques used in petroleum research (Brattekås, 2014). Field scale conditions are sized down to reservoir scale conditions where block and core samples are drilled out for study in laboratories. Experimental results can be validated in simulation studies and implemented back into reservoir and eventually field scale operations.

Upscaling is defined as the bridging of different scaled measurements from laboratory pore, core and block experiments to reservoir conditions (Zitha *et al.,* 2011). Field pilots are carried out through upscaling and factors such as well location and other strategic measures are evaluated further through field trials.

Silicon micromodels and reservoir core samples are used in this thesis to investigate the effect of diffusive mechanisms during oil recovery. The micromodels represent a 2D porous media of Berea sandstone for visualizing pore scale mechanisms, such as fluid distribution and displacement processes. Reservoir shale samples are used with miscible CO_2 injection to investigate flow capacity, displacement and oil production in tight shale formations.

2 Fluid Flow and Oil Recovery

Hydrocarbon deposits are found in a variety of formations (*e.g.* clastic sandstone, fractured carbonates, and low permeable shale), where chemical and physical properties such as density, viscosity, pressure, volumes and temperatures vary over a wide range. Primary recovery methods in hydrocarbon formations are based on the presence of internal energy in form of expanding gas-cap or active aquifer. Within the petroleum industry the term conventional recovery refers to oil and gas produced from hydrocarbon resources depleted by such natural drive mechanisms. Conventional recovery is also related to secondary production where the driving force to reservoir pressure maintenance is re-injecting naturally occurring fluids such as water or natural gas back into the reservoir. However, at the end of conventional recovery, a majority of the oil and gas resources remain trapped or bypassed within the reservoir.

Reservoirs suitable for conventional recovery have a sufficient porosity and permeability to hold and transmit oil and gas, sealed off by an impermeable cap rock (*i.e.* heterogeneous reservoirs). Unconventional reservoirs are hence formations with low permeability where oil and gas are trapped in the media and natural drive mechanisms have little or no effect on production (*i.e.* tight shale reservoirs).

To improve reservoir efficiency from conventional and unconventional reserves, unconventional recovery methods, or EOR methods, have become increasingly applied by the oil and gas industry. If positive returns can be achieved in terms of production and finance, the injection of chemically altered compositions for EOR is introduced, adding among others surfactants or polymers to the reservoir fluids. Alternative EOR methods by diffusive oil recovery techniques have gained popularity in recent years, and low salinity waterflooding and miscible CO_2 injection are among them.

2.1 Heterogeneous Reservoirs

All conventional reservoirs (*i.e.* sandstones and carbonates) are to some degree heterogeneous. Reservoir heterogeneity is defined as variations in reservoir properties related to space, meaning that petro-physical variables such as permeability, porosity, and fluid saturation vary across the formation (Ahmed, 2006). If reservoirs were homogeneous, measuring a reservoir property at one location would describe the behaviour of that property across the entire formation.

Heterogeneous reservoirs can be divided into three types, 1) naturally fractured reservoirs dominated by fracture systems and conductive flow paths, 2) layered reservoirs with large extensions of different permeability beds with or without communication, and 3) reservoirs with random heterogeneities in which two or more types of porosity may be evident (Latil, 1980). The recovery performance in heterogeneous reservoirs is reduced in presence of high permeable zones or fractures affecting fluid flow, leading to early breakthrough and bypassing of OOIP.

2.1.1 Water -and gasflooding

Reservoir displacement efficiency E determines oil recovery for any given displacement process (*i.e.* water -or gasflooding), and is the product of microscopic sweep efficiency E_D and macroscopic displacement efficiency E_{vol},

$$E = E_D \cdot E_{vol}$$

(2.1)

The macroscopic displacement efficiency E_{vol} is a combination of both areal E_A and vertical E_V sweep, and is highly affected by heterogeneities and fluid mobility (Skarestad and Skauge, 2012). Microscopic sweep estimates how well the displacing fluid contacts OOIP and determines the amount of residual oil. The higher the residual oil at the end of primary and secondary recovery, the more attractive the application of EOR techniques.

Waterflooding

Secondary recovery by waterflooding provides pressure support to the reservoir and displaces oil towards production. Waterflooding is preferred in cases where the mobility ratio is favourable, meaning that the mobility of the injected water is lower than the displaced oil (Latil, 1980). This prevents early water-breakthrough due to viscous fingering, and increases the macroscopic displacement efficiency.

In water-wet reservoirs, *i.e.* where water preferentially coats the formation surface, waterflooding is especially efficient due to spontaneous imbibition (Latil, 1980). This is important in naturally fractured or layered reservoirs as it induces cross-flow between high -and low permeability zones. The water invades less permeable regions due to the water-wet nature of the formation surface and displaces oil in the presence of a positive capillary pressure. However, if the capillary pressure is too high the consequence may be trapping or bypassing, reducing the microscopic sweep efficiency, *cf.* Figure 2.1. A uniform front needs to be maintained between the displacing fluids for favourable recovery.
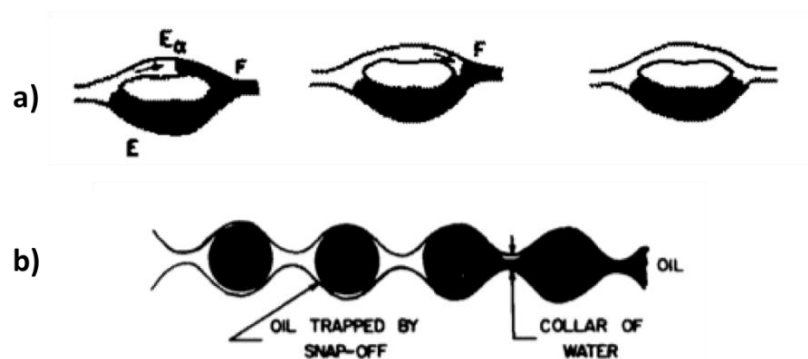

Figure 2.1 - Residual oil saturation by bypassing and snap-off modified from (Chatzis et al., 1983). a) The wetting phase in the small channel bypasses oil in the larger pore due to a higher capillary pressure, b) The wetting phase snaps off isolated oil droplets within pores due to a high capillary pressure at pore throats. Oil droplets become immobile.

Gasflooding

Gasflooding for pressure support and oil recovery takes place in the existing gas-cap or directly in the oil zone. By injecting natural or recycled gas into the original gas-cap, reservoir pressure is maintained as the gas-cap expands. Oil is recovered as gas is forced into the oil zone (Latil, 1980). The gasflooding process can be either miscible or immiscible (Terry, 2001). In most cases, miscible gas injection is used to increase the microscopic displacement efficiency when mixing with reservoir oil. However, using high mobility gas in heterogeneous formations may result in gravity segregation reducing the displacement efficiency.

2.1.2   Factors controlling fluid flow

During immiscible (water or gas) or miscible (gas) displacement, reservoir heterogeneity in combination with viscous, capillary and gravitational forces will influence macroscopic displacement and microscopic sweep. The relationship between the acting viscous -and capillary forces is defined by a capillary number N_C characterizing the amount of non-wetting (residual oil) -and wetting saturation (water) in terms of flow properties (Zolotukhin and Ursin, 2000). The dimensionless capillary number is given as,

$$N_C = \frac{v_i \mu_i}{\sigma_{ij} \cdot cos\theta}$$
(2.2)

Where subscripts i and j denotes displacing and displaced fluid respectively, v is the fluid rate $[ml/s]$, μ is the viscosity $[Pa \cdot s]$, σ is the interfacial tension between the two fluids, and θ is the wetting angle. In Equation 2.2, the term $v \cdot \mu$ represents the viscous forces of the displacing fluid, while the denominator $\sigma \cdot cos\theta$ is related to the capillary forces entrapping residual oil. An increase in capillary number by either decreasing the capillary forces (increasing microscopic sweep) or increasing the viscous forces (increasing macroscopic displacement) will contribute to higher reservoir displacement efficiency.

The effect of capillary number on residual oil and water saturation is shown by the capillary de-saturation curve in Figure 2.2. To reduce the residual non-wetting phase, the critical non-wetting capillary number has to be increased. By introducing chemicals not initially present in the reservoir the capillary number can be raised by lowering the interfacial tension (injecting surfactants or miscible CO_2), or by increasing the viscosity (addition of polymers).
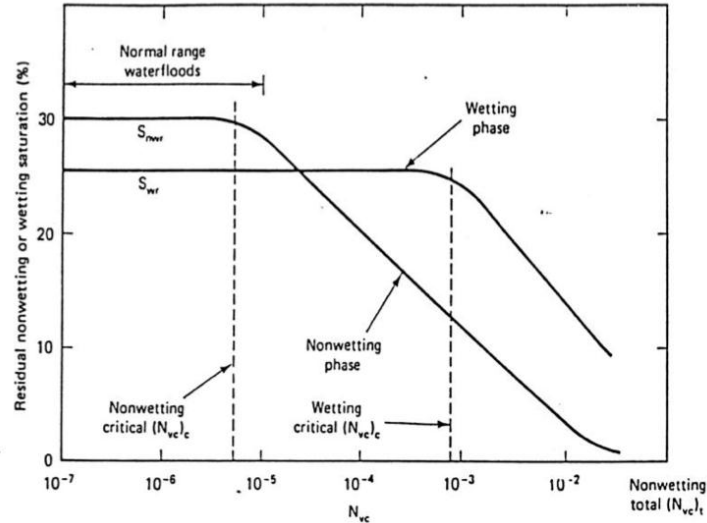
Figure 2.2 - Capillary de-saturation curve showing residual saturations (%) vs. capillary number. Non-wetting capillary numbers are normally in the range of $10^{-7} - 10^{-5}$ after conventional water flooding (Lake, 1989).

The macroscopic displacement efficiency depends highly on the relationship between viscosity and permeability. The relationship is defined by a mobility ratio M with λ_i being the mobility of the displacing fluid and λ_i the mobility of the displaced fluid (Zolotukhin and Ursin, 2000),

$$M = \frac{\lambda_i}{\lambda_j} = \frac{\dfrac{k_{ri}}{\mu_i}}{\dfrac{k_{rj}}{\mu_j}}$$

(2.3)

The factor k_r is the relative permeability, μ is the viscosity and the subscript i and j denotes displacing and displaced fluids, respectively. During multiphase flow, the mobility ratio will describe displacement stability. If the mobility ratio is low $M < 1$ a favourable relationship will exist and viscous fingering (bypassing of oil) is unlikely to occur. This will benefit the macroscopic displacement efficiency (Zolotukhin and Ursin, 2000). The total reservoir displacement efficiency is dominated by mobility ratio and capillary number (Farouq and Thomas, 1989). EOR techniques can improve oil recovery by increasing capillary number to improve microscopic sweep or provide a more favourable mobility ratio to improve macroscopic displacement.

2.1.3 Sandstone reservoirs

Sandstones are composed of sedimentary rock fragments whose grains are predominantly sand-sized varying between 1/16 and 2 mm in diameter (Bjørlykke and Jahren, 2010). They commonly consist of quartz, although sandstones often contain feldspar and numerous other mineral grains held together by silica or another type of cement. The relatively high porosity and permeability of sandstones make them good reservoir rocks for oil and gas production (Alvarado and Manrique, 2010). Highly successful North Sea fields such as Statfjord and Gullfaks are based on sandstone reservoirs of good quality, and have with improved technology increased recovery factors close to 70% (Bjørlykke and Jahren, 2010).

The most important reservoir properties are porosity and permeability, but pore geometry and wetting properties of mineral surfaces also influence petroleum production. Sandstone reservoirs show the highest potential for implementing EOR projects because most of the technologies have been tested at pilot and commercial scale in this type of rock. Figure 2.3 shows that most EOR applications have been in sandstone reservoirs (Alvarado and Manrique, 2010). The data gathered is from a collection of 1507 international EOR projects during the last decade. Thermal (steam injection) and chemical EOR methods are most frequently used in sandstone reservoirs, while gas injection is the dominating EOR method in carbonates and other rocks.
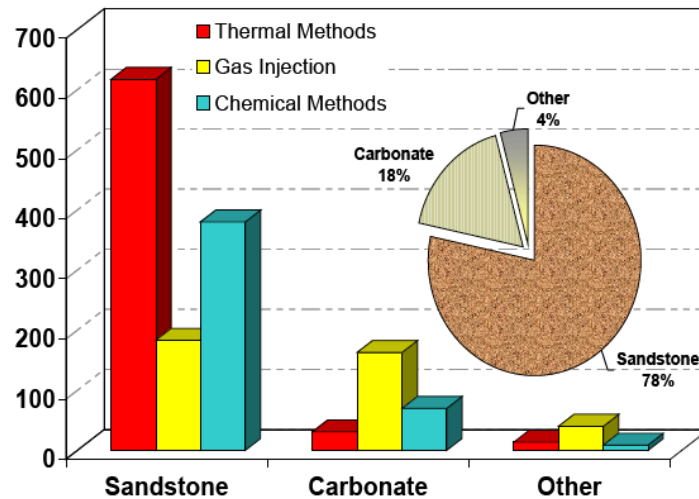
Figure 2.3 - EOR methods by rock type collected from 1507 international EOR projects (Alvarado and Manrique, 2010). The majority of EOR techniques have been applied to sandstone reservoirs, the most dominant methods being thermal and chemical injection. In carbonate and other reservoirs, gas injection is seen as the main governing technique.

2.2 Shale Reservoirs

The focus on heterogeneous carbonate and shale formations is of particular interest to nations seeing conventional reservoirs mature into their last stage of production. The current development of the abundant North American tight shale oil resources has become essential to balance their market situation and economic growth. According to Crawford and Biglarbigi (2008), oil prices are expected to remain above the threshold for economical production of shale, even though global prices continue to fluctuate in the presence of technology changes, new discoveries and OPEC strategies. Oil shale resources of commercial interest are about 2.6 trillion barrels worldwide. The US holds the largest and most concentrated deposits of nearly 2.0 trillion barrels.

Shale reservoirs are formed by compaction and consolidation of claystones and mudstones, with a diverse mineralogy from siliciclastic (sandstone) to that of carbonate (dominated by calcite and dolomite) (Zolotukhin and Ursin, 2000). Shale formations have high organic content, but are difficult to recover by conventional methods. One characteristic of shale is the extremely low permeability due to fine textured grains at sizes below 60 micrometer, and porosities less than 10 % (Kuila and Prasad, 2013).

Fluid transport is highly dependent on reservoir characteristics, and heterogeneity shows significant impact on shale recovery (Chen *et al.,* 2014). Primary production rates from shale formations are generally high, but total recovery factors are predicted to be low (Gamadi *et al.,* 2014). Unlike conventional reservoirs, water -and gasflooding do not appear to be practical or good investment due to low matrix permeability and long payback periods. However, new techniques that combine horizontal drilling with multi-stage hydraulic fracturing have made it acceptable to produce oil from tight shale formations.

2.2.1 Improved flow through hydraulic fracturing and acidizing

Contrary to conventional reservoirs, shale is usually made of thin horizons of formation beds and production by vertical well placement is minor. The introduction of horizontal drilling and well stimulation by hydraulic fracturing has made it possible to expose larger areas to the wellbore surface. Hydraulic fracturing and the injection of highly pressurized fluids form deep conductive flow paths inducing oil flow towards the wellbore. The fractures are held open by the presence of proppants (*i.e.* sand grains) counteracting the overburden pressure and rock compressibility during production.

Even with the combination of horizontal drilling and hydraulic fracturing initial production rates decline fast (Gamadi *et al.,* 2014). It is not given that hydraulic fracturing will be sufficient to keep the shale permeable in its entire production lifetime. Orangi *et al.* (2011) confirm through simulation studies that rock compaction degrades both matrix and fracture permeability. The degradation is a result of increased overburden stress during reservoir depletion. Small changes in pressure drop can change the fracture transmissibility by orders of magnitude. As cumulative production decreases, trapped saturations can be as high as 45 %.

Based on research by Morsy *et al.* (2013), combined hydraulic fracturing and acidizing was proposed to improve formation permeability. Acidizing, as stimulation technique, does not always yield essential conductivity compared to hydraulic fracturing. Morsy *et al.* suggested that by adding low concentrations of HCl to the hydraulic fluid, the dissolution of carbonate sediments (calcite and dolomite) and micro-fractures would improve reservoir permeability. Results have shown enhancement in oil recovery and also improved shale porosity by the addition of HCl.

2.2.2 Micro-scale pore size distribution

Transport mechanisms and storage capacities in shale reservoirs may be estimated based on a comprehensive understanding of reservoir pore structure. Shale is composed of complex clay microstructures aligned locally in aggregates of variable orientation (Kuila and Prasad, 2013).

A correlation between pore volume and pore diameter for shale pallets is provided in Figure 2.4, where 3 different pore structures are defined. Group A is defined as micro-pores with pore diameter of ~3 nm related to the pore space between stacks of clay elementary units. Group B are meso-pores ranging from 20 - 100 nm in pore diameter, corresponding to the pores within clay aggregates. The last group (Group C) are macro-pores in the micron size region, with diameters >1000 nm. They represent the fractures or micro-fractures between clay aggregates. As can be seen, reservoir shale is predominantly composed of group A and B elements, which are micro -and meso-pores (Kuila and Prasad, 2013)
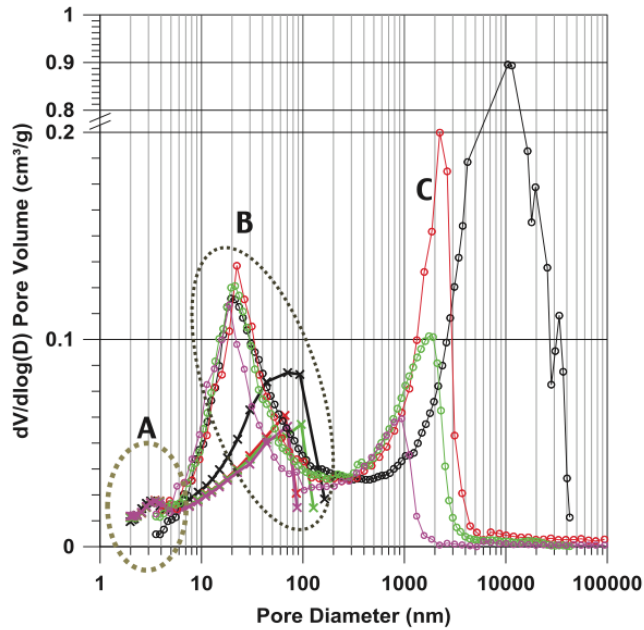
Figure 2.4 - Pore size distribution in shale pallets of Wyoming Montomorillonite (Kuila and Prasad, 2013). The peaks illustrated in the diagram identify the different distribution groups. Group A) Micro-pores with diameter of ~3 nm, Group B) Meso-pores ranging in diameter from 20 – 100 nm, and Group C) Macro-pores at diameters >1000nm.

Darcy's law or modified versions may be used if shale pores lie within the macro-range (Kuila and Prasad, 2013). However, the Darcy model cannot be directly applied if the small pores are at the micro -and meso-scale as in tight shale reservoirs. Especially at these scales, gas flow is expected to be a combination of Knudsen diffusion and/or slip-flow.

2.2.3   Fluid flow in shales

Oil production from shale formations depends on effective flow mechanisms through the porous rock. Shale reservoirs are typically characterized by gas permeabilities less than 0.1mD, and even below 0.01mD according to Bodi (2012). The typical low permeabilities in tight formations relate to matrix structure as the pore volume consists of channels ranging from micron to nanometers (Kuila and Prasad, 2013). Hence, flow in tight formations compared to conventional reservoirs can be quite different because pore sizes can be up to thousand times smaller.

Swami *et al.* (2012) stated that for a given shale pore size, actual permeability will vary with pressure. They argued that low-pressure regions in tight formations would yield larger differences in terms of actual -and Darcy permeability compared to high-pressure areas. Their assumption was confirmed by substantial calculations of actual permeability through empirical correlations provided by literature research. At approximately 5000 psi, the ratio of actual to Darcy permeability was close to 1. At lower pressures, around 200 psi, the ratio increased to in between 5-25. This low-pressure effect was also observed by Sanaei *et al.* (2014). They confirmed that actual permeability would deviate from Darcy permeability below pressures of 2000 psi (approx. 150bar).

Studies performed by Sanaei *et al.* (2014) showed that when pore sizes decrease to nanometre range the phase envelope (representing the phase conditions of a multi-component hydrocarbon mixture) shrinks and shifts to the left making fluids behave more like dry gases. In small pores, such as shale

micro -and meso-pores, flow will to a greater extent be influenced by interactions between gas molecules and pore walls. This effect is the result of free gas molecules being similar in size to flow diameter as pore size decrease, causing molecules to strike and slip against the walls. Mechanisms for transport and flow in nano-confinement will deviate from classic flow mechanics.

In conventional reservoirs fluid velocity is assumed to be zero at the pore wall and Darcy's law will be applicable for determining flow capacity. However, in micro -and meso-pores, non-Darcy flow occurs as the mean free path (the average distance a gas molecule travels before colliding with another) is decreased causing an increase in effective gas permeability (Sanaei *et al.,* 2014). The effect is especially evident in small pores at low pressures as observed by Swami *et al.* (2012) and Sanaei *et al.* (2014).

Knudsen number

To correct for effects of non-Darcy flow during permeability measurements in tight shale, the Knudsen number K_n can be used to quantify the effects of increased gas slippage against the pore walls. The Knudsen number is used to classify flow into different regimes based on increasing Knudsen numbers (Swami et al., 2012). The numbers describes the deviation from Darcy flow into transition flow where free molecular diffusion becomes apparent. Figure 2.5 shows the flow regimes defined in terms of Knudsen number.

The Knudsen number defines four flow systems. Flow in conventional resources generally occur within the viscous -or slip flow regime, where Darcy's law for laminar flow or modifications of Darcy's law (correcting for non-Darcy behaviour) is valid. Flow in shale reservoirs usually occurs within the slip -or transition flow regime (Swami *et al.* 2012).
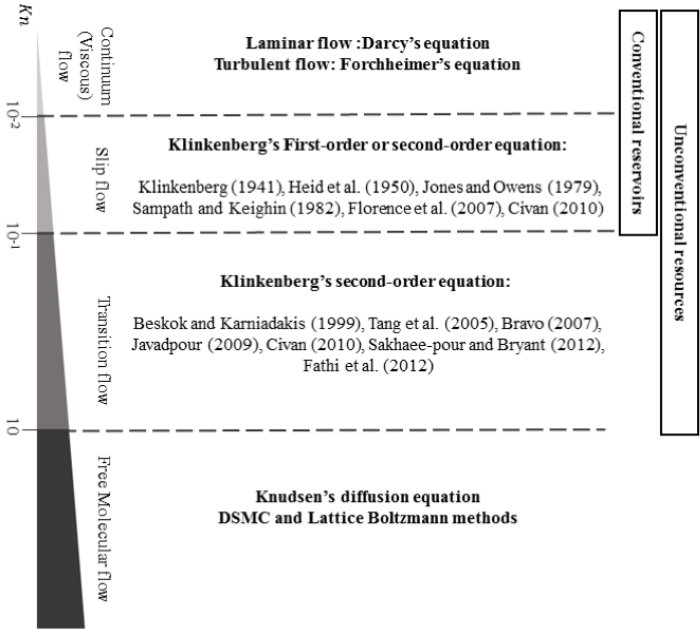
Figure 2.5 - Knudsen flow regimes. 1) Viscous flow for K_n ≤0,001 where mean flow path is negligible and intermolecular forces dominate, 2) Slip flow for 0.001< K_n <0.1 where mean flow path become significant and viscous flow theory need be modified, 3) Transition flow for 0.1< K_n <10 where slip or transition flow becomes dominant for most shale reservoirs, and 4) Knudsen's (free molecular) flow for K_n ≥ 10 defined by Knudsen's diffusion equation (Sanaei et al., 2014).

Gas permeability in tight shale

Darcy's law is only to some degree applicable for gas flow through low permeable shale. The law is valid for a 100 % saturated medium with horizontal laminar (viscous) flow of an incompressible fluid. In Darcy flow it is assumed that fluid behaves non-chemically with its surrounding rock surface, and that flow is stationary. The absolute permeability k can then be calculated by the Darcy equation,

$$q = \frac{Ak}{\mu} \frac{\Delta p}{L}$$

(2.4)

Where q is the applied injection rate [m^3/s], μ is the average viscosity [$Pa \cdot s$], L is the length of the media [m], Δp is the differential pressure across the core [Pa], A is the area of the cross section [m^2] and k is the absolute permeability in [m^2] with a factor of $0.987 \cdot 10^{-12} m^2 = 1D$ when converting to Darcy units (Zolotukhin and Ursin, 2000).
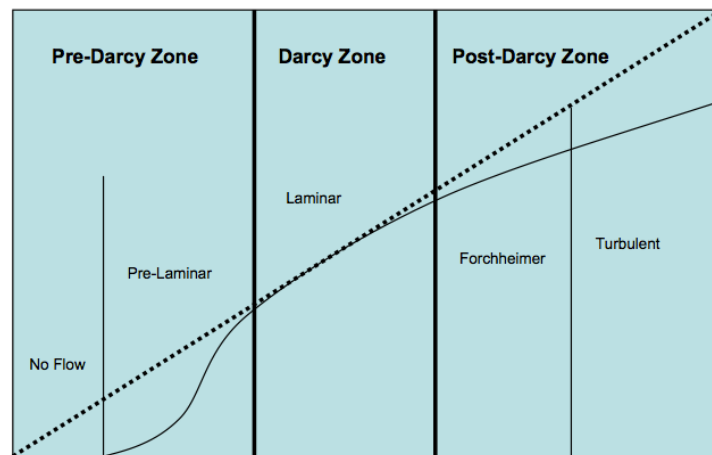
Figure 2.6 - The different flow regimes by Darcy's law (Basak, 1977). The "Darcy Zone" represents the viscous dominated laminar zone where the pressure gradient is linear to flow velocity. In the Post-Darcy zone velocity increases and flow is dominated by inertia effects (Forchheimer) prior to unsteady laminar and turbulent flow.

Darcy's empirical law represents a simple linear relationship between flow rate and pressure drop as shown in Figure 2.6 (Zeng and Griegg, 2006). It does not take into account the effect of inertia or acceleration forces at high flow rates, as viscous resistance is believed to be the dominating force (Huang and Ayoub, 2008). Further, gas permeability deviates from Darcy conditions as gas rate increases beyond the Darcy Zone, and corrections for additional pressure drops have to be made (Zolotukhin and Ursin, 2000).

The Darcy regime reaches its limit when flow velocity becomes so large that effect of inertia and/or turbulence becomes relevant (Huang and Ayoub, 2008). Inertia occurs gradually with increasing rates by acceleration and deceleration of gas travelling through the tortuous paths of the porous media. By inertia, gas will enter into the Forchheimer region Figure 2.6. Darcy's law will still be valid, but a term needs to be added to account for the increase in pressure drop (Zeng and Griegg, 2006). Beyond this region, turbulence will dominate and bring flow out of the viscous and into the slip flow regime, as illustrated in Figure 2.5, where Darcy's law will not be valid without considering a Klinkenberg correlation (Sanaei *et al.,* 2014).

The slip flow regime is based on Klinkenberg's discovery of gas slippage along pore walls (Sanaei *et al.,* 2014). Klinkenberg corrects for the overestimated permeability by defining a mean pressure correlating gas permeability to absolute fluid permeability. In laboratory practice, the Klinkenberg effect is assumed effective at gas pressures below 10 bars (Zolotukhin and Ursin, 2000).

If gas permeability is restricted to the laminar flow regime, and pressure drop remains proportional to flow rate within an experimental error, the pressure drop can be taken to be the average pressure drop (Ahmed, 2006). Gas permeability k_g can then be calculated using Darcy's law for compressible fluids,

$$Q_g = \frac{k_g A (p_1^2 - p_2^2)}{2\mu_g L p_b}$$

(2.5)

Where Q_g is the gas flow rate [*ml/s*], μ_g is the average gas viscosity [*cP*], L is the length of the media [*m*], p_1 is the inlet (upstream) pressure [*Pa*], p_2 is the outlet (downstream) pressure [*Pa*], A is the area of the cross section [*m²*], p_b is the base (atmospheric) pressure [*Pa*], and k_g is the gas permeability in [*m²*].

When conducting miscible CO_2 injection one objective is to estimate the flow capacity, permeability, for the shale samples provided. When estimating CO_2 gas permeability, potential effects of inertia or slip-flow have to be accounted for as liquid and supercritical CO_2 are highly compressible through the micro -and macro pores of the shale network. The modified versions of the Darcy's law have to be considered. The assumptions made when accounting for non-Darcy flow are presented in section 9.1.1.

2.3   Enhanced Oil Recovery

During field-scale production, different measures are taken for improved oil recovery (IOR). The term IOR is defined as economic initiatives that intend to increase oil recovery and/or accelerate reserves (Skarestad and Skauge, 2012). IOR measures are related to drilling and completion, reservoir management, production processes, and the implementation of EOR techniques. When applying EOR, materials not originally present in the reservoir are injected to increase the amount of recoverable reserves.

The impact of IOR measures is illustrated in Figure 2.7. Accelerating reserves by action 1 (*i.e*. re-perforating wells *etc.*) yield a higher net present value (NPV) and expected ultimate recovery (EUR) at the economic cut-off rate Q_e, but cumulative recovery remains unchanged N_{pi}. By implementing EOR techniques by action 2, NPV will decrease, but recoverable reserves will increase providing a higher EUR at Q_e and higher maximum cumulative recovery $N_{p,max}$.
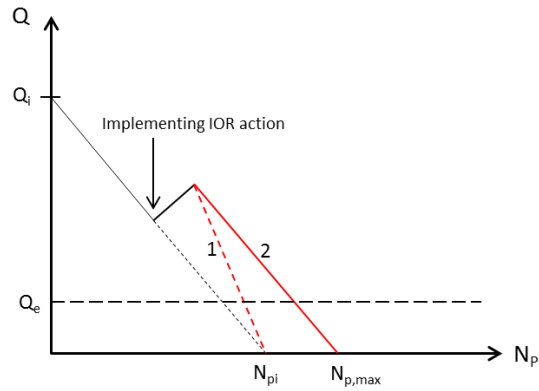
Figure 2.7 - Impact of IOR measures. Action 1) Accelerating reserves by production enhancement, Action 2) Increasing amounts of recoverable resources by EOR methods. Modified from Skarestad and Skauge (2012).

EOR is classified into four categories 1) miscible flooding, 2) chemical flooding, 3) thermal flooding and 4) microbial flooding (Terry, 2001). The purpose of EOR is to reduce the residual oil saturation after primary and/or secondary recovery. It seeks to improve the macroscopic displacement by reducing the mobility ratio between injected and in-place fluids, and/or to eliminate or reduce the capillary forces to increase microscopic sweep. EOR is frequently referred to as a tertiary recovery method in extent of the secondary methods such as water -or gas flooding. However, depending on reservoir conditions, EOR is often used as a supplement to the secondary methods (*e.g.* in shale reservoirs).

3   Low Salinity Waterflooding

Enhanced oil recovery by low salinity waterflooding (LSW) was initially reported by Tang and Morrow (1997), and further studies on LSW has since been carried forward by research and industry scale projects, such as the LoSal ® EOR program created by BP (Lager *et al.* 2008). Where conventional water flooding uses formation brine or seawater to maintain reservoir pressure, LSW will in addition, improve microscopic sweep by the injection of diluted water concentrations.

Wettability alteration during LSW is generally detected through indirect changes in relative permeability or capillary pressure curves (Morrow and Buckley, 2011). Some of the more accepted hypotheses based on crude-oil/brine/rock (COBR) interactions are multi-component ion exchange (MIE), electrical double layer expansion or the possibility of fines migration (Tang and Morrow 1999; Lager *et al.* 2006; Ligthelm *et al.* 2009).

A general assumption is that LSW alters reservoir wettability towards a more favourable condition for oil recovery. By reducing the salt content in the injected water, wettability shifts towards a more water-wet state improving microscopic displacement, fluid flow and reducing the residual oil saturation. It has been suggested that more than one mechanism may be present as the low salinity effect (LSE) occurs under a variety of circumstances (Tang and Morrow 1999). However, a consistent theory has so far not been established to explain the underlying mechanisms.

3.1   Low Salinity Effect in Sandstones

Chemical and physical properties vary between rock types (e.g. sandstones and carbonates), and the related effect of LSW has not yet been fully determined. The majority of experiments conducted are based on core flooding of sandstone, similar to the work by Tang and Morrow (1997). They worked under the assumption that high salinity brine and injected low salinity water could influence wettability at reservoir temperature. The wettability modification implied that adsorbed crude oil components at the rock surface were partially reversed due to the decrease in salinity, hence shifting surface preference towards water-wet conditions. Results confirmed that wettability alterations improved oil recovery.

In the field, successful low salinity injections have been observed consistent with laboratory results. In 2004, a log-injection-log trial was performed through a single well in a sandstone reservoir showing significant increase in oil production due to low salinity injection (Webb *et al.*, 2004). By mobilization of residual oil in the near wellbore region, a 25 - 50 % increase in oil recovery was detected. Ligthelm *et al*. (2009) also reported a Middle Eastern sandstone reservoir with 4-5 % increase in oil recovery by LSW.

LSW has been evaluated at the Snorre field for increased oil production on the North Continental Shelf (NCS) (Skrettingland *et al.,* 2010). However, screening tests from core flooding, and a single well field pilot, indicated low to marginal effects on oil recovery by low salinity injection in a third and unconventional stage of production. LSW is at present a potential EOR technique to be tested in full-scale reservoir performance on the NCS.

Mechanisms influencing the performance of LSW such as fines migration, multi-component ion exchange, electrical double layer expansion, and salt-inn effects will be briefly reviewed below.

3.1.1 Fines migration

Tang and Morrow (1999) identified the following necessary conditions for the low salinity effect (LSE) to be present 1) adsorption of crude oil for mixed-wet conditions, 2) availability of significant fines -and clay fractions, and 3) the presence of connate brine. It was assumed that crude oil containing heavy polar compounds would adhere to the rock surface uncovered by connate brine creating mix-wet conditions. When introducing a change in brine to the system, movable fines and clays adsorbed with mixed-wet particles would relocate at the oil-water interface resulting in increased water-wet conditions.

A decrease in permeability and increase in pressure drop also indicated that released particles could increase microscopic sweep by blocking pore throats and diverting flow into un-swept areas (Tang and Morrow 1999). However, Lager *et al.* (2006) questioned the link between particle release and flow diversion. They argued that even though numerous observations were in agreement, experiments performed by BP observed additional oil recovery without permeability reduction and particle migration.

3.1.2 Multi-component ion exchange

One of the more accepted hypotheses was provided by Lager *et al.* (2006) based on the concept of multi-component ion exchange (MIE). They postulated that Ca^{2+} and Mg^{2+}- cationic exchange between the mineral surface and injected low salinity water was responsible for the increase in recovery. Multivalent cations in connate brine adhere to a negatively charged clay surface and bonds to polar components in the oil phase forming organo-metallic complexes. In addition, organic polar components may displace cations and adsorb directly onto the mineral surface increasing the oil-wetness of the rock. During low salinity injection, MIE occurs where un-complex inorganic cations replace organic polar compounds and organo-metallic complexes at the clay surface. As a consequence, the system shifts towards increased water-wet conditions.

The MIE theory explains many of the results obtained in literature based on the importance of connate brine containing divalent cations, and mineral rocks holding certain cationic exchange capacities (Boussour *et al.,* 2009). The theory of MIE confirms Tang and Morrow's (1999) conclusion that refined oil yields no effect to low salinity injection, because no polar compounds are present to interact with the clay minerals (Lager *et al.,* 2006). It also confirms why LSW gave no results on the acidized and fired core experiments performed by Tang and Morrow (1999). Lager *et al.* (2006) concluded that the removal and stabilization of fines by acidizing and firing reduced sensitivity to low salinity injection by destructing the cation exchange capacity at the water-clay interface.

3.1.3 Electrical double layer expansion

Ligthelm *et al.* (2009) confirmed the theory proposed by Lager *et al.* (2006) that the presence of multivalent cations in connate brine increase surface oil-wetness, and that LSW with a high cationic content was partially responsible for the subsequent wettability alteration. However, they reasoned that the major contribution towards increased water-wetness was the result of reduction in ionic brine strength. Low brine potential yields an expansion of the electrical diffuse double layers surrounding clay and oil particles resulting in electrostatic repulsion. Once these repulsive forces

exceed the binding forces through the multivalent cation bridges, the oil particles will be desorbed from the clay surface altering the wetting state.

3.1.4 Salt-in-effect and pH elevation

Alternative theories postulated to LSW are the "salt-in-effect" proposed by RezaeiDoust *et al.* (2009) and the effect of localized pH elevation by Austad *et al.* (2010). The proposition by RezaeiDoust *et al.* (2009) is based on increased solubility of organic materials due to the presence of two-valent ions within the low salinity phase. Because of increased solubility, some organic material may desorb from the clay and improve water wetness. Austad *et al.* (2010) defines LSE as a consequence of cation desorption at the clay surface that induces a local pH increase when the cation is substituted with a H^+ molecule from the injected low salinity water. A normalized acid-base reaction occurs between H^+ and OH^- molecules increasing water wetness.

3.2 Low Salinity Effect in Carbonates

Carbonate reservoirs make up to 50% of the world proven hydrocarbon reserves However, due to the fairly heterogeneous nature in terms of porosity and permeability, recovery factors are observed to be less than 30% OOIP and the IOR potential from carbonates is therefore high. Carbonate reservoirs have a high organic content, but recoveries remain low due to a low matrix permeability generally ranging between 1-10 mD and extensive fracture systems (Høgnesen *et al.*, 2005). The high permeable fractures in carbonates carry the majority of flow, and the absence of viscous forces across the matrix are negative for production (Fernø, 2012). Hence, in carbonates, capillary imbibition remains the main recovery mechanism compared to viscous displacement.

Most carbonate reservoirs are preferentially oil-wet, and the wettability preference reflects the imbibition potential of the reservoir (Høgnesen *et al.*, 2005; Fernø, 2012). Because of the negative capillary pressure in carbonates, the water imbibition associated with conventional waterflooding will not spontaneously displace oil from matrix (Høgnesen *et al.*, 2005). The injection of low saline water in carbonates will hence experience reduced spontaneous imbibition since reservoirs are basically oil-wet.

However, research has revealed increased oil recovery from certain carbonates exposed to LSW. The effect was investigated by Romanuka *et al.* (2012) through spontaneous imbibition experiments on oil-bearing outcrop chalk, reservoir limestone and dolomite, resulting in increased recovery from several of them. It is generally accepted that the increased recovery by LSW in carbonates is due to wettability modifications of the mixed-oil wet surface. However, due to the fractured nature of carbonates, it may be questioned to what degree low saline water is able to imbibe into the oil-wet matrix inducing wettability alterations. Sandengen and Arntzen (2013) proposed osmotic diffusion to be a driving force in overcoming the negative capillary pressures of oil-wet rock, causing counter-current flow during spontaneous imbibitions experiments. Hence, small-scale diffusion processes driven by osmotic pressure gradients can be the mechanism for EOR in carbonates as well as sandstones.

3.3 Visualization of Low Salinity Effect

A majority of experimental work on LSW is based on core scale experiments and study of wettability changes through relative permeability curves and spontaneous imbibition tests. However, present new developments in micromodel visualization may be used to detect possible fluid-fluid interactions during low salinity waterflooding directly at the pore level. Parameters for maximum oil recovery may be investigated, and theories for predicting the performance of LSW can be developed and further quantified by core flood experiments.

Visualization studies on low salinity injection through micromodel experiments were reported by Emadi and Sohrabi (2013). During their studies, a mixed-wet micromodel saturated with high salinity brine and crude oil was utilized. When low salinity water came in contact with crude oil, water micro-dispersions formed at the oil-water interface and within the oil bulk phase. A hypothesis was developed, explaining the formation and coalescence of micro-dispersions based on the dual nature of crude oil surface-active molecules. These surface-active compounds, called monomers, consists of two functional groups, one hydrophilic (water-soluble) and one hydrophobic (oil-soluble), and work as natural surfactants (Zoloutkhin and Ursin, 2000). When crude oil is brought in contact with an aqueous phase these natural surfactants accumulate on the water/oil interface. If accumulation is increased above a critical concentration, an ordered aggregation of surfactant molecules (micelles) will form in either the aqueous phase or oil phase depending on salinity content (Zolotukhin and Ursin, 2000).

Emadi and Sohrabi (2013) explained that when the ionic strength of the injected water was lowered, the monomers would migrate from the oil-water interface of the low saline water into the oil phase. The monomers in the oil would further create reverse micelles around water cores found within the bulk, defined as water micro-dispersions. The concept of connate water swelling occurs as the water micro-dispersions flow through the oil phase and mix with the connate water, causing the brine phase to expand. If high salinity water is introduced back into the system, the water micro dispersions become unstable and collapse, leaving behind droplets of water in the oil phase.

Two mechanisms were credited the increase in oil recovery, 1) wettability alteration towards water-wet conditions, and 2) connate water swelling. However, Emadi and Sohrabi (2013) did not attempt to explain what mechanisms could be active in the transport of water micro-dispersions through the oil phase. With reference to the findings of Sandengen and Arntzen (2013), it could be argued that the crude oil acts as a semi-permeable membrane transporting water micro-dispersions in the presence of an apparent salinity gradient. If the salinity gradient is sufficient, an osmotic diffusion process could be considered as a contributing effect to low salinity waterflooding and oil mobilization. This effect will be discussed below, emphasizing on mobilization of residual oil by osmotic diffusion.

3.4 Osmosis during Low Salinity Waterflooding

In an oil/water/rock system containing high salinity connate brine, the injection of low salinity water results in a salinity gradient between the two aqueous phases. Due to this salinity gradient, an osmotic pressure will be present to induce molecular diffusion between the two phases. Molecular diffusion by osmosis occurs in systems where a semi-permeable membrane separates phases of different concentration, passing only pure solvents (*e.g.* water) and no solutes (*e.g.* salt) (Chang, 2008). Hence, the osmotic pressure gradient causes water molecules to move from areas of low salt concentration (with a surplus of water molecules), to areas of high salt concentration. The osmotic process is illustrated in Figure 3.1. Water transport through the membrane will stop up when salt concentration is the same on both sides.
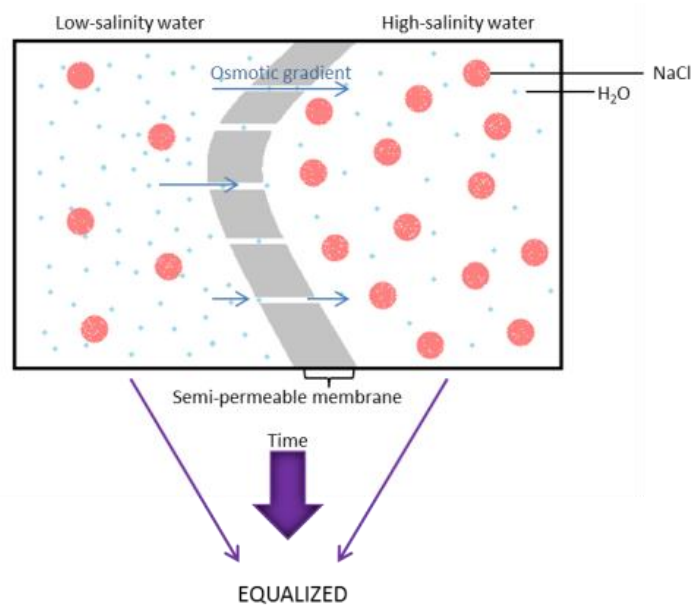
Figure 3.1 - Osmotic diffusion through a semi-permeable membrane. Water molecules from a low salinity concentration diffuse through the semi-permeable membrane into the high salinity phase. The semi-permeable membrane acts like a fine filter passing only the pure solvent (water), but is impermeable to the solute (NaCl). Osmotic diffusion ceases as the concentration difference is equalized.

In a given oil/water/rock system, it is plausible that osmotic diffusion will occur with the intermediate oil layer acting as semi-permeable membrane transporting water molecules from the low-salinity to the high-salinity side. As a result, the inaccessible connate brine will expand and displace the oil layer towards the low salinity phase for enhanced oil recovery.

The degree of osmotic diffusion is determined by the amount of water flux through the semi-permeable membrane. The water flux can be calculated using Fick's law given as,

$$J_A = -D_{AB}\left(\frac{\partial C_A}{\partial x}\right)$$

(3.1)

Where J_A is the flux of low salinity water A [mol/sm^2], ($\partial C_A/\partial x$) is the concentration gradient between the aqueous phases across the diffusion distance [mol/m], and D_{AB} is the diffusion constant of low salinity phase A to high salinity phase B [m/s] (Berg, 2010).

The concentration gradient depends on the relative difference in salt concentration between the two water phases. Water flux through the membrane will generally start to cease as the concentration gradient is reduced by dilution of high salinity water. Fick's law also state that the amount of water flux is proportional to the diffusion constant D_{AB}. This diffusion constant is temperature dependent, meaning diffusion will increase with increasing temperature. When the diffusion coefficient is evaluated the Stokes-Einstein equation is used. From this equation the following relationship between the diffusion constant, temperature and viscosity is,

$$D_{AB} \propto \frac{T}{\mu} \qquad\qquad (3.2)$$

Where T is the absolute temperature and μ is the dynamic viscosity of the fluid. The diffusion constant can be measured through various oil compositions. Lower number alkenes tend to have a higher diffusion constant, while higher viscosity yields a lower diffusion constant.

Experiments conducted by Ellila (2012) showed that the water flux through the oil phase would improve with an increase in osmotic gradient. In terms of chemical thermodynamics, the diffusion process through the oil membrane is a result of the difference in chemical potential between the two aqueous phases. The chemical potential is an inverse function of concentration. Hence, for low salinity water the chemical potential will be high, while for high salinity brine the chemical potential will be low. Equilibrium is established when the difference in chemical potential is reduced to zero. In a porous medium this equals the point where the high-saline brine is 100% diluted by the low-salinity water.

3.4.1 Osmotic diffusion in fractured shale formations

The effect of osmotic pressure, caused by salinity contrasts, has also been used to enhance oil production from unconventional oil-wet shale (Fakoharoenphol *et al.,* 2014). The majority of shale formations have a diverse mineralogy similar to that of carbonates, and generally high amounts of clay sediments. Due to the wide pore-size distribution, as defined by Kuila and Prasad (2013), it is believed that these clay sediments have the potential of acting as semi-permeable membranes, passing and restricting certain solute particles. The semi-permeable membrane property of clays can be explained by the electrical double layer expansion theorem of Ligthelm *et al.* (2009). During hydraulic fracturing, the injection of low salinity water at high pressures will create a salinity gradient to the initial high salinity brine. When low salinity water contacts clays, the electrical double layer between sheets will expand, forming a neutral zone passing only neutrally charged water molecules to the centre of the porous structure.

It was proposed by Fakoharenphol *et al.* (2014) that shale swelling during drilling should be attributed to osmotic pressure. Hence, a theory was presented on osmotic induced flow in shale as illustrated in Figure 3.2. Initially, oil saturates the larger part of the nano-pores and the high salinity water is bound to clay laminations. During LSW, the injected low saline water contacts the clay sediments and the non-polar water molecules flow through the neutral zones in presence of an osmotic gradient. The increased water saturation within the clay structure causes the clay to swell, and the pressure within the nano-pore increases until oil is relocated through larger meso-pores.
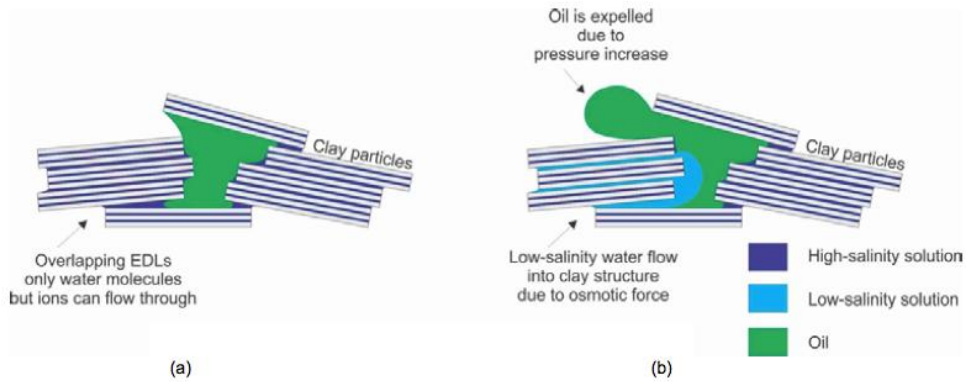
Figure 3.2 - Osmotic induced flow in shale (Fakoharenpol et al., 2014). A) Oil occupies most of the pore space while formation water is bond to clay laminations. B) Low salinity water contacts the clays, and water molecules enter the nano-pores due to the osmotic pressure gradient. Clay swells and the built up pressure expels oil through larger pores.

In addition, as shale formations are mainly oil-wet, multivalent bridging of oil molecules to the negatively charged clay surface adsorb based on the MIE theory by Lager *et al.* (2006). Water-wetness and the relative permeability to oil increase mobilizing irreducible oil saturation. Fakoharenphol *et al.* (2014) illustrated the effect of osmotic pressure by performing spontaneous imbibitions experiments on oil-wet shale samples. Results showed significant improvement on oil displacement when submerged in low salinity water.

4 Miscible CO$_2$ Injection

Carbon dioxide (CO$_2$) has been used for EOR since 1972, when the first miscible CO$_2$ flood was performed at the SACROC Unit in Texas, United States (Lambert *et al.* 1996). It was expected that miscible CO$_2$ injection would yield additional recoveries of 8 – 16 % of OOIP after waterflooding from the given unit. In 2012, SACROC still produced nearly one million barrels a year, 40 years after EOR was initialized (Meltzer, 2012). The same year, estimates showed that miscible CO$_2$ injection had reached 5 % of the United States total crude oil production (Enick and Olsen, 2012).

CO$_2$ is one of the most abundant gases in the atmosphere. The burning of fossil fuels (*i.e.* oil, gas, coal etc.) releases high amounts of CO$_2$ into the air, and is a source for carbon-based emissions. CO$_2$ is a factor in global warming and in order to reduce the amount of CO$_2$ released to the atmosphere by fossil fuels, a worldwide carbon capture and storage (CCS) program has been initiated, urging the petroleum industry to invent more effective ways to integrate the produced CO$_2$ in EOR, and/or store amounts of injected CO$_2$ in underground reservoirs (Iglauer, 2011).

The Norwegian petroleum industry has gained significant experience with CO$_2$ storage on the North Continental Shelf (NCS). Since 1996, CO$_2$ from the Sleipner Vest field has been recycled into the Utsira formation for storage (NPD, 2014). The availability for gas storage on the NCS is large, but the lack of CO$_2$ has halted further project development. CO$_2$ for EOR remains primarily an active technique in the US, where 74.4 % of CO$_2$ for EOR is available through natural gas reserves (Enick *et. al.,* 2012).

4.1 CO$_2$ Injection in Shales

It has been postulated that osmosis during LSW can act as contributing mechanism in EOR from shale formations (Fakoharenphol *et al.* 2014). However, LSW will not be a practical investment in tight-shale formations because of its low injectivity potential. Even in combination with hydraulic fracturing, LSW would require a long payback period if osmotic diffusion and LSE was the only contributing mechanisms. The effect of osmotic diffusion by LSW is still being researched, hence other methods need be considered for EOR from shale oil reservoirs as a supplement to secondary water -or gas injection.

Ongoing research at the Dept. of Physics and Technology (UoB) focus mainly on CO$_2$ gas for EOR and carbon storage during production. A wide range of research activities has previously been investigated, such as CO$_2$ foam for mobility control and integrated EOR (IEOR) (Haugen *et. al.,* 2014) and visualization of CO$_2$ diffusion in fractured chalk (Eide *et al.* 2013). A favorable characteristic of CO$_2$ compared to other gases is miscibility with resident oil at reservoir conditions.

The majority of performance -and evaluation studies on miscible CO$_2$ injection for shale oil recovery are provided by numerical reservoir simulations. Simulation studies conducted on miscible CO$_2$ flooding include both continuous and cyclic injection schemes, and field scale tests (Vega *et. al.,* 2010; Dong and Hoffman, 2013; Chen *et. al.,* 2014). Some core-scale laboratory studies on miscible CO$_2$ injection in unconventional shale exist focusing on improved oil recovery (Kovscek *et al.* 2008; Gamadi *et al.* 2014).

4.1.1 Continuous CO_2 injection

Kovscek *et al.* (2008), performed core-scale CO_2 injection into siliceous shale for the purpose of improving oil recovery. The experiment was conducted at near miscible conditions, and resulted in a 10% increase of OOIP by continuous CO_2 injection (after initial counter-current production in a closed downstream system). In 2010, an extension to the study by numerical simulation was conducted by Vega *et al.* (2010).They simulated miscible CO_2 injection into low permeable shale with the same characteristics as Kovscek *et al.* (2008) (permeability of 1.3mD, and porosity of 34%). By using the same production scheme, results yielded an additional recovery of 39 %OOIP by continuous CO_2 injection. The total recovery estimate was 93%.

4.1.2 Cyclic CO_2 injection

Chen *et al.* (2014) simulated the potential of cyclic CO_2 injection as a potential secondary recovery method for reservoir shale oil. In cyclic injection, CO_2 is exposed to the formation for a certain soaking period and recovered due to the pressure build-up caused by oil swelling. Findings showed that recovery rates from the initial CO_2 cycle peaked at values above that of primary production. However, during progressive cycles, the rates declined because the production periods could not compensate for the recovery loss during injection -and soaking.

The importance of shut-in period on cyclic CO_2 injection was further investigated by Gamadi *et al*. (2014), in addition to enhanced oil recovery. Experiments were performed on core samples in laboratory and it was discovered that re-pressurization was an important factor for ultimate production. A higher number of cycles and shorter shut-in periods lead to better recovery. In terms of oil production, their work provided an additional recovery of 10-29% and 33-85%OOIP for different shale types under various operating conditions.

Based on the encouraging results from both simulations and experimental studies, miscible CO_2 injection is shown to be a suitable EOR method for shale oil reservoirs. Implementing miscible CO_2 during the cyclic injections gave positive recovery results, even if no conclusions were drawn to its contributing mechanisms (Gamadi *et al.*, 2014). The simulation results of Vega *et al.* (2010) indicated the potential of achieving almost 100% oil recovery from siliceous shale by miscible CO_2 injection. However, further work needs to be performed on laboratory core-scale to fully explore the potential of CO_2 injection in shale formations.

Miscible CO_2 may increase flow through the shale structure due to the higher mobility of oil when mixed with CO_2. This thesis investigates the possible effect of miscible CO_2 injection in tight (< 1mD) low porosity reservoir shale. The objective is to quantify the residual oil production (%OOIP) by continuous CO_2 injection, and determine the effect of displacement, miscibility and flow capacity.

4.2   Mechanisms during CO_2 Injection

In miscible CO_2 injection, pure CO_2 constitutes over 95% of the overall injected composition (Meltzer, 2012). The gas has shown itself to be a very effective solvent, providing better sweep efficiency than other lean gases (i.e. CH_4 or N_2) (Zolotukhin and Ursin, 2000). Since CO_2 is highly mobile, it is often integrated with other EOR techniques such as water-alternating gas (WAG), or CO_2 foam (CO_2 + surfactant) for mobility control and improved displacement efficiency.

CO_2 is known to be highly soluble with oil causing it to swell and the resulting miscibility reduces viscosity and increases oil mobility Figure 4.1. The gas is to a lesser extent soluble in water, but CO_2 will increase water-viscosity towards a favourable macroscopic displacement with time (Latil, 1980). In addition, CO_2 gas has the capability of extracting heavier components of C_5-C_{30} from crude oil compositions, where lean gases only extract intermediates of C_2-C_6 (Skarestad and Skauge, 2012). During tertiary recovery, the implementation of miscible CO_2 will decrease the interfacial tension between water and residual oil, improving the microscopic sweep efficiency.
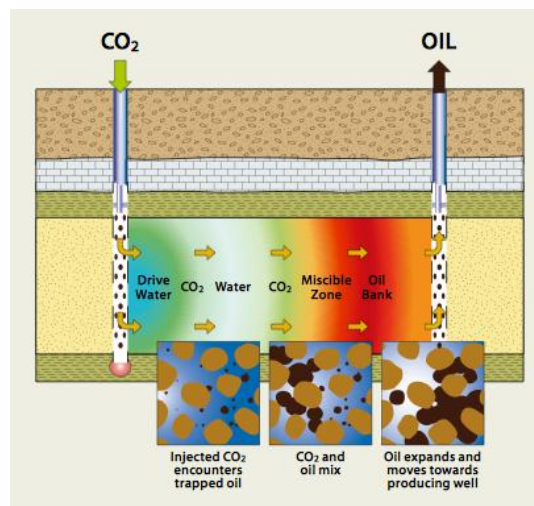
Figure 4.1 - CO_2 WAG process (NPD, 2014). 1) The injected CO_2 comes in contact with residual oil, 2) The CO_2 mixes with the oil phase due to its high solubility, 3) The oil phase swells and mobility increases. Drive water provides additional displacement of oil towards the production well.

4.2.1   Physical properties of CO_2
The physical properties of CO_2 change with temperature and pressure. At standard conditions (25 °C, 0.987 bar) CO_2 is in gas phase, but transits into liquid or supercritical state as temperatures and/or pressures are increased. Figure 4.2 shows a typical phase diagram for CO_2. During a miscible injection CO_2 is either liquid or supercritical depending on reservoir conditions. At temperatures and pressures above the triple point (where the three phases coexist), CO_2 will be in its liquid phase. At the critical point, CO_2 will be in supercritical state behaving both as gas and liquid with no phase boundary. According to NIST (2011), CO_2 reaches supercritical state at a temperature of 30.98 °C and a pressure 73.8 bar.
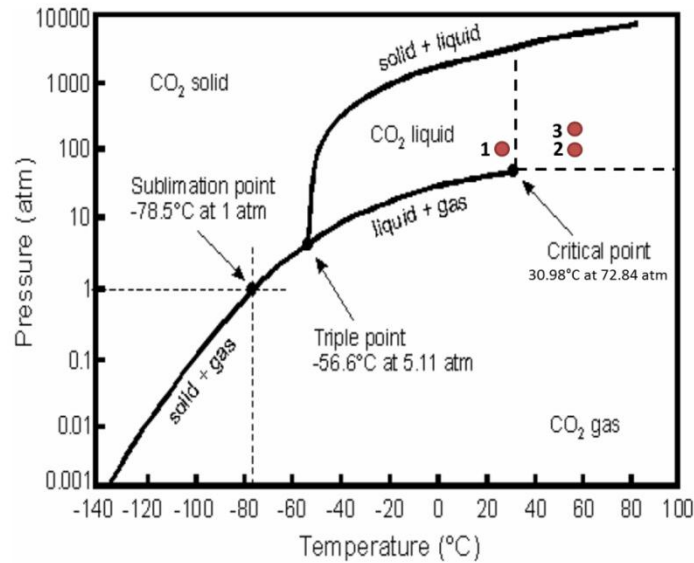
Figure 4.2 - Phase diagram for CO₂. The red dots represent the experimental conditions under which CO₂ was used in this thesis. Experiments were performed at 1) 100 bar and 25 °C liquid state, 2) 100 bar and 60 °C supercritical state, and 3) 160 bar and 60 °C supercritical state (1bar = 0.987 atm). Modified from Picha (2007).

Both density and viscosity are pressure dependent variables. As illustrated in Figure 4.3, both viscosity and density of CO₂ increase with increasing pressure under isothermal conditions. At low temperatures (*i.e.* 20 °C), the phase transition from vapour to liquid is a direct shift where viscosity and density increase instantly. The instant increase occurs because the system is below the critical temperature (30.98 °C) when CO₂ changes from gas to liquid. At higher temperatures (*i.e.* 60 °C), the phase transition from gas to supercritical occurs gradually with increasing pressure. This gradual change from one state to another is due to the similar properties of liquid and supercritical CO₂. In miscible recovery, the higher CO₂ density and viscosity compared to other gases is favourable. High density provides less gravity segregation, and higher viscosity provides a positive mobility ratio.

Figure 4.3 - Viscosity and density of CO₂ at isothermal conditions (Brattekås, 2014). Graphs show viscosity of CO₂ vs. pressure (left), and density of CO₂ vs. pressure (right). The black dashed curves represent the critical temperature 30.98 °C where CO₂ shifts into supercritical state.

30

4.2.2 Miscibility of CO_2

At given conditions, CO_2 acts like an effective solvent that extracts light and intermediate hydrocarbons from the reservoir oil (Skarestad an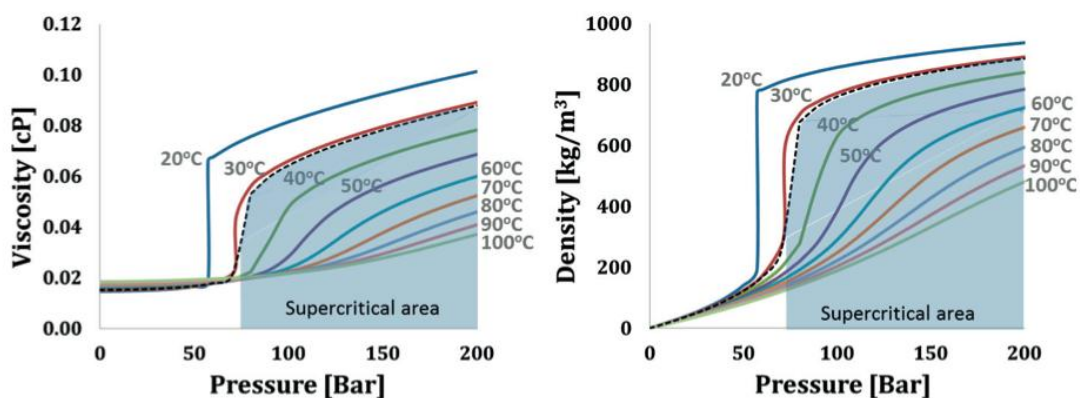d Skauge, 2012). The resulting miscibility may be partial or complete depending on fluid properties, temperature and pressure. Miscible CO_2 floods are either first-contact, or multiple-contact miscible (Terry, 2001). At first-contact miscibility, CO_2 is directly dissolved into the oil phase. By multiple-contact miscibility, intermediate oil components mix gradually with the CO_2 across a transition zone. The back of the transition zone is completely miscible with injected CO_2, while the front is miscible with the reservoir oil.

Compared to other gases, CO_2 has the advantage of low minimum miscibility pressure (MMP), the minimum pressure required to develop a miscible displacement (Skarestad and Skauge, 2012). By slim-tube experiments, MMP can be determined by constructing an MMP-curve Figure 4.4 (Yellig and Metcalfe, 1980). The curve plots recovery factors for a given pore volume CO_2 injected at various pressures. The pressure at which the curve levels off determines the MMP. Above this point, further increase in pressure will not enhance oil recovery as miscibility is obtained.
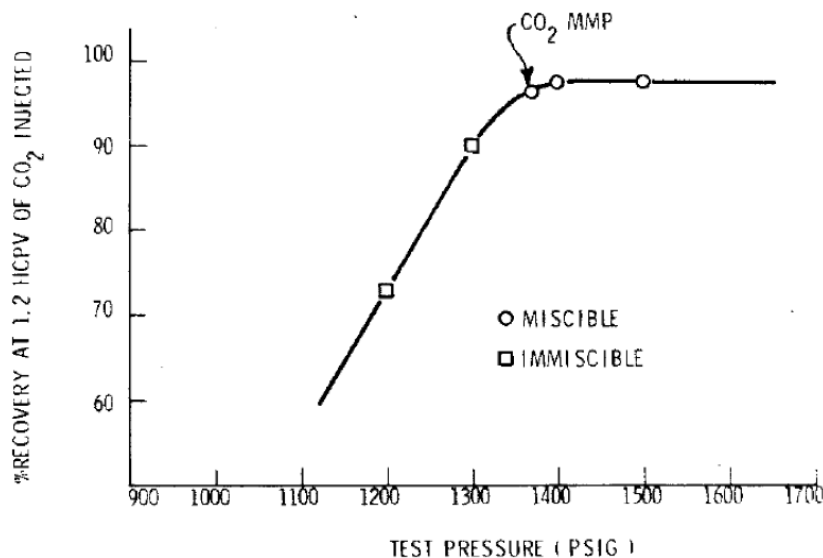
Figure 4.4 - MMP curve (Yellig and Metcalfe, 1980). Displacement pressures vs. recovery (%OOIP) are plotted after 1.2 pore volumes (PV) CO_2 injected. The plateau defines the MMP for the given oil composition.

Ternary phase diagrams determine if, and after how many contacts, miscibility may be achieved at given pressure (Farouq and Thomas, 1989). Figure 4.5 shows a ternary diagram illustrating first-contact and multiple-contact miscibility processes. The three corners of the diagram represent different compositions of the injected gas, from light (C_1), intermediate (C_2 - C_6) to heavy components (C_{7+}). The two-phase line encloses the region at which reservoir composition is both gas and liquid.

The two-phase line is divided into a dew point curve (upper) and a bubble point curve (lower) at the plait point. Above the dew point curve the reservoir composition is saturated with gas, and below the bubble-point curve the composition is saturated with liquid. The tangent to the two-phase region at the plait point is called the critical tie line.

31
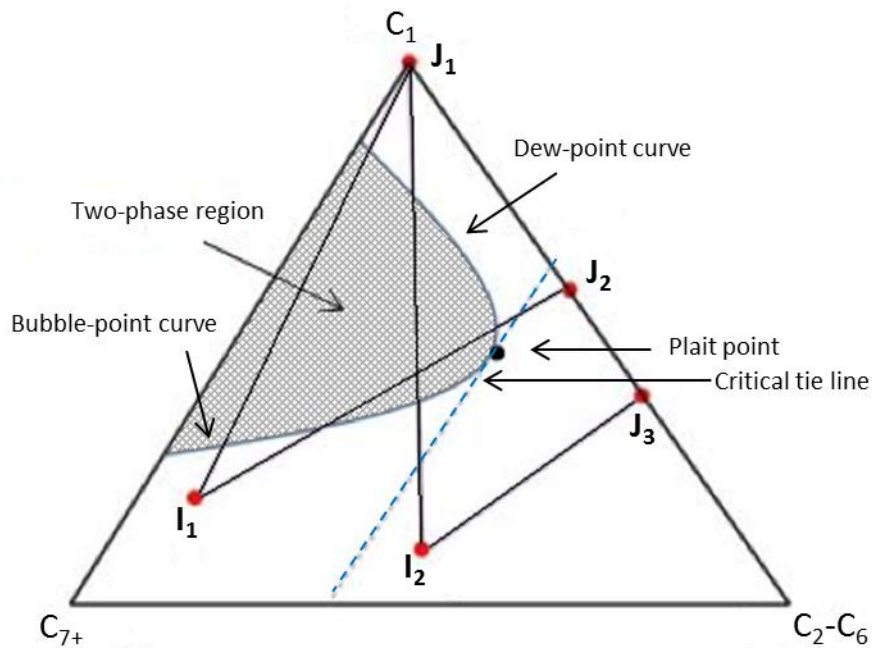
Figure 4.5 - Ternary phase diagram describing the different miscible processes. I_x and J_x are oil and gas compositions respectively. Dilution paths are shown for first-contact miscibility (I_2-J_3), vaporizing gas drive (I_2-J_1), and condensing gas drive (I_1-J_2). In addition, immiscible displacement with a dilution path crossing the two-phase region on the same side of critical tie line is illustrated (I_1-J_1). Modified from (Skarestad and Skauge, 2012).

A dilution path line connects the reservoir oil composition I_x to the injected gas J_x. If the dilution path crosses outside the two-phase region, as for (I_2-J_3) displacement will occur entirely within one phase. First-contact miscibility is achieved. However, if the dilution path crosses the critical tie line into the two-phase region, multiple-contact miscibility occurs (Skarestad and Skauge, 2012).

Multiple-contact miscibility can be either a vaporizing gas drive by (I_2-J_1) or a condensing gas-drive by (I_1-J_2) (Skarestad and Skauge, 2012). In a vaporizing gas drive, intermediate components from lighter reservoir oils are vaporized into the injected dry gas upon contact (Farouq and Thomas, 1989). In a condensing gas drive, components condense from an intermediate saturated gas into the heavy component reservoir oil. The latter is the case for miscible CO_2 injections performed in this thesis, in addition to first-contact miscibility.

4.2.3 Transport mechanisms during miscible displacement

Miscible displacements are influenced by mechanical transport of solutes (CO_2) through dispersion mechanisms (Perkins and Johnston, 1963). Dispersion is a process in which one phase is distributed within a bulk phase creating a continuous system due to molecular diffusion and/or convection transport (Delgado, 2007). During miscible CO_2 flooding, the bulk phase is the under-saturated reservoir oil and the dispersed phase is the injected CO_2. For low fluid velocities u, were $u \rightarrow 0$, dispersion is solely determined by molecular diffusion (Delgado, 2007). At higher velocities, dispersion becomes purely fluid mechanical, and is to a greater extent controlled by convection.

Dispersion is dependent on reservoir heterogeneity, and transport is therefore divided into longitudinal (direction of fluid flow) and transverse (opposite to fluid flow) dispersion (Perkins and Johnston, 1963). Transverse dispersion combines the effect of both molecular diffusion and convection in moving particles across streamlines. In longitudinal dispersion, particles are moved along streamlines by radial diffusion, but the effects are degraded as velocity profiles accelerate. At higher velocities, turbulence occurs causing the local fluids to mix. Transverse dispersion is therefore less effective than longitudinal ((Perkins and Johnston, 1963; Hart *et al.* 2012; Delgado, 2007).

Molecular diffusion is the constant irregular movement of gas molecules across an interface due to concentration differences between the phases (Perkins and Johnston, 1963). In a miscible displacement, the molecules within each phase will be equally attracted to their own kind as to the molecules within the opposing phase (Zolotukhin and Ursin, 2000). The molecular attraction is, however, greater in the more dense fluid, and a molecular pressure gradient will appear across the interface. The pressure gradient causes molecules to move and accelerate and eventually result in diffusion across the boundary zone. Due to the larger concentration of molecules in gas phase, diffusion continues until equilibrium is reached between the injected gas and reservoir oil. The interfaces vanish and miscibility is obtained Figure 4.6.
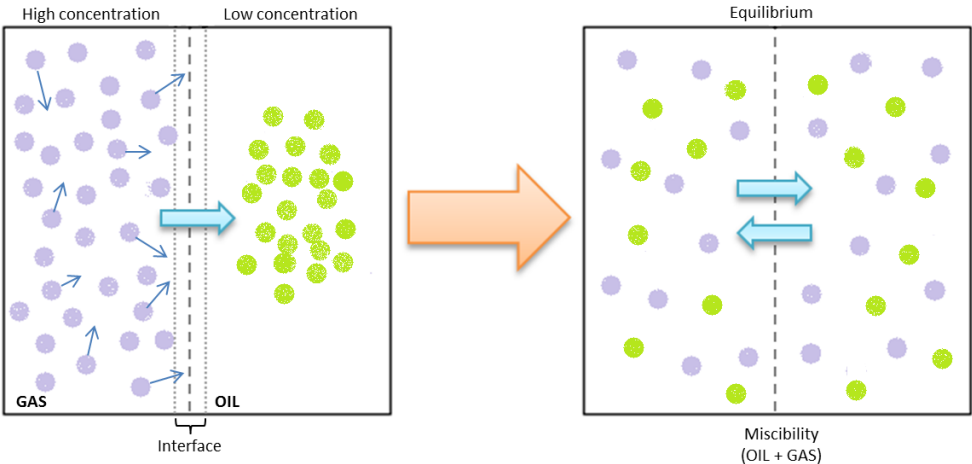
Figure 4.6 - Molecular diffusion. A high concentration of gas molecules is in contact with denser oil phase under miscible conditions. Due to the pressure gradient across the interface, and the irregular movement of gas molecules, a molecular diffusion process occurs. Diffusion stops as equilibrium and miscibility is achieved.

Convection occurs due to density gradients within the porous media (Ghorayeb and Firoozabadi, 2001). During miscibility, density will change as gas diffuse and mix with the oil phase. The density of the oil will decrease and the lighter composition will rise within the reservoir due to gravity forces. As a result, denser oil will replace the lighter composition, resulting in circulation of fluids from one region to another (Perkins and Johnston, 1963).

In fractured reservoirs, where channelling is likely to occur during CO_2 injection, molecular diffusion will be an important transport mechanism (da Silva and Belery, 1989). The diffusion process provides means for oil recovery by increased oil pressure due to swelling. For unconventional shale, where hydraulic fracturing provides the basis of permeability, molecular diffusion during miscible flooding is likely to have significant effect on enhanced oil recovery.

In cases of water shielding, where water saturation restricts contact between CO_2 and oil, molecular diffusion will contribute to displacement over time. Because CO_2 has the ability to diffuse through water, CO_2 will eventually reach the trapped oil, and swelling will displace the shielding water (Campell and Orr, 1985). This process is illustrated in Figure 4.7. This particular form of molecular diffusion through a water membrane is termed osmosis.
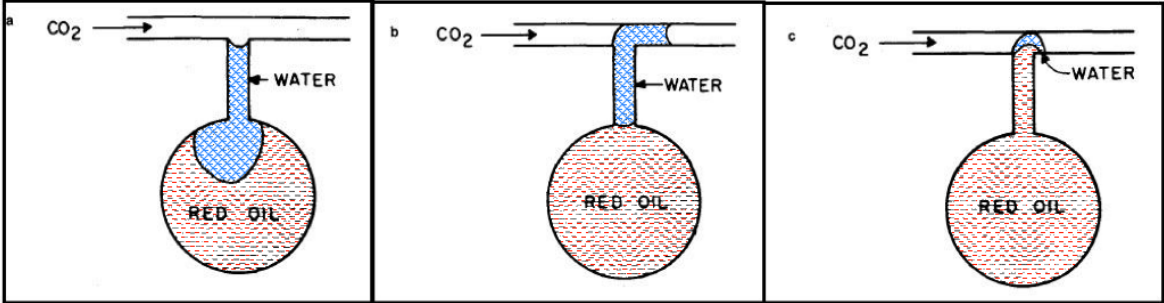
Figure 4.7 - Schematic illustration of oil swelling due to CO_2 molecular diffusion through water membrane. a) CO_2 is injected into the channel, but water shielding blocks contact between CO_2 and residual oil in dead-end pore, b) Due to molecular diffusion, CO_2 diffuse through the water membrane and oil starts to swell, c) The resulting oil expansion pushes the shielding water into the channel. Modified from (Campbell and Orr, 1985).

Part 2 – Experimental Setups and Procedures

All experiments presented in this thesis were conducted at the University of Bergen (UoB), Dept. of Physics and Technology. This part of the thesis lists the fluids and materials used when performing LSW in micromodels and miscible CO_2 injection in tight shale. The setup and equipment are described, and the preparations and procedures for executing the two experiments are reviewed.

5   Fluids and Materials

5.1   Fluids

Fluids used and their characteristics are listed in Table 5.1. Synthetic Brines A, B, and C were made specifically for the experiments related to low salinity waterflooding and osmotic mobilization. Mineral oils with different carbon numbers were applied to compare the osmotic effect on various oil compositions. During CO_2 injection, brine was not used because initial water saturation was already present. Shale cores were only saturated with oil. Both sets of experiments were based on refined oil tests (n-Hexane, n-Heptane and n-Decane) to investigate the effect of osmotic visualization and miscible CO_2 injection in systems of simple oil chemistry and single MMPs, before performing experiments by multi-component Ekofisk crude oil.

Table 5.1 - Fluid properties of oils, brines and CO_2 gas at experimental conditions

Fluid	Composition	Conditions	Density [g/cm^3][2]	Viscosity [cP][2]
n – Hexane	C_6H_{14}	1 bar, 25 °C	0.655	0.296
n – Heptane	C_7H_{16}	1 bar, 25 °C	0.680	0.388
n – Decane	$C_{10}H_{12}$	100 bar, 25 °C	0.734	0.951
		100 bar, 60 °C	0.709	0.609
Ekofisk crude oil[1]	53 wt.% HC	1 bar, 20 °C	0.849	14.5
	35 wt.% aromatics 12 wt.% resins 0.90 wt.% asphaltenes	1 bar, 60 °C	0.829 ± 0.014[3]	-
Brine A (high salinity water)	5 wt% NaCl	1 bar, 25 °C	-	-
Brine B (high salinity water)	20 wt% NaCl	1 bar, 25 °C	-	-
Brine C (low salinity water)	Distilled water	1 bar, 25 °C	0.997	0.890
CO_2 gas (5.0 purity)	> 99.999 % CO_2	100 bar, 25 °C	0.818	0.0739
		100 bar, 60 °C	0.290	0.024
		160 bar, 60 °C	0.638	0.050

[1] *Composition of Ekofisk crude oil obtained from (Graue et al., 1999).* [2] *Density and viscosity values are gathered from (NIST, 2011).* [3] *Density of Ekofisk Crude at 60°C was experimentally measured. The uncertainty was calculated by equation A5, Appendix A.*

CO_2 was used at various pressures and temperatures affecting its physical state. In experiments performed by CO_2 injection for oil production from low permeable shale, liquid CO_2 and supercritical CO_2 for miscible and multiple-miscibility displacement processes were applied.

5.2 Sandstone Micromodels

Sandstone micromodels representing a 2D porous media were used for visualizing pore scale mechanisms, such as fluid distribution and displacement processes, during osmotic mobilisation. The micromodels were constructed by etching structures from thin section analysis of Berea sandstone into Silicon wafers. The resulting pore structures and flow paths manufactured at specific depths were bonded to a glass plate allowing fluid flow and interactions to be studied through a microscope.

The high-resolution micromodels were constructed at the Stanford Nanofabrication Facility (SNF) using specialized imaging, etching and bonding techniques to represent a two dimensional section of a real porous media (Hornbrook *et al.,* 1991; Woody *et al.,* 1996). Detailed descriptions of the steps involved in manufacturing the micromodels are published by Hornbrook *et al.* (1991). The procedure consists of five steps; photography, digital manipulation, image mask construction, image transfer/etching, and model construction. A specialized deep-reactive ion etching (DRIE) technique is used to etch the two-dimensional pore network of Berea sandstone into the silicon wafer creating surface roughness on the vertical wafer walls (Buchgraber, 2012). The strongly water-wet

characteristic of the micromodel is obtained by a thin oxide layer that develops on the surface of the structure during bonding of the etched silicon wafer to its glass cover plate.

As described by Rangel-German and Kovscek (2006), four ports for either injection or production were drilled into the glass plate to connect with the porous network. In addition, two fractures were etched into the silicon wafer for observing matrix-fracture interactions. These fractures were located between the fluid distribution ports, one in the upper and one in the lower part of the porous media.

The two-dimensional silicon wafer micromodels fully represent typical Berea sandstone at a 1:1 scale (Rangel-German and Kovscek, 2006). Figure 5.1 shows a schematic of a fully constructed micro model. It visualizes the etched pore network, with the location of the four distribution ports relative to the lower and upper fractures. The grains within the pore network appear as "islands" and the etched pores and throats appear as "channels". The coordination number, *i.e.* the average number of flow entrance/exit paths from the pores, range from 1 – 5 (Gauteplass *et al.,* 2013).
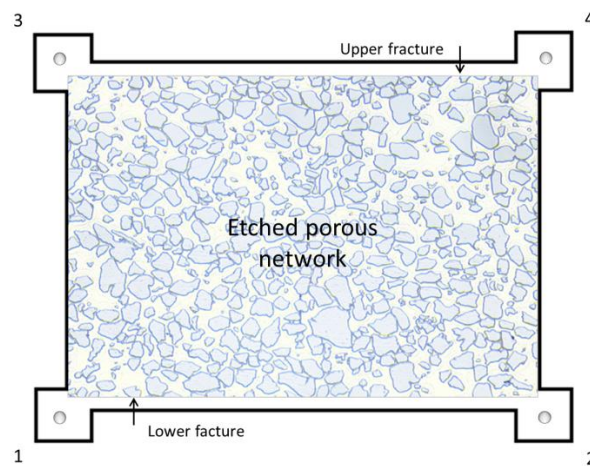
Figure 5.1 - Schematic of a micro model. The etched pore network is connected to the lower and upper fracture, which in turn is connected to the fluid distribution ports. Distribution ports are numbered 1-4. Either one of the ports can be used for injection or production depending on the boundary conditions for the experiments.

Scanning electron microscopy (SEM) images of the silicon micro models, show flow channels to be 25 μm deep, as shown in Figure 5.2 (a) (Rangel-German and Kovscek, 2006). Figure 5.2 (b) shows measured grain dimensions performed by Follesø (2012). The results ranged from 214.45 μm to 9.55 μm in a Berea sandstone micro model.
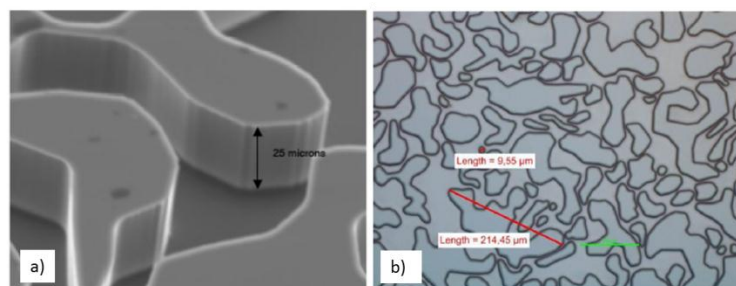
Figure 5.2 – (a) Depth measurements of a Berea sandstone silicon micro model by Scanning Electron Microscopy (SEM) images (Rangel-German and Kovscek, 2006), (b) Grain size measurements taken at 20x magnification to identify the grain size range in a Berea silicon micro model (Follesø, 2012).

Two types of silicon wafer models are used depending on pressure regime. These are titled respectively as low-pressure and high-pressure micromodels. The low-pressure models have low strengths and only small differential pressures (2-3 bars) can be applied across the models (Follesø, 2012). The high-pressure models can in theory withstand pressures up to 150 bars and be applied under a wider range of experimental conditions. The general properties regarding etching depth, grain size and coordination number are fundamental for size while porosity and permeability vary.

5.2.1   Low-pressure models

A picture of the low-pressure micromodel can be found in Figure 5.3 (a). The micromodel has a 5x5 cm^2 etched pore network (matrix), containing $3.5x10^5$ pores distributed across the area with a flow distribution channel (fracture) width of 1250 µm (Gauteplass *et al.,* 2013). The porosity measured on microscope images is 52 %, and the average matrix and fracture permeability are 700mD and 1500mD respectively (Follesø, 2012).
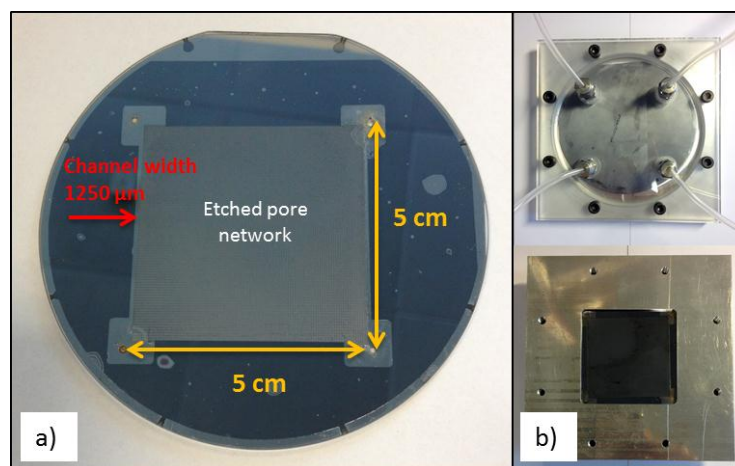
*Figure 5.3 - (a) Low-pressure micromodel with specified dimensions, (b) Low-pressure silicon micromodel mounted in aluminium-Plexiglas holder. The aluminium part has a window for studying the porous network, while the Plexiglas has distribution ports for injecting and producing fluids.*

When performing experiments with low-pressure micromodels, specially designed holders manufactured at the UoB Dept. of Physics and Technology are used (Follesø, 2012). These micromodel holders consist of two plates, one made of aluminium for positioning the model, and one made of Plexiglas with holes (ports) for injection and production. The aluminium plate is designed with a window through which the porous network can be studied, and the distance between the microscope objective and the model has been minimized. Small gaskets are located around the distribution ports in the Plexiglas plate to prevent leakage. The Plexiglas is placed on top of the micromodel and fastened. NPT fittings and tubing are connected to the four holes for injecting and producing fluids. A low-pressure silicon micromodel mounted in a holder is visualized in Figure 5.3 (b).

5.2.2   High-pressure models

A picture of a high-pressure micro model can be seen in Figure 5.4 (a). The dimensions of the pore network are 2,76x2.16 cm and the estimated porosity is approximately 60% (Høyland, 2014). The width of flow distribution channel is 715.5 µm. Permeability measurements were performed on fully assembled high-pressure micromodels by water injection using Darcy´s law (*cf.* equation 2.4, section 2.2.3). One assumption was made when calculating the matrix permeability: a radial displacement

was assumed and the length of the diagonal network was hence divided in two too represent the length of the matrix cross-section. The matrix permeability was calculated to be $3.3\pm0.1*10^{-1}$ D and fracture permeability 67.8 ± 0.3 D (*cf.* equation A2, Appendix 2 for uncertainty calculations).
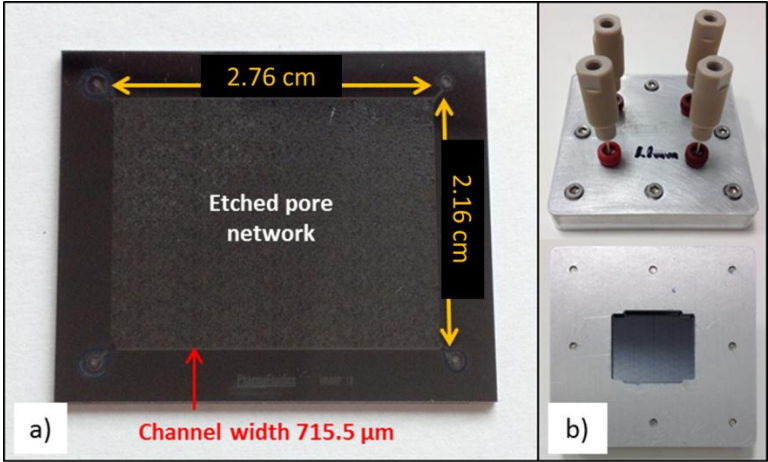
Figure 5.4 - (a) High-pressure micromodel with specified dimensions, (b) High-pressure micromodel mounted in aluminium micromodel holder. The bottom part has a window for studying the porous network, and the top part seals off the micromodel and has distribution ports for injecting and producing fluids.

Specific guidelines issued by the manufacturer were followed when assembling the high- pressure micromodels in their holders as shown in Figure 5.4 (b). Figure 5.5 shows the steps in assembling a 1.7mm high-pressure model. The mounting of the micromodel and the specific equipment used are described below.
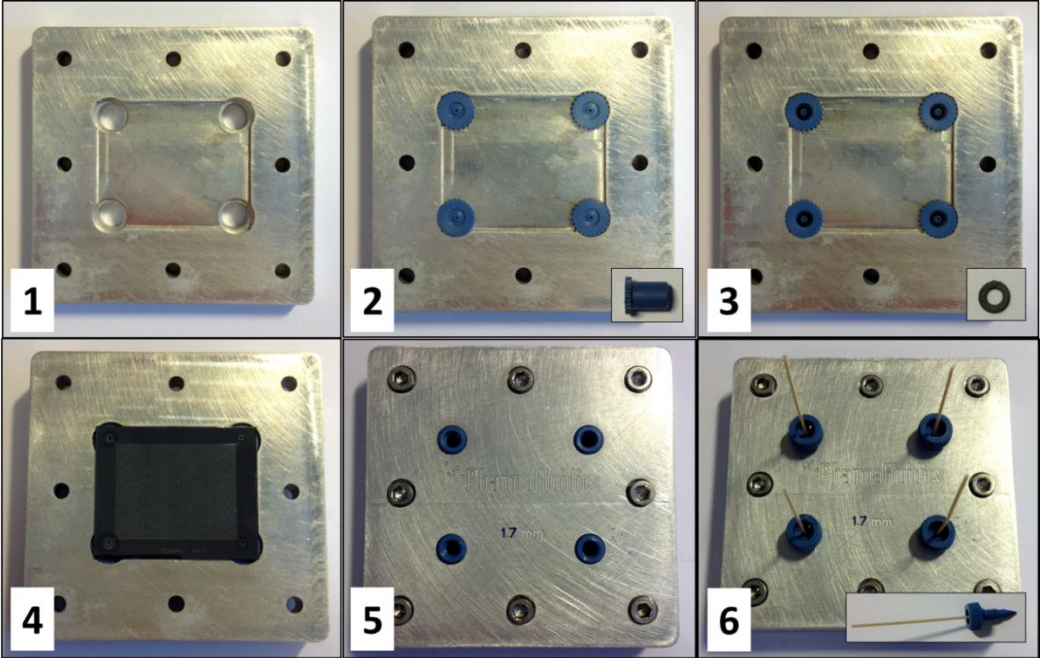
Figure 5.5 - Illustration of high-pressure micromodel assembly. 1) The top part of the aluminium holder is placed with the housing facing up. 2) Nano-ports are positioned in their respective holes. 3) Gaskets are located around the holes of the nano-ports. 4) The micromodel is placed with the silicon wafer facing up. 5) The bottom of the holder is positioned above the model, and fastened with screws. 6) A complete micromodel assembly is shown with 1/16 Peek tubing connected.

Step 1: All parts used in assembling the micromodel are thoroughly cleaned before mounting. Isopropanol is used to clean the different parts and compressed air is used to dry and blow away dust and particles.

Step 2: The female NanoPorts are placed in their respective holes in the top of the holder, and the bottoms of the NanoPorts are levelled with the surface of the micromodel chamber.

Step 3: 0.5 mm thick port gaskets (N-124-02) are placed into the recess surrounding the holes at the bottom of the NanoPorts. These gaskets are installed to prevent leaks and provide pressure resistance for the micromodel when mounting the parts together.

Step 4: The micromodel is placed on top of the gaskets with its silicon side facing up, precisely levelled with the edge of the aluminium holder.

Step 5: The bottom part of the holder, providing the window for observation, is placed on top of the silicon micromodel. Eight stainless steel screws are carefully finger-tightened to assemble the two aluminium parts, starting in adjacent corners.

Step 6: After finger-tightening the screws, a torque key is used to apply a momentum of 0.5 Nm, securing the two aluminium parts together. This is the maximum force that can be applied in order to not break the model.

Step 7: Male nuts with 360 µm O.D. capillary peek tubing were then finger-tightened to the female NanoPorts for fluid injection and production.

Time, testing and failures had to be taken into account when working with the high-pressure models. In assembling the holders the micromodels revealed great sensitivity to torque when securing the two aluminium parts together. When the micromodels were initially mounted, injection tests had to be performed to ensure that the models were assembled correctly (no leakage). Several pressure tests were also conducted to confirm that the models could withstand pressure at experimental conditions. In addition, manufacturing deficiencies were detected such as brittle distribution holes and misaligned fluid ports.

5.3 Tight-Shale Core Samples

Experiments investigating miscible flow and oil production from low permeable shale were conducted on three 1.5inch diameter reservoir shale samples received from a formation in the US. The samples were extracted from a formation of three structural layers, a middle-section of sand-and siltstones, a lower section source rock and an upper section seal of high organic content. Two of the shale cores, sample 3i and 4i, were unpreserved upon arrival, while shale core 12iA was kept semi-preserved in wax. It was assumed that the sample porosity ranged between 4-5%. All reservoir cores were measured and weighed upon arrival, and permeability values were estimated. The geometric properties can be seen in Table 5.2.

Table 5.2 - Geometric properties measured for the various shale cores

Core ID	Length [cm] ± 3E-03[1]	Diameter [cm] ± 2E-03[1]	Bulk volume [cm^3]	Porosity [%]	Pore volume [cm^3]	Initial weight [g] ± 0.01
12iA	2.450	3.820	28.08 ± 0.05	~ 5.0	1.40 ± 0.05	70.35
3i	3.798	3.796	42.98 ± 0.07	~ 4.8	2.06 ± 0.07	111.27
4i	3.923	3.796	44.40 ± 0.07	~ 4.5	2.00 ± 0.07	114.45

[1] Uncertainties are calculated based on equation A3, Appendix A.

Computed tomography (CT) scans of the rock structures for the three shale samples were obtained by the use of a medical CT scanner at Haukeland University Hospital (HUH) (Graue *et al.,* 2014). The high-resolution, X-ray computed tomography (CT) creates 2D sequential images of a given thickness, providing a 3D visualization of the media's structural composition when compiled together (Ketcham and Carlson, 2001). The 2D slices are created based on variation in X-ray attenuation from different angles, closely related to the objects density (Ketcham and Carlson, 2001). Regions and structures of higher density are identified by increased X-ray attenuation, while lower density regions are recognized by lesser amounts of reflected X-ray beams (Graue *et al.,* 2014).

The following image series, Figure 5.6, 5.7 and 5.8, are montages of CT-scans provided for shale cores 3i, 4i and 12iA respectively. The dark grey areas on the scans are lower-density regions, while the lighter areas are zones reflecting higher density (Graue *et al.,* 2014). The images are vertical slices of the samples taken continuously throughout the length of the cores. Only six slices from each shale sample are shown.

Shale core 3i
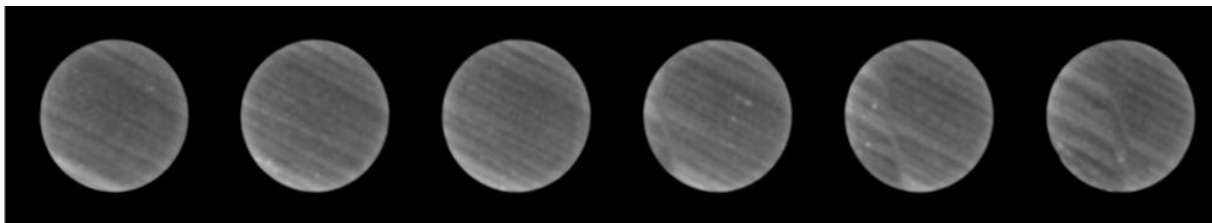
Figure 5.6 - Image montage of the CT-scans for shale 3i, each slice a 0.6mm thick representation of the sample. Low-density regions are observed as dark grey, while lighter areas reflect high-density regions. No distinct high-density zones are observed within the core. However, straight laminations dominate the sample, changing direction towards the end. Modified from (Graue et al., 2014).

Shale core 4i
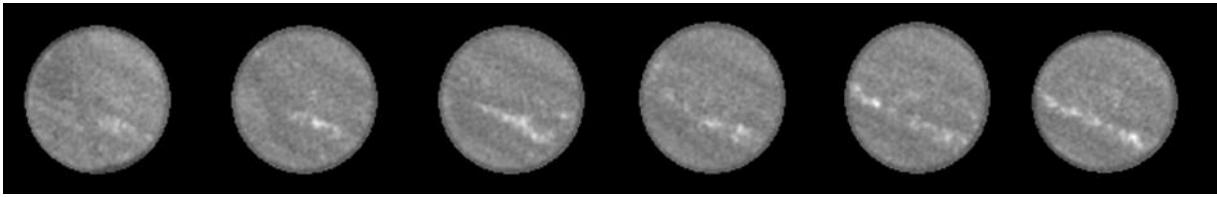
Figure 5.7 - Image montage of the CT-scans for shale 4i, each slice a 0.6mm thick representation of the sample. Low-density regions are observed as dark grey, while lighter areas reflect high-density regions. Both laminations and regions of high density are observed. Laminations are constant throughout the core. Modified from (Graue et al., 2014).

Shale core 12iA
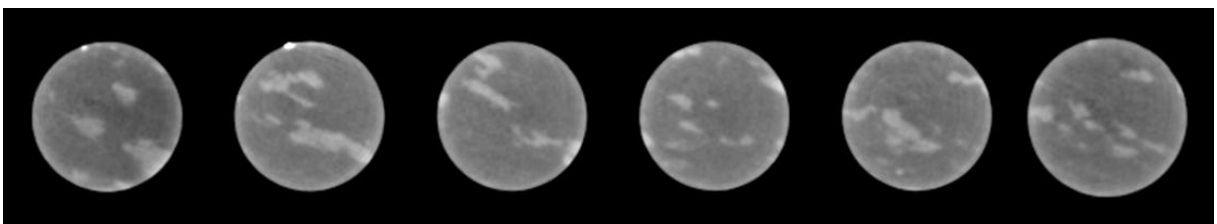
Figure 5.8 - Image montage of CT-scans taken for shale 12iA, each slice a 0.6mm thick representation of the sample. Low-density regions are observed as dark grey. Patchy zones of lighter grey high-density areas are prominent throughout the core. Modified from (Graue et al., 2014).

Generally, CT-scans can help indicate the presence of fluids within the rock structure. However, because of the tight shale matrix it cannot be concluded whether there are intitial fluids present from the images gathered.

6 Low Salinity Waterflooding in Sandstone Micromodels

In studying the effect of osmotic mobilisation by LSW, the experimental setup designed for pore scale micromodel flow and visualization at the Microfluidic Laboratory in Dept. of Physics and Technology, was used.

6.1 Setup and Equipment

A sketch of the experimental setup is shown in Figure 6.1. All experiments during osmotic diffusion were performed with the micromodel placed horizontally on the microscope.
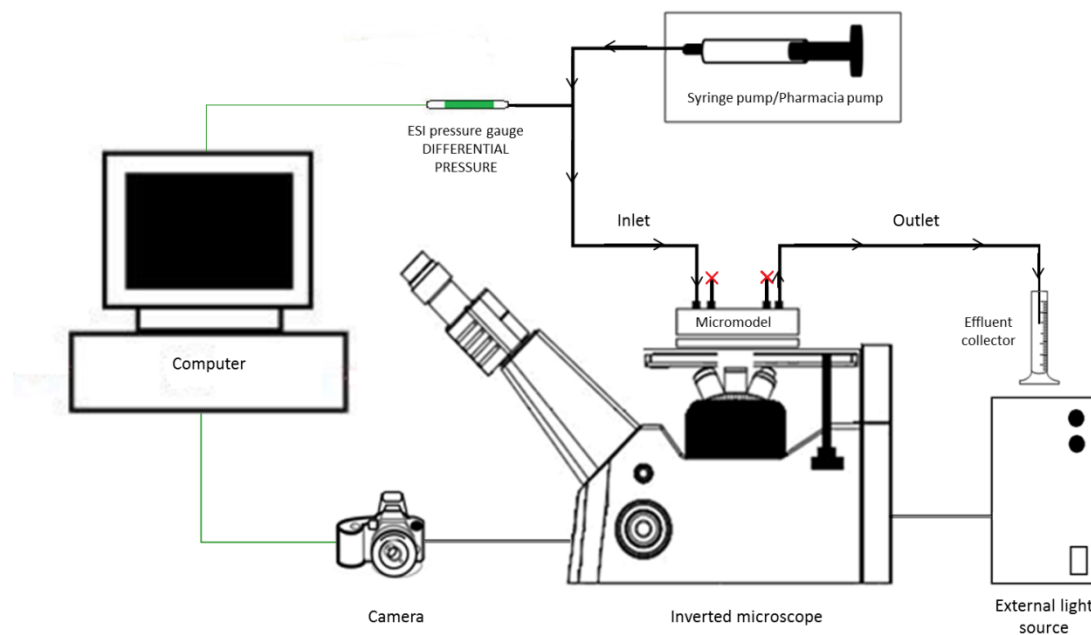
Figure 6.1 – Schematic of the microfluidic setup used for visualizing osmotic diffusion by low salinity water injection. The black lines are plastic tubing, and the arrows indicate fluid flow. The green lines are data cables connecting pressure transducers and high-resolution camera to computer for logging and monitoring.

6.1.1 List of equipment
- Nexus 3000 KR Analytical syringe pump
- Pharmacia LKB P-500 pump
- ESI Digital USB Pressure Transducers, range 0 – 4 barg (±0.10 %FS)
- Nikon Eclipse Ti-U Inverted Microscope
- Nikon Intensilight C-HGFI External Light Source
- Nikon DS-Fi1 Camera Head
- Nikon DS-U3 DS Camera Control Unit
- NIS-Elements D-Imaging Software 4.0
- Computer for controlling camera and pressure logging
- 1/16" plastic tubing and Swagelok fittings
- NanoPort assembly

6.1.2 Detailed description

After the initial mounting of the micromodel holder (*cf.* section 5.2) the model was placed on the rectangular mechanical stage of the Nikon Eclipse Ti-U inverted microscope (*cf.* Figure 6.1). The micromodel was positioned with observation window facing down, and distribution ports facing up. The field of view was operated by moving the mechanical stage in X and Y directions when turning the stage knobs. When the micromodel was placed on the stage, the inlet side of the micromodel was either connected to a Nexus syringe pump or a Pharmacia syringe pump for fluid injection.

The Pharmacia pump with two synchronized syringes was mainly used for injection rates of 1ml/h or higher during the initial saturation of the porous media. For all injection rates below that, the Nexus syringe pump was used as it had the ability to inject fluids at constant rates of minimum 0.00225 ml/h. Even though the Nexus pump provided a maximum injection limit of 3261.66 ml/h, the syringe had to be refilled manually as it contained only 25 ml. The Pharmacia pump was therefore used when continuous injection was required.

An ESI USB pressure transducer was connected to the setup on the inlet side of the micro model, and the differential pressure was logged on the computer. This was mainly to record the differential pressure across the model during the various injection steps and to monitor that pressures remained under the 2 bar limit for the low-pressure micromodels.

For studying the displacement processes within the micromodel, four different lens objectives were installed under the mechanical stage of the microscope. These four objectives had different magnification capabilities, providing 2x, 5x, 10x and 20x zoom respectively. In addition, 30x magnification was possible as the inverted microscope had a build-in 1.5x zoom, which could be added to the different objectives. The height and width of field of view for different objectives can be found in Table 6.1. An external light source was also connected to the microscope through an optic fibre cable. This light source delivered light to the microscope by an incorporated shutter, with six levels of adjustable light intensity ranging from 3%-100%.

Table 6.1 - Study areas for different objectives installed on the microscope (Follesø, 2012).

Objective lens	Height (µm)	Width (µm)
2x	4629.6	6167.3
5x	1854.3	2470.3
10x	929.7	1238.5
20x	470.6	626.9

To study osmotic mobilisation during low salinity waterflooding, a field of view 5x-zoom was generally chosen. The Nikon camera head captured the processes studied by taking time-lapse image sequences controlled by the Nikon NIS-Element D Imaging Software and camera control unit. The camera head was a 5-megapixel CCD camera, taking pictures at a maximum of 1 frame per second when capturing images of 1280 x 960 pixels with 8bit RGB pixel depth. Generally, time-lapse images would vary between 10 seconds or 15 minutes depending on whether it was initial saturation, primary drainage or osmotic diffusion that was recorded.

6.2 Preparations and Procedures

The experimental work performed on micromodel visualization of osmotic gradient was done in collaboration with fellow master student Arthur Uno Rognmo and PhD candidate Jarand Gauteplass.

6.2.1 Experimental conditions
Several experiments were conducted on both low -and high-pressure micromodels to study osmotic mobilisation by LSW. Different experimental conditions were applied, such as changing the oil and brine compositions between experiments. Table 6.2 lists an experimental overview of fluids injected for the different displacement processes during the experiments.

Table 6.2 - Overview of experiments and the various fluid injections for the different displacement processes during osmotic diffusion

Micromodel ID	High salinity brine flooding	Primary drainage	Low salinity water injection	Baseline
LPM 1	Brine B	n-Heptane	Brine C	Yes
LPM 2	Brine A	n-Heptane	Brine C	No
LPM 3	Brine A	n-Hexane	Brine C	No
LPM 4	Brine B	n-Hexane	Brine C	No
LPM 5	Brine A	Crude oil	Brine C	Yes
HPM 1	Brine A	Crude oil	Brine C	No
HPM 2	Brine A	Crude oil	Brine C	No

As can be seen from Table 6.2, two different brine compositions were used in the refined-oil experiments (Brine A and B), while the brine for the crude oil experiments was kept constant (Brine A). Two different sets of baselines were performed. The first baseline was based on osmotic diffusion through a refined oil membrane (n-Heptane and n-Hexane), while the second was through a crude oil membrane.

6.2.2 General boundary flow conditions
Different port configurations were applied for the various steps performed during LSW. The opening and closing of injection and production ports depended on the pressure differences across the porous network, and whether or not air was trapped within the micromodel. The different port combinations controlled fluid displacement through the model. The most frequently used boundary flow conditions and their effect on displacement are illustrated and described below. All injections were performed with the micromodel positioned horizontally on the surface.

Diagonal production (DP)

The diagonal production port is opened to induce flow through matrix (*cf.* Figure 6.2). The injected fluid displaces initial gases and/or liquids first along the lower fracture. As pressure builds up forced imbibition is induced into the matrix and the initial phase is diagonally displaced by co-current flow towards the upper right production port.

Figure 6.2 - Diagonal production. Fluid enters the micromodel through the lower left injection port, displacing fluids in the lower fracture into matrix as indicated by blue arrows. Fluids are then displaced diagonally across the matrix visualized by green arrows.

Horizontal production (HP)

The horizontal production port is opened to displace initial phase from the lower fracture, and continuously from matrix by spontaneous imbibition and counter-current displacement (*cf.*Figure 6.3). Both production ports in upper fracture are closed so only the lower part of the matrix is affected by the counter-current displacement back into lower fracture.
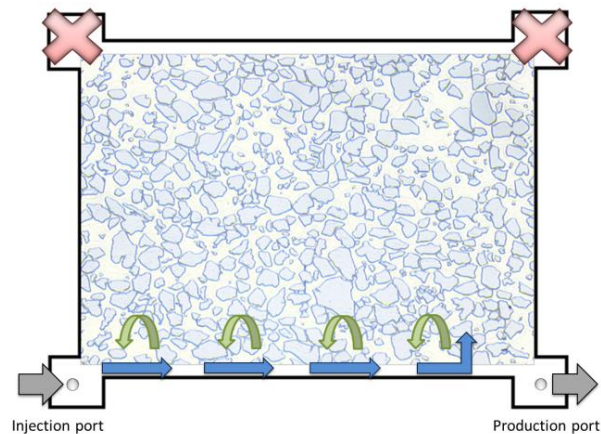
Figure 6.3 - Horizontal production. Fluids enter the micromodel through the lower left injection port, displacing the initial phase in the lower fracture (blue arrows) followed by spontaneous imbibition and counter-current displacement indicated by green arrows.

Horizontal and diagonal production (HDP)

Both the horizontal and diagonal production ports are opened so high injection rates can be implemented without creating large differential pressures across the micromodel. The injected fluid displaces the lower fracture first and then the matrix by spontaneous imbibition. The initial phase is displaced both co-currently towards upper the right production port, and counter-currently towards the lower right production port.
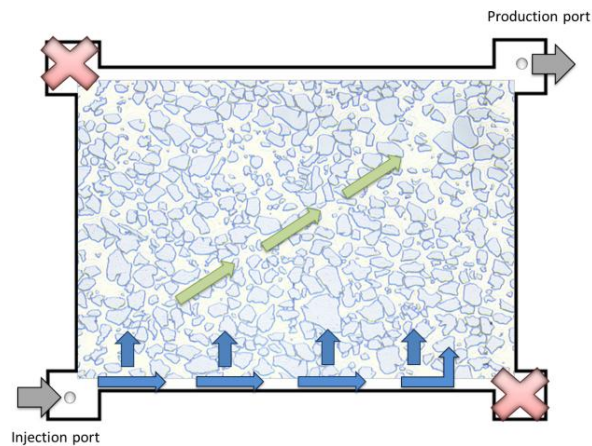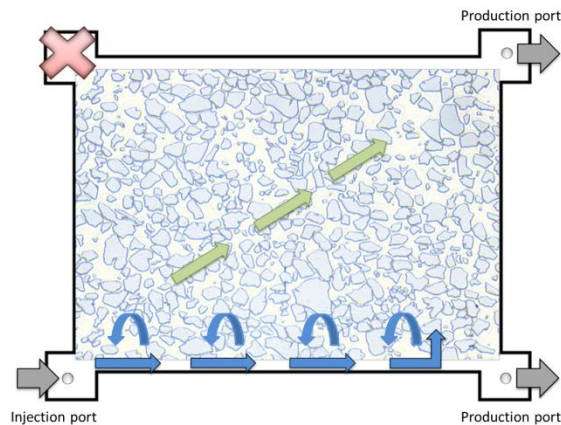
Figure 6.4 - Horizontal and diagonal production. Fluid enters the micromodel through the lower left injection port, displacing the lower fracture and the matrix through spontaneous imbibition. Blue arrows illustrate displacement of initial fluid through the lower fracture and counter–current flow in matrix. The green arrows visualise co–current displacement through the matrix.

<u>Gravitational displacement</u>

The micromodel is placed vertically to induce gravitational displacement. The method is applied if residual air is left within the model after initial saturation, or if unwanted air bubbles are injected into the model. Gravitational displacement is effective in displacing air due to the density difference between the fluids inside the porous network. Air will rise to the upper fracture and be produced through the upper right production port in favour of the other fluids present.

6.2.3 Initial high salinity water saturation

Due to the water-wet nature of the silicone micromodels, the injected brine displaced air from the fracture while spontaneously imbibing into the matrix by HDP. Water breakthrough was observed seconds after injection-start due to the small pore volume of the models. Injection rates are listed in Table 6.3. For improved sweep across the matrix DP was applied to force the waterfront to move diagonally through the porous media, and finally to obtain 100% saturation, capillary-trapped air was removed by GP.

Depending on experimental conditions, high salinity Brine A or B was used for the initial saturation process. 100% saturation was generally achieved after 24 hours, depending on the boundary flow conditions and injection rates applied. For all injections into the low-pressure micromodels, the 2 bar pressure limit were maintained. Hence, the initial saturation time was longer compared to the high-pressure micromodels. Average injection rates applied and their corresponding boundary flow conditions are listed in Table 6.3. 100% water saturation was visually verified through the inverted microscope.

Table 6.3 - Average injection rates applied during initial high salinity saturation and their corresponding BFC

Micromodel	HDP	DP	Gravitational displacement
Low-pressure	2 ml/h	1 ml/h	0.2 ml/h
High-pressure	5 ml/h	3 ml/h	1 ml/h

6.2.4 Primary oil drainage

After initial water saturation with high salinity brine, primary oil drainage was performed on the micromodels by HDP. After oil breakthrough in the lower fracture, the horizontal production port was closed and DP applied. The injection rate was set to 0.7 ml/h for oil injection in both low -and high-pressure micromodels, controlling the propagation of oil through the porous network. By keeping a constant injection rate, the oil pressure within the lower fracture would increase until it exceeded the threshold pressure of the porous media. Oil would then start to enter the largest accessible pores first where the capillary pressure would be lowest, displacing the initial high salinity brine co-currently.

Primary drainage was completed when the lower part of the matrix was predominantly saturated with oil, while the upper part of matrix contained a high brine concentration. This continuous oil layer represented the semi-permeable membrane separating the initial high salinity brine from the injected low salinity water during osmotic diffusion. The primary drainage process took 10-30 minutes depending on the pore volume of the micro models.

6.2.5 Secondary high salinity waterflooding

High salinity brine at original concentration was re-injected into the partially saturated micromodel by HP. The brine spontaneously imbibed into the matrix due to the strongly water-wet wettability preference. High salinity water saturation increased while oil was counter-currently displaced and produced through the lower fracture.

Secondary high salinity water flooding was initially performed at 2 ml/h to displace oil from the fracture. When sufficient amounts of oil had been produced, the injection rate was lowered to 0.1 ml/h allowing spontaneous imbibition to act as the main driving force. As spontaneous imbibition seized and capillary pressure reached zero, secondary recovery was completed. The process of re-injecting high salinity brine lasted approximately 24 hours for both high -and low-pressure micro models.

6.2.6 Low salinity water injection into lower fracture

High salinity brine in the lower fracture was then replaced by injecting low salinity water, Brine C in Table 5.1 by HP. Only high salinity water within the fracture was displaced due to ceased spontaneous imbibition. In addition, lack of differential pressure across the matrix by HP created no oil mobilization during brine exchange in the fracture. However, an osmotic gradient was formed between the high salinity brine in the matrix and the low salinity water in fracture, separated by the continuous semi-permeable oil membrane. Low salinity injection lasted at average for 3 hours at a rate of 0.5 ml/h.

6.2.7   Osmotic diffusion and oil mobilization

After establishing an osmotic gradient, the diffusion process was monitored by the inverted microscope. Time-lapse pictures were taken every 15 minutes within a chosen field of view. By HP the injection rate was lowered to 0.042 ml/h, equivalent to 1 ml/day, in order to maintain a "fresh" flow of low salinity water to preserve the osmotic gradient. In addition, a constant flow of low salinity water prevented direct transport of salt ions between the different water concentrations. The only contact possible between the high salinity brine and the low salinity water would be by osmotic diffusion through the semi-permeable oil membrane. The diffusion process was set to develop for 7–14 days.

Prior to performing osmotic mobilisation experiments, baseline tests were carried out. The purpose was to document the absence of an osmotic gradient. It is predicted that when implementing an osmotic gradient, the mobilization of oil will be an effect of osmotic diffusion only. During the baseline tests, high-salinity brine at 0.042ml/h replaced low salinity water in lower fracture. Baseline tests were performed on micromodels primary drained by refined oil, the results representative for all experiments conducted under these conditions. In addition, when introducing Ekofisk crude as the oil phase, new baselines were performed. The baseline experiments were set to last approximately the length of the osmotic diffusion experiments.

7 Miscible CO$_2$ Injection in Shale Core Samples

An experimental setup was constructed at the Dept. of Physics and Technology with the purpose of performing high-pressure miscible CO$_2$ injections into low permeable shale. The setup was assembled using appropriate Swagelok tubing, fittings, and high-pressure Autoclave valves for executing high-pressure injections. The rig was build inside a heat cabinet to simulate reservoir conditions.

7.1 Setup and Equipment

A schematic illustration of the high-pressure setup is shown in Figure 7.1. All experiments were conducted by horizontal CO$_2$ injection. The Back Pressure Regulator (BPR) was placed inside the cabinet to avoid large pressure and volume fluctuations as liquid and supercritical CO$_2$ converts back into CO$_2$ gas at ambient pressure and temperature.
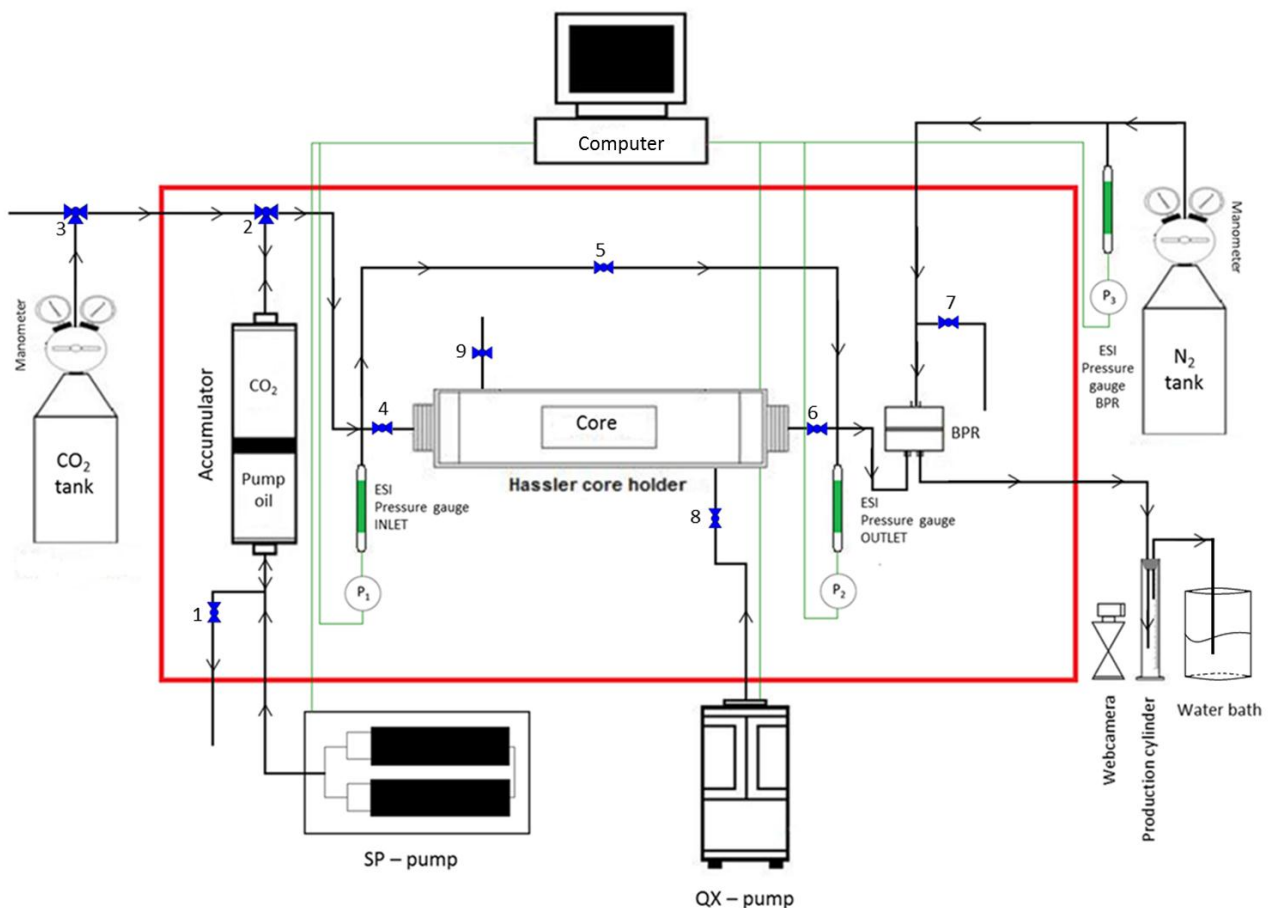
Figure 7.1 - Schematic illustration of the high-pressure setup for liquid and supercritical CO$_2$ injection into low permeable shale. The red square represents the heating cabinet in which the experimental setup was build. All the equipment, except for pumps, gas tanks and the production cylinder was positioned inside the cabinet. The black lines illustrate the tubing and the various flow lines. The arrows show the flow path through the tubing and core. Valves labelled 1 – 9 are illustrated in blue. The green lines are data cables connecting pressure transducers and pumps to a computer for logging, and operational purposes.

7.1.1 List of equipment

- Autoclave valves and crossings for high-pressure injections
- 1/8" steel tubing and Swagelok fittings
- Oiltech EHP2-S-0010-210-100 stainless steel piston accumulator (Max. volume 1.2L, max. pressure 375 bar)
- Equilibar HC276-5 Precision Back Pressure Regulator (Max. pressure 200 bar)
- N_2 tank (Max. pressure of 160 bar)
- CO_2 tank (Max. pressure of 60 bar)
- Computer for controlling pumps and pressure logs
- 3 x ESI Digital USB Pressure Transducers, range 0 - 400 barg (±0.10%FS)
- 1.5" Hassler type core holder - RCHR series (Max. pressure 7000 psi, max. Temp. 350°F).
- Quizix SP 5200 pump
- Quizix QX-6K-SS pump
- Web camera monitoring production
- 50 and 10 ml production cylinders

7.1.2 Detailed description

When an experiment required elevated temperatures, the cabinet was set to desired heat. In addition, a backpressure of either 100 or 160 bars N_2 was set during this period to investigate potential leaks at the BPR (valve 7 closed) in Figure 7.1. An ESI USB pressure transducer was connected to the line from the nitrogen-tank, logging the backpressure P_3 for verification purposes. When the system was stabilized the shale sample was mounted within the 1.5" Hassler core-holder. The shale core was isolated by closing inlet-valve 4 and outlet-valve 6. A confinement pressure was then applied by the Quizix QX pump located outside the cabinet. The pump injected distilled water into the confinement through valve 8 with valve 9 closed, until an initial confinement pressure was reached. Distilled water was used in confinement instead of pump-oil to avoid mixing of oils (pump-oil and crude oil) if leaks were to be detected through the sleeve.

CO_2 was injected from the tank located outside the cabinet through valve 3, and (the two-way) valve 2 into the accumulator. As CO_2 filled the accumulator, the CO_2 pressure displaced the piston towards the bottom of the buffer, displacing all excess pump-oil located below through valve 1. Valve 1 was then closed, and the CO_2 tank shut off. By opening valve 2 towards the system, with bypass valve 5 open (inlet valve 4 and outlet valve 6 still closed), CO_2 pressure was logged by the inlet P_1 and outlet P_2 ESI USB pressure transducers. Any leaks through fittings or crossings would be evident at this time and hence sealed. The CO_2 system would be left to thermodynamically stabilize for experiments at elevated cabinet temperatures.

After reaching equilibrium, the inlet 4 and outlet 6, valves to the core holder were opened. The CO_2 was now in direct contact with the inlet and outlet ends of the shale core. CO_2 was then pressurized to BPR pressure by injecting pump-oil from the Quizix SP pump into the bottom of the accumulator where the oil and CO_2 were separated by a moving piston. As the CO_2 pressure exceeded the BPR pressure, CO_2 escaped through the BPR and into a water bath located outside the cabinet. The bypass (valve 5) was then closed. The CO_2 pressure was further increased at the inlet, setting up a differential pressure across the core to induce flow through the sample. The net confinement

pressure was always maintained at least 60 bars above inlet CO_2 pressure to ensure CO_2 flow through the core.

As CO_2 penetrated the core sample, it mixed with the resident oil and the mix was displaced towards the outlet. Produced oil was collected outside the cabinet in the production cylinder, and monitored by web camera. For long injection tests the accumulator was re-pressurized several times to continue CO_2 injection and oil recovery, or for logging CO_2 injection rate at different conditions.

After completing the experiment, the system was depressurized by stopping the Quizix SP pump. With the inlet, outlet and bypass valves open, valve 1 at the base of the accumulator was carefully opened. Pump-oil was drained as the piston was pushed to the bottom of the buffer. Net confinement was also decreased simultaneously during this step. As the accumulator was emptied, the N_2-tank maintaining backpressure was closed, and the pressure was carefully released by valve 7. As the backpressure fell below the system CO_2 pressure, CO_2 was produced through the BPR. This continued until the backpressure reached atmospheric pressure and there was no CO_2 left in the system.

After the shale core was removed from the holder, end-pieces, tubing and BPR were cleaned. Tubing and end-pieces were flooded by n-Decane, which was then displaced by compressed air followed by CO_2 gas. The BPR was opened and excess oil removed manually.

7.2 Preparations and Procedures

The experiments conducted on miscible CO_2 injection and oil production from reservoir shale were carried out together with master student Arthur Uno Rognmo.

7.2.1 Experimental conditions

CO_2 injection was performed on n-Decane and crude oil saturated shale cores under various temperature- and pressure conditions investigating flow capacity and potential oil production. Table 7.1 lists the experimental conditions under which the various experiments were executed, in addition to saturation fluid and the physical state of the injected CO_2 gas.

All injections were performed at constant differential pressure, inducing flow through the core, knowing that the low permeability of shale could result in extremely high-pressure levels if exposed to constant injection rates. The induced CO_2 injection rate was logged during the experiment to be used when estimating the effective CO_2 permeability. The constant pressure injections were held within the pressure limitations of the experimental equipment.

Table 7.1 - Experimental conditions as performed for the various shale cores, including saturation fluid and CO_2 state.

Core ID	Saturation fluid	Temp. [°C]	CO_2 state	Differential pressure [bar] ±0.57[1]	Confinement pressure (above inlet) [bar] ±0.83	Absolute pore pressure (inlet) [bar] ±0.4
12iA_1	n-Decane	25	Liquid	55.49	73.96	162.1
				77.86	82.10	183.9
12iA_2	n-Decane	25	Liquid	58.64	59.96	160.0
				79.74	59.81	180.2
12iA_3	n-Decane	60	Supercritical	72.33	59.41	169.6
12iA_4	Ekofisk crude oil	60	Supercritical	70.04	90.10	222.9
				68.93	91.08	221.9
3i_1	Ekofisk crude oil	60	Supercritical	70.48	80.42	222.9
				70.19	82.28	229.6
				39.90	112.39	199.6
				29.52	122.48	189.5
				29.49	122.47	189.5
3i_2	Ekofisk crude oil	60	Supercritical	68.18	90.00	222.0
				67.82	87.95	222.0
				70.88	89.90	225.1
4i_1	Ekofisk crude oil	60	Supercritical	67.74	90.43	229.6
				67.76	90.38	229.6
4i_2	Ekofisk crude oil	60	Supercritical	69.16	89.91	223.1

[1] Uncertainty is calculated by equation A4, Appendix A.

Shale core 12iA was the only sample that was saturated by n-Decane, with experiments performed at room temperature and liquid CO_2 injection (*cf.*Table 7.1). The main purpose of saturating sample 12iA with n-Decane was to investigate whether it was possible to obtain oil recovery from tight reservoir shale by first-contact miscible CO_2 injection. For 12iA_1 and 12iA_2, miscible CO_2 injection was performed at differential pressures of approximately 60bar until oil production ceased. The pressure was then raised to 80bar for additional oil recovery. Subsequently, for injection 12iA_3, the temperature was elevated to 60°C to examine the effect of elevated temperature on recovery.

After conducting the initial experiments with n-Decane, supercritical miscible CO_2 injection was performed on all samples saturated with Ekofisk crude oil (*cf.* Table 7.1). The temperature was kept constant at 60°C with a differential pressure of approximately 70bar for all injections, and a net confinement pressure of at least 60bar. For experiment 3i_1, the differential pressure was lowered to 40 and 30 bar respectively to maintain a continuous CO_2 injection over time. Some discrepancies are seen for the average differential pressures applied in the crude oil experiments. In Table 7.1, the differential pressures range between 67-71bar for the different CO_2 injections. The variations are caused by instabilities in the backpressure regulator (BPR).

7.2.2 CO_2 gas permeability estimates in tight shales

During miscible CO_2 injection, one objective was to estimate sample permeability by CO_2. When CO_2 is injected for potential oil production, it will flow through the core with relative permeability to the oil phase until miscibility is achieved. At the end of recovery, when the majority of the residual oil has been produced, CO_2 will be the only phase flowing through the porous network. Hence, an end-point effective permeability can be calculated for CO_2 equivalent to shale flow capacity.

7.2.3 3D saturation of shale cores

Previous studies conducted by Opdal (2014) and Bø (2014) within the Reservoir Physics group at the Dept. of Physics and Technology (UoB) addresses a "best practice" re-saturation method for saturating dry reservoir shale cores. The procedures investigated were based on dynamic and static re-saturation, the results yielding 7-9% increased oil saturation for cores subjected to the static approach (Opdal, 2014; Bø 2014). Compared to dynamic saturation, where fluids are flooded through the core, the static method provides 3D-saturation covering the whole surface of the core increasing contact area and hence saturation of the sample. In re-saturating shale cores used in this thesis, static saturation was therefore conducted on all samples before miscible CO_2 injection was performed.

In the static approach shale cores were placed within an accumulator and immersed with the desired saturation fluid. Depending on whether the saturation fluid was n-Decane or Ekofisk crude oil, the accumulator was placed at room temperature or in a heating cabinet at elevated temperatures.

At ambient temperature, shale cores were saturated with n-Decane by pressurizing the accumulator to 100bar. No temperature elevation was required as viscosity and density of n-Decane at room temperature was sufficiently volatile in entering the porous media. Shale cores saturated with Ekofisk crude oil were pressurized to 200bar at 60°C inside a heat-cabinet to maintain its reservoir composition, as crude oil is known to precipitate wax at room temperature. In addition, elevated temperature and pressure yields reduced viscosity and density for crude to penetrate the porous network.

When determining the oil saturation of the shale cores, the accumulator containing the samples was depressurized and the saturated cores were weighed. When the samples had obtained a constant weight increase, it was concluded that maximum oil saturation was reached. To calculate the saturation, the dry and saturated weights of the shale cores were measured. Oil saturation was then determined by the following equation,

$$S_o = \frac{m_s - m_d}{V_b \cdot \phi \cdot \rho_{oil}}$$

(7.1)

Where S_o is the calculated oil saturation, m_d is the dry weight of the sample [g], m_s is the saturated weight [g], V_b is the sample bulk volume [ml], ρ_{oil} is the density of the oil [g/ml], and φ [%] is the porosity of the sample.

The properties of the different shale core samples are listed in Table 5.2. The saturation process took approximately 2-4 days before maximum saturation was reached.

7.2.4 Oil recovery by weight and volumetric production

It was attempted to record oil production during both liquid and supercritical CO_2 injection by measuring the oil production flashed at the outlet as a function of time. A web camera was placed next to the production cylinder, illustrated in Figure 7.1, to record oil production. In logging recovery versus time, CO_2 injection commenced when experimental conditions had stabilized after the initial CO_2 pressurization. The differential pressure across the core at this point created flow through the sample, mixing the CO_2 phase with the oil and displacing it towards the outlet. In addition, the injected CO_2 pore volume was recorded against the oil volume produced. Profiles illustrating dynamic production were made from the collected data.

Continuous miscible CO_2 injection into low permeable reservoir shale is assumed to yield little oil recovery due to low injectivity and low permeability of the rock. To provide a better estimate of oil recovery compared to what was visualized through volumetric production, weight measurements were recorded both before CO_2 injection and after. From Equation 7.1, the total oil saturation produced was calculated, and further oil recovery in terms of percent original oil in place (%OOIP) was determined by,

$$R_f(\%OOIP) = \frac{S_o - S_{o,after}}{S_o} \cdot 100\%$$

(7.2)

Where R_f is the recovery factor, S_o is the oil saturation after 3D-saturation and $S_{o,after}$ is the oil saturation after miscible CO_2 injection. When calculating oil recovery it is assumed that all reductions in weight are solely the result of oil production during CO_2 injection.

Part 3 - Experimental Results and Discussion

This part, presents results and discussions from the experiments performed in this thesis. Chapter 8 describes the observed water growth and oil mobilization by LSW in sandstone micromodels. Chapter 9 presents the permeability measurements and oil recovery factors obtained by miscible CO_2 injection in tight shale. Uncertainties are also presented and discussed.

8 Osmotic Diffusion during Low Salinity Waterflooding

Two alternative scenarios for osmotic diffusion by LSW were investigated. The first set was based on a refined oil membrane to investigate osmotic behaviour through a one-component oil phase. These experiments involved two different refined oils and various high salinity brines. The second set was based on Ekofisk crude oil to observe osmosis through a crude oil membrane. Baselines were established for each scenario. The results are captured in image sequences, zoomed-in and cropped to focus on fluid-fluid interactions in specific parts of the micromodels. Images are in some cases modified to highlight contrasts between water, oil and solid grains.

The following sections 8.1 to 8.4 describe the results from performing LSW. First, baseline tests in absence of a salinity gradient are presented for both the refined and crude oil experiments. Subsequently, results of osmotic diffusion are presented for the two different systems (*i.e.* refined oil and crude oil) when injecting low salinity water. The effects of using different high salinity brines and oil compositions are described in detail during the refined oil experiments. The experiments with crude oil are then reviewed and finally an overall summery is presented in section 8.5, where results are compared to relevant literature data.

8.1 Baselines - No Salinity Gradient

A baseline test was carried out to establish fluid movement without an osmotic gradient present. The same conditions were used as during low salinity water injection (*cf.* section 6.2.6), but high salinity brine replaced low saline water in the fracture. It was anticipated that there would be no movement of interfaces or mobilization of oil in matrix and fracture in the absence of an osmotic gradient.

8.1.1 Refined oil baseline

Figure 8.1 shows the results from the refined oil baseline with a resident (connate) brine concentration of 20wt% NaCl (Brine B, Table 5.1). The images were taken before (at 0 hours) and after (at 3 days 20 hours) continuous injection of Brine B. No change in saturation distribution was observed. The 20wt% NaCl was the highest salinity brine concentration investigated and was set to represent the refined oil baseline for subsequent LSW tests. No expansion of oil phase was detected when lowering the injection rate to osmotic diffusion rate (0.042 ml/h).
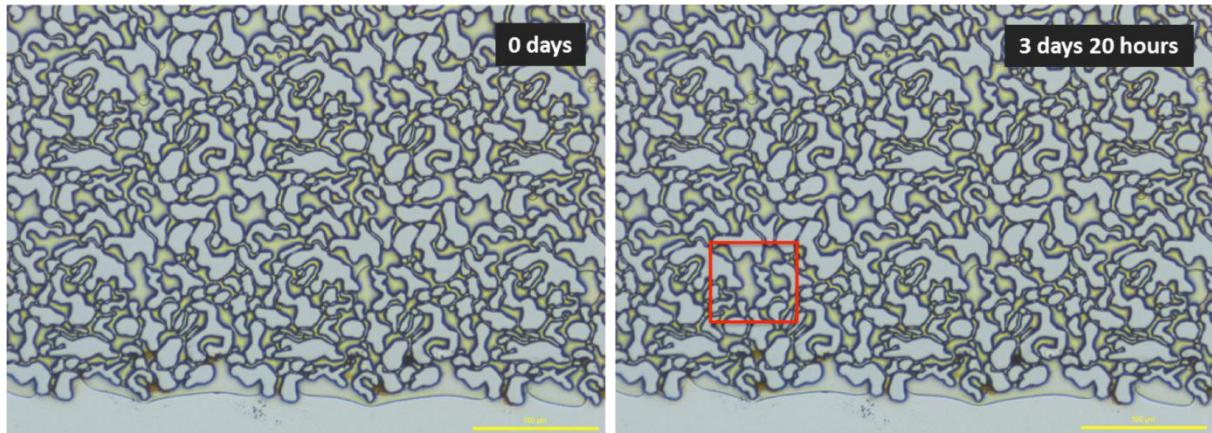
Figure 8.1 - Refined oil baseline. The islands are grains and the fluid interface in lower fracture is the boundary between oil (yellow/green) and water. Brine B (same concentration as the brine in matrix) was injected through lower fracture at a rate of 0.042 ml/h. No mobilization or movement of interfaces were observed within field of view during the baseline.The length-scale in the lower right corner of the images represent 500 μm. The area in red is the region where water droplets will coalescence and adhesion will be observed in subsequent LSW tests.

8.1.2 Crude oil baseline

A baseline was also created for Ekofisk crude oil. The crude oil was first run through a 40μm, and then a 15μm filter to remove particles that could potentially block pore throats and channels in the micromodel. The micromodel was saturated with Brine A as salinity concentration. Contrary to tests with refined oil, tests with crude did show a response to injection rate. It was observed that the crude in the lower fracture expanded as the rate was reduced down to the osmotic diffusion rate (0.042 ml/h). Another test was therefore run with step-wise reduction in injection rate. This was done to minimize the influence of the expanding oil phase on baseline results investigating potential diffusion transport. With this approach, no movement was observed through the crude oil in the fracture or matrix during the baseline test. The results are shown in Figure 8.2.
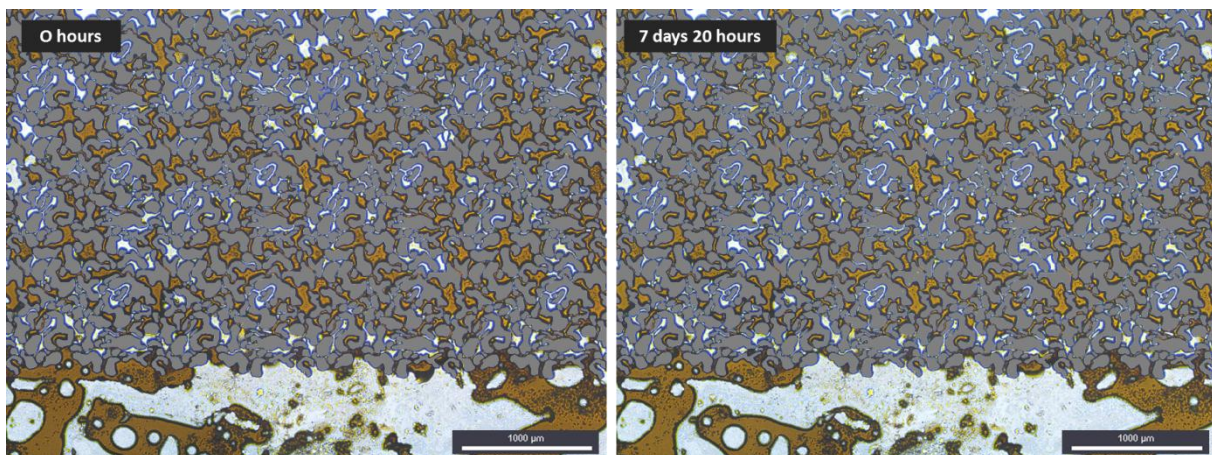
Figure 8.2 - Crude oil baseline. The brown phase is crude oil, the grey islands are grains, and the transparent phase is water. No mobilization or movement of interfaces were observed in field of view during the baseline test. The length-scale in the lower right corner of the images represent 1000 μm.

8.2 Water Dispersions and Droplet Growth in Matrix

8.2.1 Salinity gradient and osmotic diffusion

After conducting the refined oil baseline tests, LSW was performed by injecting low salinity water through lower fracture into the system initially saturated with high salinity Brine B (Table 5.1) and primary drained with n-Hexane. The low salinity waterflood established a high salinity gradient between the aqueous phases. Osmotic diffusion was allowed to progress and monitored through the microscope.
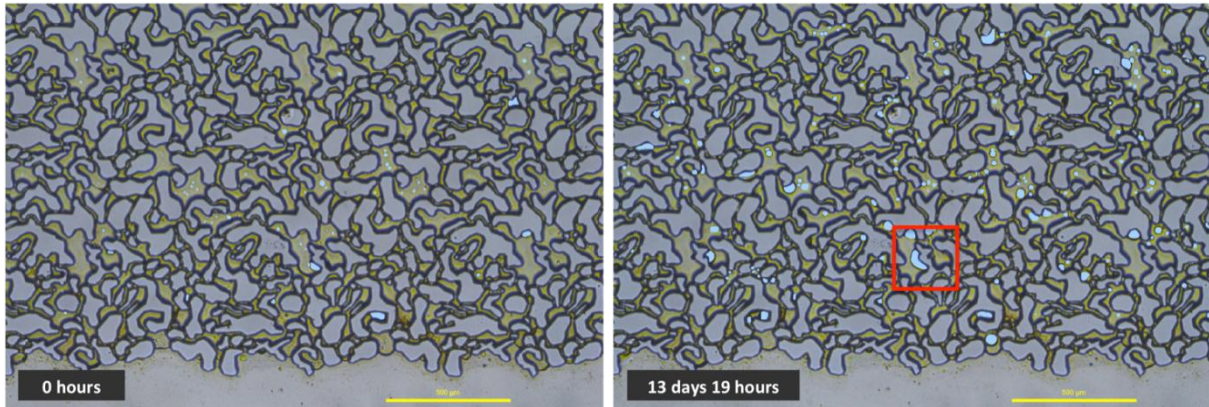

Figure 8.3 - Water dispersions and droplet growth. The blue areas are water dispersions and droplets, the grey islands are grains and the green/yellow phase is oil. With an osmotic gradient water droplets are mobilized through the semi-permeable oil into the matrix and grow along pore walls in surface roughness. The matrix distribution of water droplets before LSW (0 hours) and after (13 days 19 hours) are illustrated in blue. The area shows a region where continuous water droplet growth was observed. The length-scale in the lower right corner of the images represent 500 μm.

During the approximately 14 days of LSW, osmotic diffusion occurred through the semi-permeable oil membrane resulting in increased amounts of water dipersions within the oil phase across field of view. The results showed both water dispersion and droplet growth along the pore walls. Figure 8.3 shows the increased water dispersion and droplet growth from time 0 to 13 days and 19 hours.

The increased amount of water dispersions in matrix oil confirms that the continous oil layer works as a semi-permeable membrane transmitting water moelcules to high saline water-in-oil, validating the osmotic effect visualized throught the capillary tube experiments of Sandengen and Arntzen (2013).

In addition, as the porous media is strongly water-wet, low salinity water will flow along the pore walls of the matrix and reach inaccessible regions of high salinity brine through waterfilm diffusion. When encountering surface roughness the water phase will accumulate and droplet growth is observed. The water droplet growth will eventually displace the residual oil of the originating pore to more conductive areas in matrix.

8.2.2 Continuous water droplet growth

When carrying out LSW in the previous system, composed of Brine B and primary drained with n-Hexane, increased diffusion resulted in water dispersion -and water droplet growth. Osmotic activity was seen across the matrix field of view, and the continuous water droplet growth along pore walls

displaced on the surrounding oil phase. In addition, oil production was observed through the lower fracture from outside field of view.

Figure 8.4 shows an image sequence of a continuous water droplet growth within matrix. The location of field of view is indicated in Figure 8.3. In Figure 8.4 image I, 2 hours and 15 minutes after initiating low salinity injection, a water droplet A appears within the angled corner of the right pore wall inside the hightlighted oil phase. In Figure 8.4 the water droplet is colored blue and the sourrounding oil interface is highlighted in red. Water droplet A starts to grow as low salinity water diffuses through the intital high salinity brine coating the pore walls. The waterfilm expands and a water droplet forms. The droplet expands until it reaches a maximum size, image II-III (5 hours and 30 minutes), where the droplet snaps-off and returns as a waterfilm along the pore wall.

Figure 8.4 - Continuous water droplet growth. The blue color indicates the growing water droplet and the red highlights the oil phase. The dark blue lines are shadows and interfaces between oil and grains. Image I) Water droplet A appears at the grain surface. Image II-III) The water droplet grows and pushes on the surrounding oil phase until it reaches maximum size and snaps back into a waterfilm. Image IV) The water droplet reappears and starts to grow. Image V-VI) Water droplet grows to maximum size and displace the oil phase. Image VII-IX) The water droplet snaps back to a waterfilm, but grows back again to displace the surrounding oil phase into the interconnected pore channels. In addtion, two more water droplets have emerged as B and C, and water dispersions are evident in the adjacent pore encircled in green. The length-scale in the lower right corner of the images represents 100 µm.
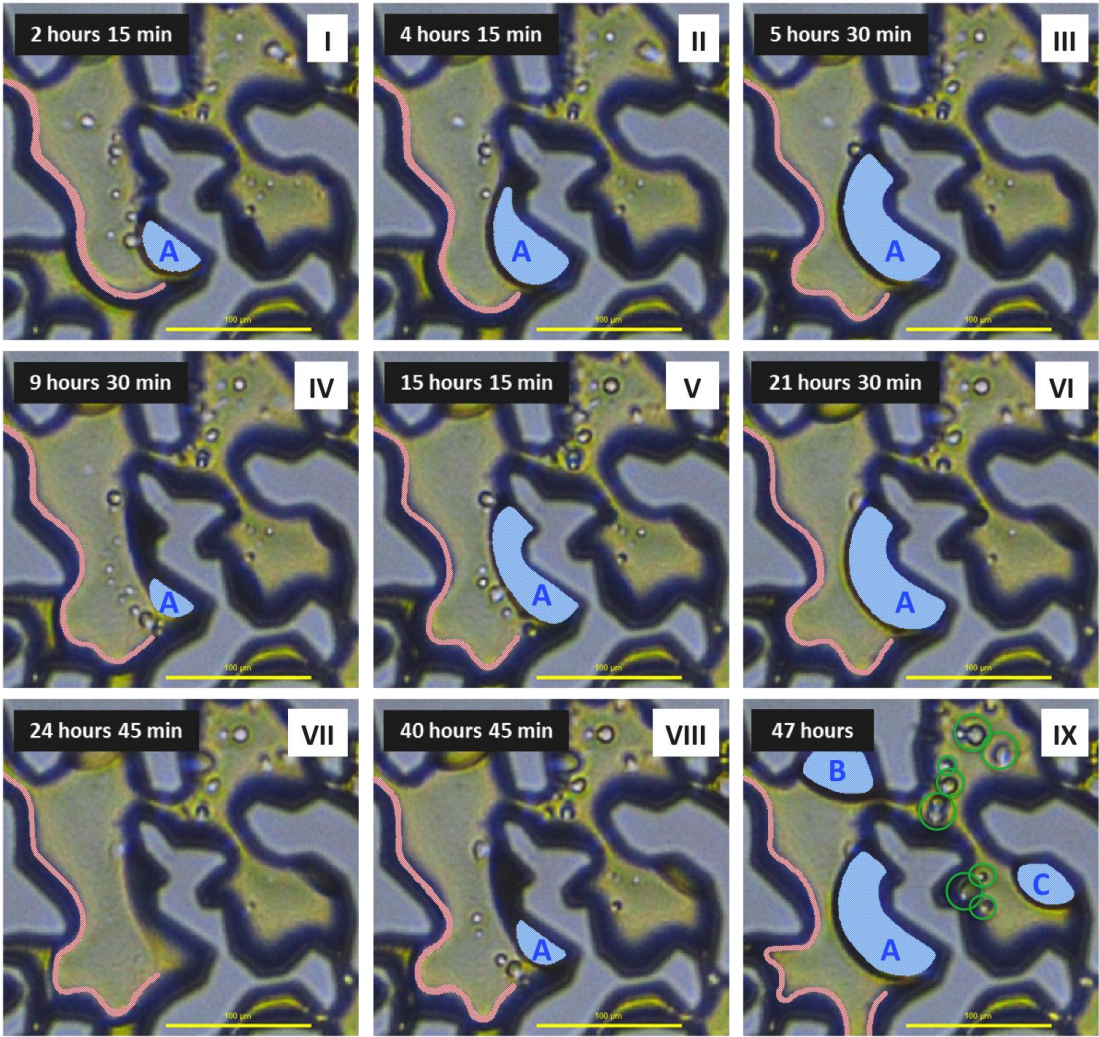
Repeatedly, after 9 hours and 30 min in image IV, the waterfilm starts to expand again pushing on the surrounding oil phase. After 21 hours and 30 min, image VI, the water droplet reaches its maximum size and snaps. The water droplet continues to grow and snaps-off 5 times during the osmotic process. After 47 hours, image IX, the water droplet has managed to displace the surrounding oil into the interconnected pore channels. In addition, a water droplet B has emerged along the near-by pore wall, and in the adjacent pore to the right, a water droplet C and several water dispersions have formed. The water dispersions are circled in green.

It is believed that the main mechanism for water droplet growth along the pore wall is water diffusion of low salinity water through the high salinity water film coating the grains. When water encounters areas with rougher surface it will accumulate until it exceeds the barrier and diffuse on. Hence, the water droplet will grow continously until it snaps-off. The direction of flow after snap-off is unknown due to the dark shadows along the grains. No direct change or movement is seen in the vicinity or in the adjacent pore.

Droplet size versus diffusion time was measured for the continuous growth of water droplet A. The size of the droplet was measured using the NIS-Elements D-Imaging Software importing the time-lapse images taken during the osmotic process. Figure 8.5 illustrates how the measurements were performed.
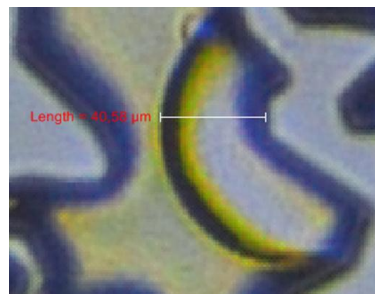
Figure 8.5 - Measurements of water droplet growth. The values were obtained by using the NIS-Elements D-Imaging Software and the length-scale function within the program. This function allowed the measurement of length from one fixed point. The fixed point was set at the grain surface, and the opposite end of the scale was moved according to the droplet size. The numerical value is shown next to the scale.

Figure 8.6 shows the growth of the expanding water droplet compared to diffusion time. During the time the experiment progressed, the water droplet grew to a maximum of 41.7 μm in five different sequences. The growth occurred continuously for the first 2.5 days, but as the diffusion process progressed the growth diminished. After approximately 5 days, water droplet growth was significantly reduced. During the next 8 days until the diffusion process was terminated the water droplet was unable to reach its maximum size.

Figure 8.6 - Water droplet size as a function of diffusion time. The blue graph represents water droplet growth and the repeated sequences during the length of osmotic diffusion. The red dots and the polynomial trend line represent the water droplet snap-off time to the duration of diffusion. The trend line increases exponentially and the water droplet will eventually be unable to reach maximum snap-off size due to the diminishing effect of the osmotic gradient.

A polynomial approximation was provided to relate the water droplet snap-off time to the duration of the diffusion process. The red dots on Figure 8.6 illustrate the time in days between each snap-off compared to diffusion time. The trend line shows a positive exponential curve. The increased exponential development indicates that the driving force for the water droplet growth decreases as the time span between each snap-off increases.

During the first two days, snap-off time occurred at high rates. However, during the last droplet growth, it took approximately 4 days before the droplet reached maximum size as the diffusion process and salinity gradient slowly declined by dilution (*cf.* Figure 8.6). The droplet growth eventually stopped as equilibrium between the aqueous phases was established

8.2.3 Water droplet coalescence and adhesion

To investigate the effect of water dispersion and droplet growth through an oil membrane of higher carbon number, the system was re-established with Brine B, but primary drained with refined oil n-Heptane before implementing LSW.

During the osmotic diffusion process water droplets started to grow within the largest pores of the network marked red in Figure 8.1. An image sequence documenting water dispersion and water droplet growth, coalescence and adhesion is shown in Figure 8.7. In image I pore A, taken after 8 hours and 30 minutes, water dispersions have emerged in the oil bulk due to osmotic diffusion of low salinity water into high salinity water-in-oil. Water droplets have also occurred on pore walls due to water diffusion. In images II-IV the water dispersions continue to grow and coalesce into larger accumulations. Image IV represents status after 35 hours.

Figure 8.7 - Water droplet coalescence and adhesion. The dark blue lines are shadows and interfaces between water and oil. The grains are within the sharp-edged side of the blue lines. Image I-IV) Water dispersions coalesce in the large oil pore A, and water droplets grows along the pore wall. Image V) Due to differences in fluid density the water dispersions descend and adhere to the wate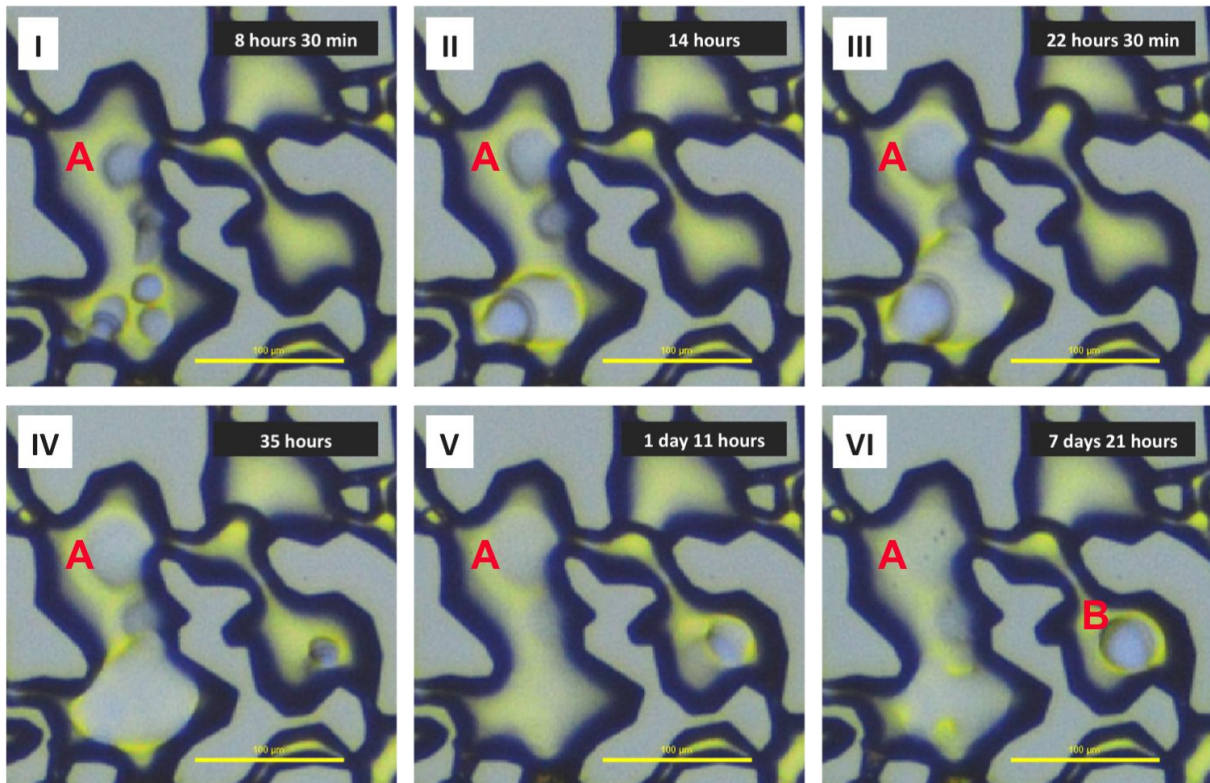r-wet glass observation window. VI) Water adheres to the glass window and in the near-by pore B to the right a water-core has continuously grown towards the water-wet glass surface. The length-scale in the lower right corner of the images represent 100 µm.

Due to density differences, the larger accumulations of water dispersions descend within the oil phase and relocate underneath the oil bulk as seen in image V. As the dispersions relocate within the porous media, the strongly water-wet nature of the glass observation window causes the water to adhere to and spread across the surface. This effect is clearly shown in image VI after 7 days and 21 hours. In the neighbouring pore B to the right, water-in-oil can be seen continuously growing towards the water-wet surface of the window, image IV-VI. The diffusion mechanism transporting low saline water into the brine concentrated water-in-oil could clarily be that of osmosis.

When increasing the carbon number of the oil by using n-Heptane, the viscosity of the oil membrane will increase. From the observed diffusion process, water dispersion and water droplet growth was reduced through the oil phase compared to the n-Hexane membrane. From the Stokes-Einstein equation (*cf.* equation 3.2), the diffusion constant of low saline water is inversely proportional to viscosity which should reduce the waterflux through higher viscosity membranes as seen across the field of view.

8.3 Residual Oil Displacement and Mobilization in Matrix and Fracture

8.3.1 Movement of interfaces in matrix

After studying the effect of changing the composition of the refined oil membrane, it was decided to alter the concentration of the initial high salinity brine to one with lower salt content. To study the effect of brine salinity on osmotic diffusion the system initially saturated with Brine B was changed to Brine A (5wt% NaCl) (*cf.* Table 5.1).

The porous media was primary drained using the refined oil compositions previously applied. Figure 8.8 shows the results of osmotic diffusion in a matrix primary drained by n-Heptane and initially saturated with Brine A. After 6 days and 21 hours, oil displacement and movement of interfaces were observed within matrix. The shift can be seen by the relocations of the oil phase encircled green in the figure. Water dispersions were not detected, and only some areas were found with water droplet growth. No mobilization of oil to fracture or production was observed.
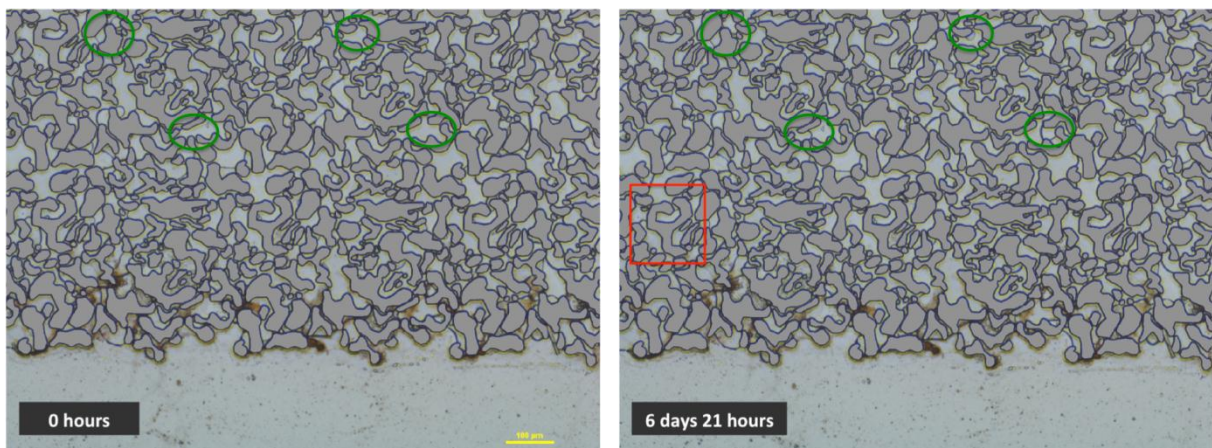
Figure 8.8 - Oil movement and redistribution of interfaces. The grey islands are grains and the dark lines between the grains are interfaces between water and oil. After 6 days and 21 hours, a shift and relocation of the oil phase can be seen in the green encircled areas. The area highlighted in red indicates a region where oil displacement occurred (See Figure 8.9 for details). The length-scale in the lower right corner of the image represent 100 μm.

8.3.2 Inaccessible water expansion and oil displacement in matrix

From the system established in section 8.3.1, where a lower salinity gradient is applied through a high carbon numbered oil (*i.e.* n-Heptane), an oil displacement process in matrix is documented in Figure 8.9. Initially, inaccessible high salinity brine resides within a cul-de-sac "dead-end" pore in image I. The blue color represents the aqueous phases (brine and low salinity water) while the red represent the oil phase. Residual oil droplets are also located inside the inaccessible pore.

Figure 8.9 - Inaccessible water expansion and oil displacement in matrix. Blue color indicates the aqueous phases and red indicates the oil phase. The dark blue lines are shadows and interfaces between water, oil and grains. Image I) Cul-de-sac pore with inaccessible brine and residual oil droplets are observed. Image II) Oil phase B is displaced through matrix from events outside field of view into the cul-de-sac pore. Image III) Brine A inside the pore is displaced by film flow to water phase C. The advancement of oil B stops due to capill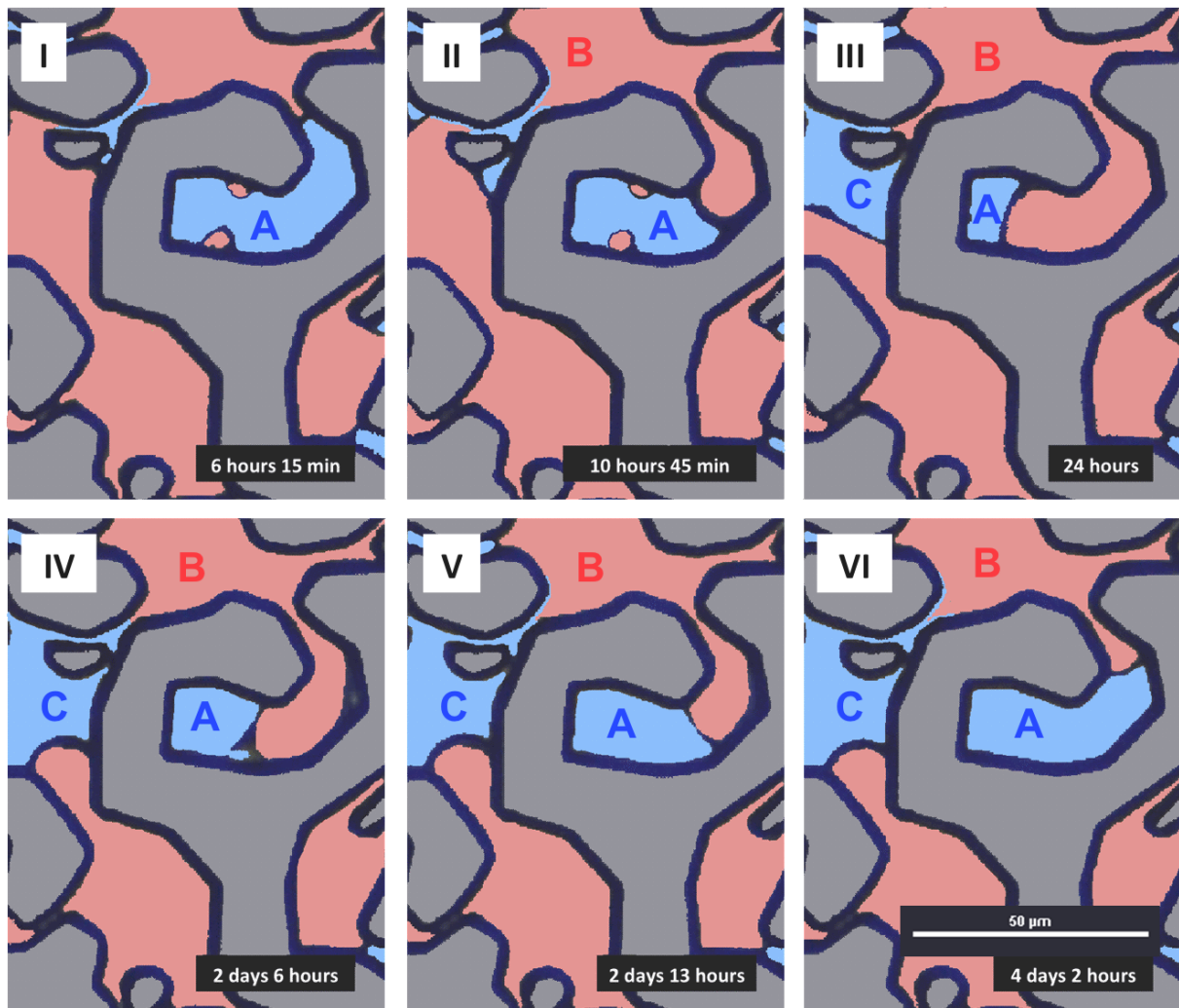ary forces inside the pore. Image IV-V) Low salinity diffusion increases water saturation C (from outside field of view), and forces water back into the inaccessible brine A through film flow. The growth in A leads to relocation of oil phase B. Image VI) The displacement process cease when high salinity brine A is diluted by the low saline water from C.

After 10 hours and 45 minutes, image II, oil phase B is displaced from matrix outside field of view into the cul-de-sac pore. As oil phase B is enforced into the pore, initial high salinity brine A is displaced into the pore channel through film flow. In image III, the oil phase B has reached the residual oil droplets within the pore, but further advancement is stopped due to capillary pressure. Outside the pore, water saturation C stops swelling as film flow from A ceases.

In image IV, after 2 days and 6 hours of low salinity water injection, water phase C starts to grow. The expansion is a result of water diffusion between low salinity water and brine outside field of view. In image V (after another 7 hours) water from C travels back into the inaccessible pore A through film flow. The high salinity brine A expands relocating oil phase B. The displacement process continues until low saline phase C has fully diluted the brine concentration inside A. The oil displacement

process ends after 4 days and 2 hours, image VI, and the saturation distribution remains stagnant until the diffusion process is terminated after a total of 6 days and 21 hours.

The main transport mechanism leading to oil displacement was diffusion of low salinity water through the high salinity water-film coating the matrix grains. The dilution of high salinity water in the matrix causes the water phase to expand and the oil phase to displace as observed in Figure 8.9. Extensive water dispersion due to osmotic diffusion was not apparent through the oil phase in this low salinity gradient system, but occational water droplet growth along pore walls was observed due to water diffusion film flow.

8.3.3   Oil displacement and mobilization to fracture

Another experiment was performed changing the oil composition to n-Hexane creating a lower viscosity oil membrane. The brine concentration was kept at 5wt% NaCl, i.e. low salinity gradient, and low salinity water was injected. During LSW, both water dispersion and droplet growth was observed several places within the matrix. High salinity brine expansion by diffusion of low salinity water through film flow caused oil displacement and oil mobilization from matrix to fracture. In addition, oil was produced from fracture on two occasions within the field of view.
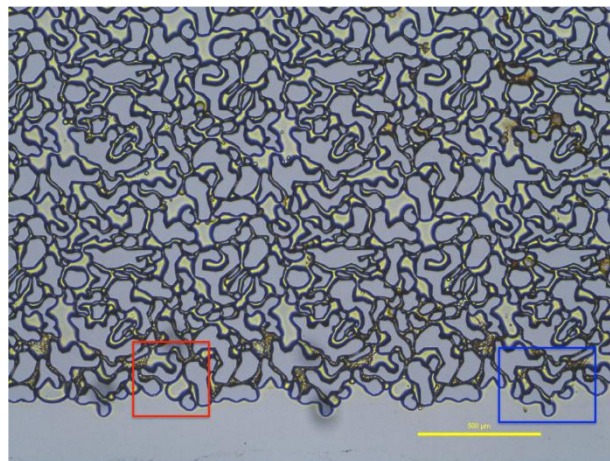
Figure 8.10 - Field of view indicating the areas of observed matrix - fracture interactions. Grains are coloured grey, and the dark lines between the grains are shadows or interfaces between water and oil (green/yellow phase). The red and blue boxes indicate the regions where oil displacement and oil mobilization were observed respectively. The length-scale in the lower right corner of the image represents 500 µm.

Figure 8.10 shows the field of view and outlines two regions of interest (red and blue) where oil displacement and mobilization to fracture was observed. The oil displacement to fracture within the red region is explained in more detail in the following section, introducing the mobilization process of oil to fracture and subsequent oil production in section 8.3.5.

8.3.4   Oil displacement to fracture

Figure 8.11 documents the process of oil displacement to fracture from two pore channels in connection to matrix oil (*cf.* field of view indicated in Figure 8.10). Image I shows the initial conditions when displacement was observed after 4 days and 20 hours of LSW. Phase A is the low salinity water in fracture, and phase B is inaccessible high salinity brine in a dead-end pore. Phase C is the displacing oil droplet. In image II, low salinity water A diffuses by film flow into the inaccessible brine phase B. The brine expands and displaces oil droplet C towards the fracture.
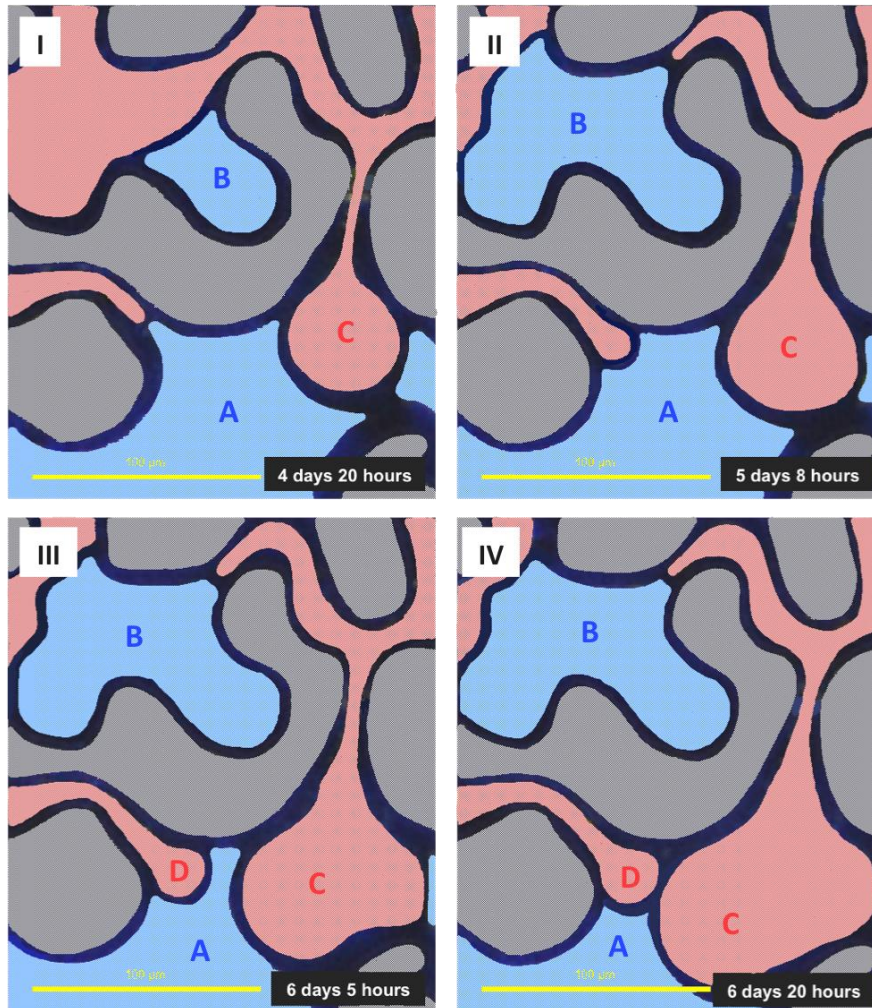
Figure 8.11 - Oil displacement to fracture. Blue colour indicates the aqueous phases and red indicates the oil phase. The dark blue lines are shadows and interfaces between water, oil and grains. Image I) An oil droplet C occurs through a pore throat. Inaccessible brine B is located within a "dead-end" pore and low saline water A fills the fracture. Image II) Low saline water A diffuses from fracture into the high saline water B. Water phase B expands and displaces the surrounding oil e.g. droplet C towards the fracture. Image III) Oil C moves towards fracture by displacement from upper matrix, and an oil droplet D is displaced into the same pore channel from the adjacent pore throat. Image IV) Location of oil droplets C and D as LSW is terminated. The length -scale in the lower left corner of the image represent 100 µm.

As oil droplet C is in contact with matrix oil outside field of view, the oil is further displaced towards fracture by an above displacement process. In addtion, an oil droplet D is also displaced into the same pore channel from an adjacent pore throat. The displacement of the two oil droplets C and D continues until the diffusion process is terminated after 6 days and 20 hours. At this time , image IV, the two oil droplets are in close contact, and further diffusion could have caused the dropelts to mix and mobilize into the lower fracture. This process of oil displacement indicates that water diffusion transport may provide enough driving force to produce oil to fracture in the presence of a low salinity gradient.

66

8.3.5 Oil mobilization to fracture

Oil mobilization from matrix to lower fracture was observed several times during the LSW scenario with Brine A (5wt% NaCl) by water diffusion transport. Two of the mobilization processes occurred within field of view originating from the same pore throat, blue region in Figure 8.10. The first oil mobilisation occurred after 21 hours and 15 minutes of low salinity injection. Figure 8.12 documents the process. Mobilization was not observed during the first 21 hours and 15 min, image I. After additional 15 min as shown in image II, an oil droplet A emerged from a pore throat in direct contact with the fracture. After 57 hours, image III-IV, the oil droplet continues to grow from the pore throat. In addition, a second oil droplet B in proximity to A has appeared on the outside of the grain. In the next image V, mobilized oil from a region outside the field of view fills the fracture flowing towards the production port. The oil phase in fracture adheres to the matrix-fracture boundary, and oil droplet A mixes with the oil phase and is produced with the bulk flow, image VI. Oil droplet B was not produced, as the bypassing oil was not in direct contact with the droplet.
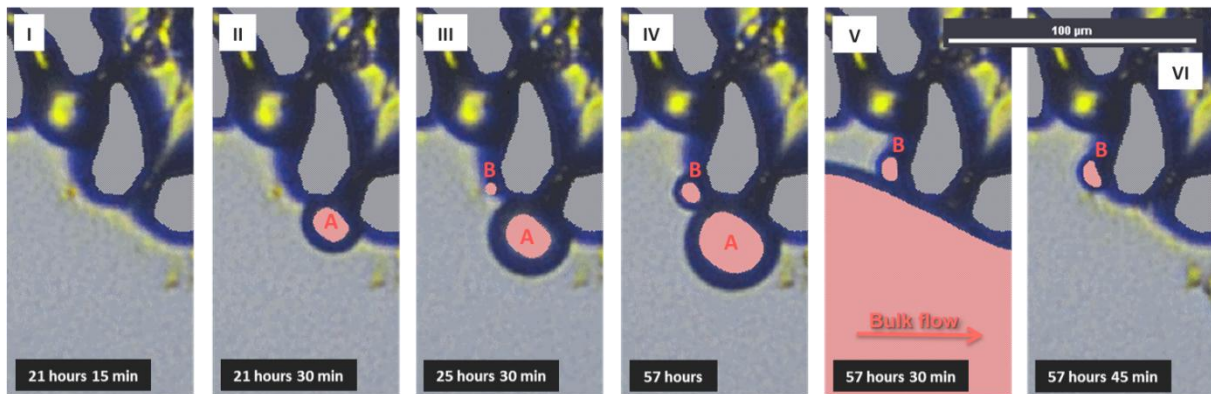
Figure 8.12 - Oil mobilization from matrix and fracture production. Red color represents the oil phase, the grey islands are grains. The dark blue lines are shadows and interfaces between water, oil and grains. Image I) The initial situation before oil mobilization. Image II) An oil droplet A emerges from the pore throat. Image III-IV) Oil droplet A continues to grow from pore throat to fracture. In addition, an oil droplet B emerges in vicinity of A. Image V) Oil phase produced from outside field of view bypasses the observed area. The red arrow indicates flow direction. The oil phase adheres to the matrix-fracture boundary. Image VI) Oil droplet A is produced together with the bypassing bulk. Droplet B is not mobilized as it was not in direct contact with the passing oil.

A second mobilization process occurred after 99 hours and 15 min shown in Figure 8.13. In image I, oil droplet B is located as left after the first mobilization. In addtion, two more oil droplets C and D are defined on opposite side of the grains. After 96 hours, and prior to the second mobilization of oil droplet A, a flow of mobilized oil passes the field of view, image II. The bypassing oil adheres to the matrix, image III, and oil droplet C is produced, image IV. An immobile oil droplet E is left behind in facture and increased oil saturation at D is observed. After 99 hours and 15 min, image V, an oil droplet A reemerges.

Oil droplet A grows over the next time span, image V- VI, before it is produced together with a bulk of mobilized oil after 118 hours, image VII. The bulk of mobilized oil produces in addition droplets C, D and E , but droplet B remains in place.
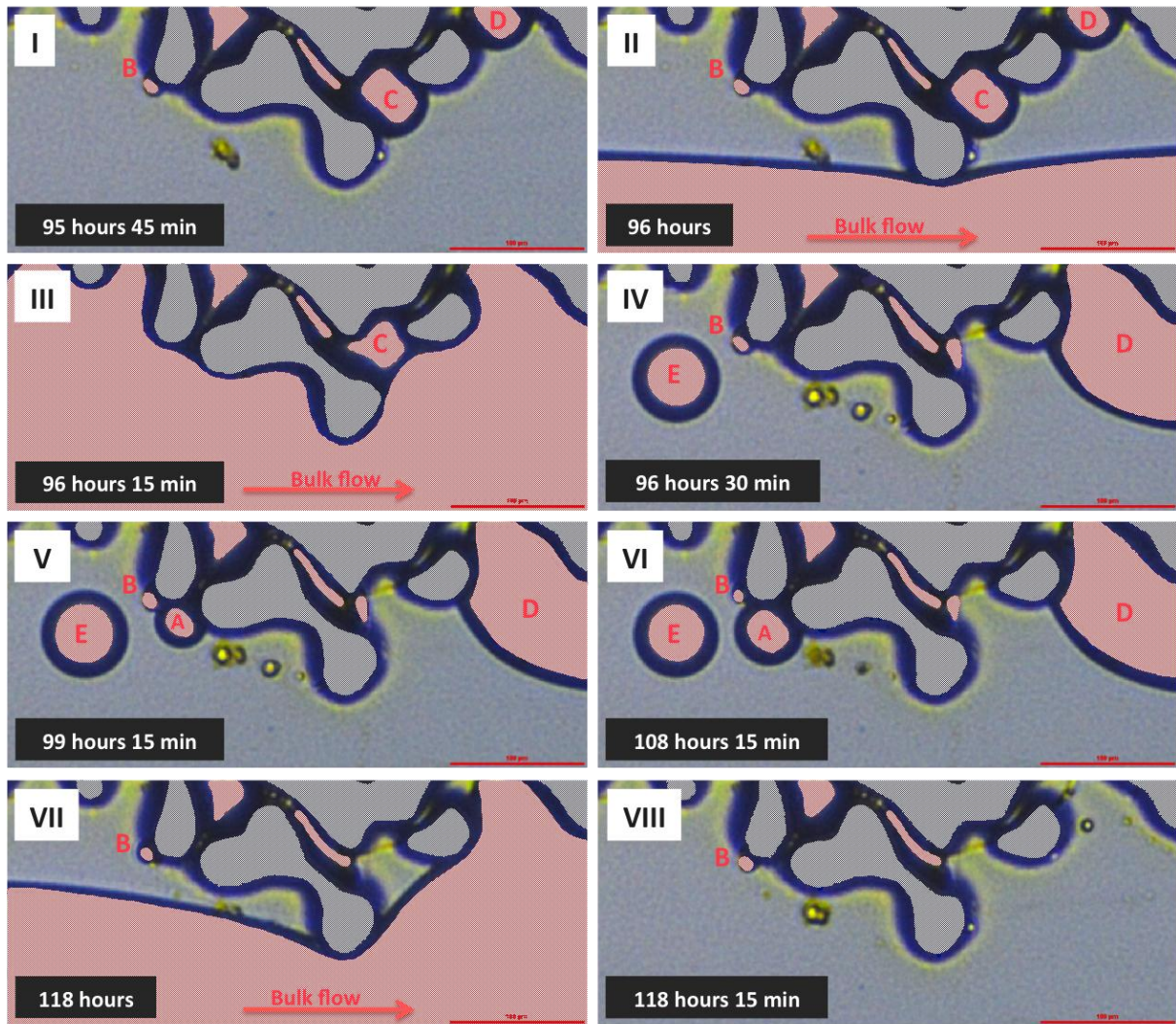
Figure 8.13 - Repeated oil mobilization from matrix. Red color represents the oil phase. The dark blue lines are shadows and interfaces between water, oil and grains. Image I) Indicates the initial situation and localization of oil droplets B, C and D. Image II) A stream of mobilized oil from outside field of view enters the region. Image III) The mobilized oil adheres to the matrix-fracture boundary. Image IV) The bypassed oil bulk has produced with it oil droplet C, but has left behind oil droplet E and oil saturation at D. Image V-VI) An oil droplet A emerges from the pore throat and grows into the fracture. VII) Another stream of mobilized oil passes the observed area. VIII) All oil droplets A, C, D and E are produced. Oil droplet B remains in place. The length-scale in the lower right corner of the image represent 100 µm.

The counter-current oil production from matrix to fracture illustrated in figure 8.12 and 8.13 is important in enhanced oil production from heterogeneous fractured reservoirs. During LSW, the water will channel through the fracture system but due to the salinity gradient, water will diffuse into matrix especially in mixed-wet carbonate reservoirs where spontaneous imbibtion is reduced. The high salinity brine will expand and displace movable oil through the matrix. The oil will be mobilized into fracture through paths of least resistance, as observed in the above image sequences where the droplet appears from the same pore throat twice. As larger bulks of oil are produced along the matrix-fracture boundary mobilized droplets will mix with the growing oil phase and flow with the current.

8.4 Crude Oil Displacement and Water Dispersion Growth

8.4.1 Crude oil displacement in matrix

After completing the frist set of experiments documenting the influence of different brine salinities and refined oil compositions on osmotic diffusion, it was decided to investigate the influence of an Ekofisk crude oil membrane. Because viscosity of crude oil is larger than that of water, the effect of osmosis at room temperature was assumed to be minor. The crude was filtered through a 40µm and 15µm filter to sieve out larger particles, and two different scenarios were considered. The first was to establish a continuous crude oil membrane through the matrix as in the refined oil experiments. The second was to create a residual oil system. The initial high salinity brine concentration was 5wt% NaCl for all crude oil tests. This was based on the refined oil experiments since the majority of water dispersion, droplet growth, oil displacement and mobilization had occurred at that salinity.

A continuous Ekofisk crude oil membrane was established through the matrix as illustrated by the brown oil phase in Figure 8.14. In this system, low salinity water (Brine C) was injected into the lower fracture after completing the second baseline test. As a result, osmotic diffusion of low saline water induced displacement of oil within the matrix, and crude oil was mobilized into the channel at several occasions. The red, blue and green areas will be described in detail below.
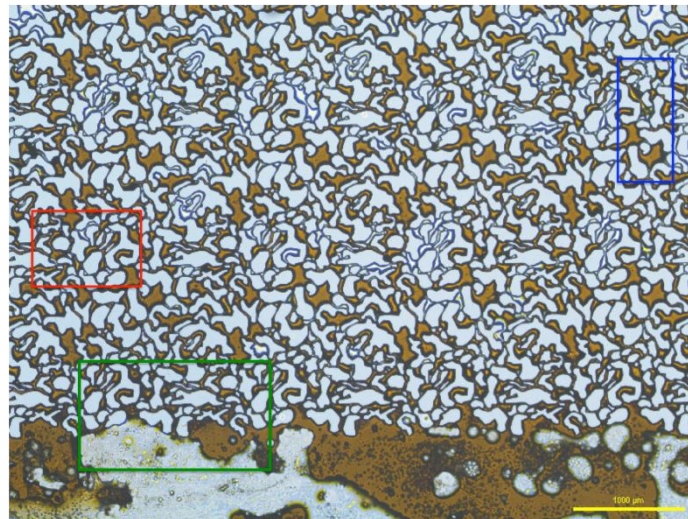
Figure 8.14 - Continuous crude oil membrane within field of view. The brown phase is crude oil, the grey islands are grains, and the transparent phase is water saturation. The red, blue and green regions of interest indicate the areas where oil displacement was observed during osmotic diffusion. The length-scale in the lower right corner of the image represent 1000 µm.

The displacement process within the red region is illustrated in Figure 8.15 below. After 2 days and 10 hours the oil and brine distribution was as illustrated in image I. As low salinity water diffuses into matrix it reaches pore A, image II, and the intitial crude oil is displaced. The low salinity water diffuses by film flow further into pore B containing intital brine. The high salinity brine in pore B expands and displaces oil from the interconnected pore C, image II. In image III, the water further invades the surrounding pore channels D, E and F from pore C. An equal displacement process has also occurred at G, image III.

Figure 8.15 - Crude oil displacement by low salinity diffusion in matrix. The brown phase is crude oil, the grey areas are grains, and the transparent phase is water saturation. The dark blue lines are shadows and interfaces between water, oil and grains. Blue arrows indicate water flow. Image I) Intital fluid distribution in the observed area after 2 days and 19 hours of osmotic diffusion. Image II) Low salinity water diffuses from pore A by film flow into pore B. The high salinity brine in pore B expands and displaces oil from the interconnected pore C. Image III) Water phase continues to displace oil from the surrounding pore channels D, E and F. The same displacement process is observed in pore G.

The second oil displacement was observed in the region of interest indicated in blue in Figure 8.14. The process is described in Figure 8.16. In image I, pore A and B is filled with brine and pore C is filled with crude oil. During the next hour, image II, a shift and re-location of phases occur as oil is suddenly produced from lower matrix into fracture (*cf.* Figure 8.18). Pore C is now filled with water, image II. The initial oil was displaced down towards fracture during the re-relocation of fluids. Simultaneously, in pore A and B, crude oil is displaced from the upper part of matrix refilling the pores.

There is a contact between pore B and C through pore D containing crude oil, image III. As crude oil refills pore B, the inititial brine pushes on the oil phase in pore D. As a result crude oil is displaced into pore C. After 6 days and 3 hours, image IV, crude oil has refilled most of the pore space in C. The displacement of crude oil from the upper part of matrix into pore A and B has ceased.
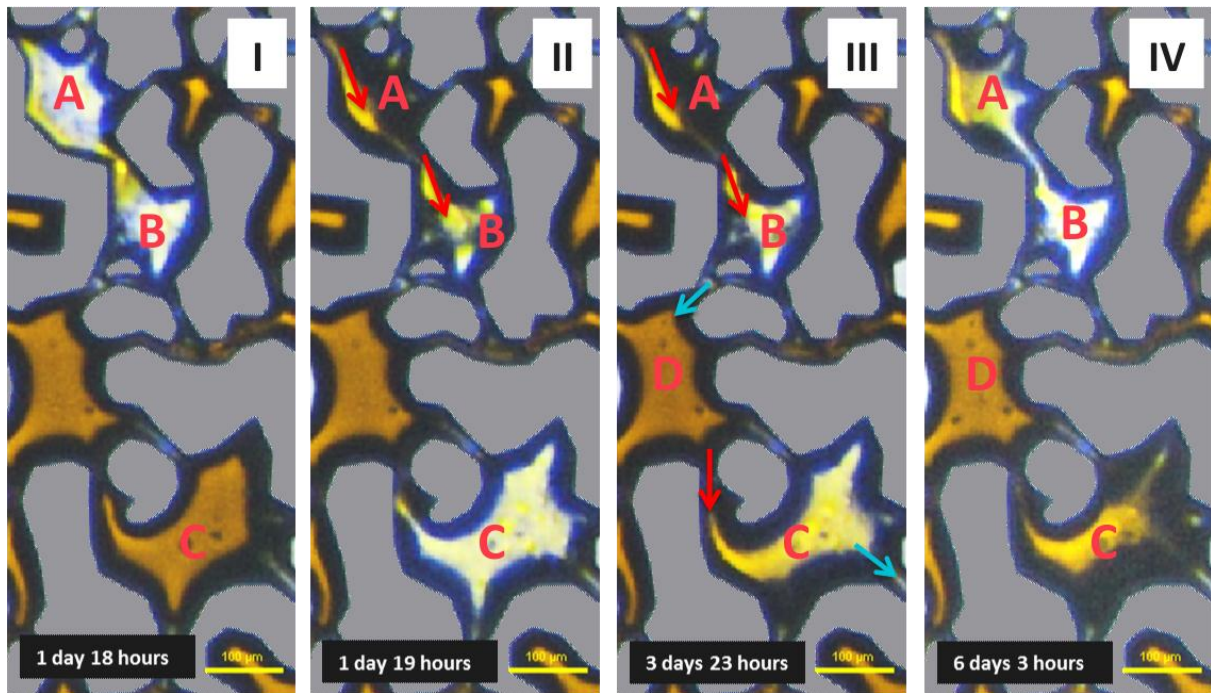
Figure 8.16 - Redistribution of fluids and crude oil displacement in matrix. The brown phase is crude oil, the grey islands are grains and the transparent phase is water. The dark blue lines are shadows and interfaces between water, oil and grains. The red arrows indicate oil flow and the blue arrows indicate water flow. Image I) Initial saturation as observed after 1 day and 18 hours of osmotic diffusion. Pore A and B contains high salinity brine, and pore C contains crude oil. Image II) Oil produced into lower fracture causes the fluids to redistribute within matrix. Pore A and B are drained by crude oil from upper part of matrix and the crude oil in pore C is displaced by water. Image III) As pore B fills with oil the initial brine phase pushes on the oil saturation in pore D. Crude oil is drained from pore D into pore C and water is displaced out of field of view. Image VI) After 6 days and 3 hours the drainage of oil to pore A and B has ceased, and pore C is partially refilled with crude.

In Figure 8.17, 7 days and 4 hours after start of injection, pore C from Figure 8.16 is again completely filled with crude oil, image I. During the next 7 hours, image II-IV, the crude oil within the pore is gradually displaced by low salinity diffusion. In image II, the water film along the pore wall starts to expand as low saline water diffuses through pore throath A from outside field of view. After 6 hours, image III, the water phase starts to displace the resident crude oil down pore channel B. In image IV, low salinity water has emptied the entire pore.

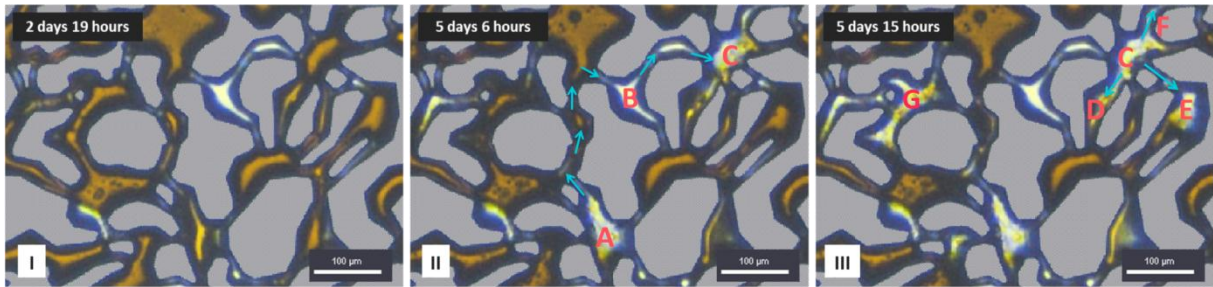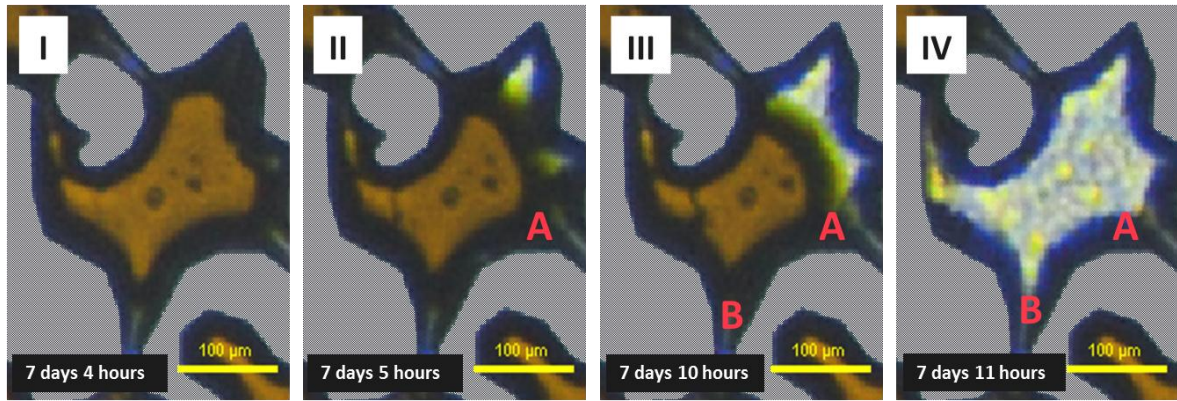*Figure 8.17 - Crude oil displacement by water film diffusion. The brown phase is crude oil, the grey islands are grains, and the transparent phase is water saturation. The dark blue lines are shadows and interfaces between water, oil and grains. Image I) Pore in matrix filled with crude oil. Image II) Low salinity water diffuses through pore channel A by film flow. Image III) Expanding water film displaces oil through pore channel B towards fracture. Image IV) Water phase has displaced all the crude from the pore.*

In addition to oil displacement within the matrix, crude oil was mobilized to fracture during the diffusion process. As crude oil is suddenly produced from the matrix, a shift occurs and the subsequent relocation of fluids takes place as described in Figure 8.16. Figure 8.18 illustrates the following process of crude oil production to fracture. The apparent region is illustrated green in Figure 8.14.
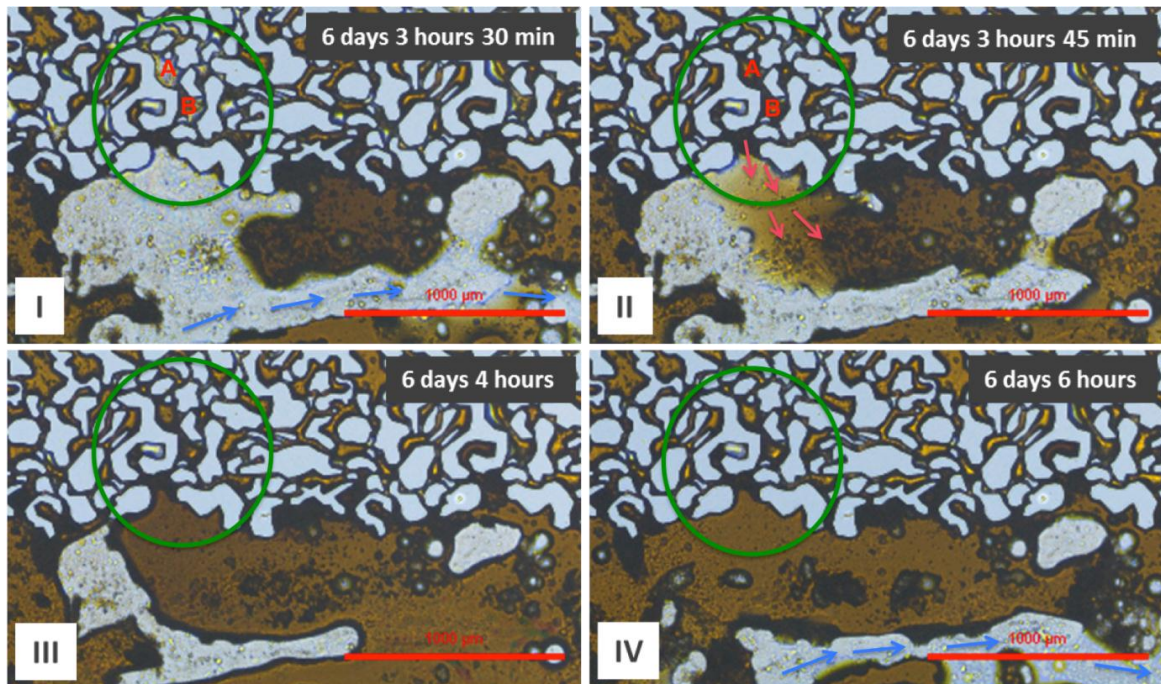
Figure 8.18 – Crude oil production. The brown phase is crude oil, the grey islands are grains, and the transparent phase is water saturation. Image I) Water-paths channel through crude oil in the fracture as indicated by the blue arrows. A region is circled in green where low salinity water from the fracture is in contact with matrix pores A and B. Image II) Oil is mobilized from the matrix through pores A and B into the fracture mixing with the crude already present. III) Crude oil from the matrix and fracture merge together forming a continuous phase. IV) Low salinity water starts to channel through the crude located along the matrix-fracture boundary towards production.

After 6 days 3 hours and 30 min, image I, low salinity water flows through the fracture in water-paths through the oil phase as indicated by the blue arrows. Inside the green circle, low salinity water from the fracture is in direct contact with the matrix and a continous water path connects with pore A and B. After 15 min, image II, pore A and B fills with oil and crude is mobilized into the fracture. In the fracture oil mixes with crude already present, and after another 15 min, image III, crude oil from the matrix has merged with oil in the fracture forming a coherent phase. More oil is produced into the fracture and after 6 days and 6 hours, image IV, a continuous oil phase is established along the matrix-fracture boundary. Low salinity water may again find its way through the oil and create water-paths towards production.

Oil displacement and mobilization take place within the continuous crude oil system in a high viscosity oil membrane. Water diffusion through film flow is the main transport mechanisms in the system as water dispersion and droplet growth are not observed. Water in the lower fracture is channells through the oil phase because of higher mobility. The oil remains immobile, but expands continuously as crude is displaced from the matrix.

8.4.2 Crude oil water-dispersion growth

To investigate the effect of LSW and osmosis in a system of residual oil saturation, a micromodel was prepared as in the previous crude oil experiment with Brine A. However, instead of creating a continuous oil membrane the process of secondary high salinity waterflooding was performed to establish residual oil saturation. Fluid distribution after the secondary waterflooding is shown in Figure 8.19. By creating a system of residual oil, the diffusion transport mechanism of low salinity water will first be dominated by water diffusion to dilute the initial high saliniy brine in matrix. Afterwards, the main mechanism will be osmotic diffusion mobilizing the residual oil saturations by water flux through the oil membrane. However, based on the experience with water flux through high viscosity refined oil membranes, the osmotic effect is expected to be reduced.

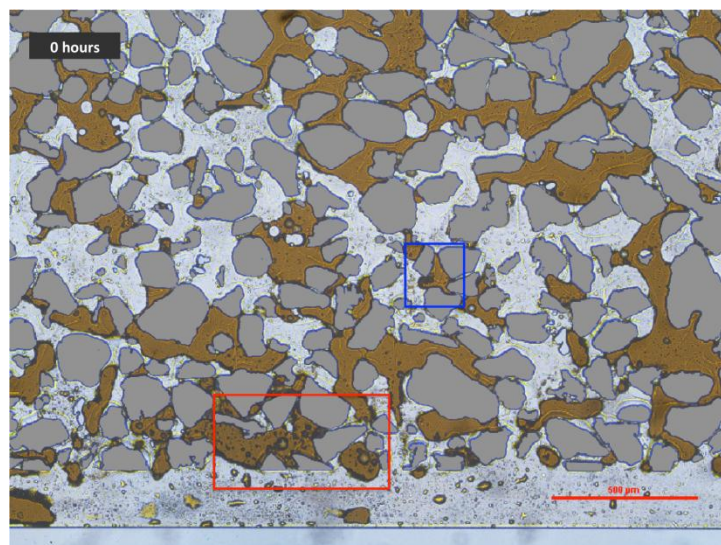*Figure 8.19 - Residual oil distribution after secondary waterflooding. The brown phase is crude oil, grey islands are grains, and the transparent phase is water saturation. The red box indicates the area where accumulations of water dispersions were observed. The blue box indicates the area where oil displacement developed. The length-scale in the lower right corner of the image represent 500 µm.*

Following preparations, low salinity waterflooding was performed. The results are illustrated in Figure 8.20. The area observed lies on the matrix-fracture boundary marked red in Figure 8.19. The initial conditions at 0 hours is depicted in image I. Traces of high salinity brine are located within the residual oil phase as water-in-oil. After 11 hours and 45 minutes, image II, increased amounts of water dispersions have occurred within the crude oil. The same effect as observed in Figure 8.4 is detected. As the water-in-oil coalesce into larger water dispersions, the density difference between the crude oil and water relocates the droplets down towards the water-wet glass surface of the micromodel. When the droplets reach the glass the water spreads out and adheres to the surface. An example of this behavior is observed by the two droplets encircled red in image II. During the course of LSW the two water-in-oil coalesce and subsequently disappear due to surface adhesion.

Figure 8.20 - Crude oil water-dispersion growth. The brown phase is crude oil, the grey islands are grains, and the transparent phase is water saturation. Image I) Initial conditions with water-in-oil observed within the crude. Image II) Water micro-dispersions have started to grow within the crude. The droplets encircled in red will coalesce and disappear by the next frame. Image III) Extensive water dispersion growth has caused the crude oil to expand towards the fracture. The length-scale in the lower part of the image represent 100 μm.

After 5 days, image III, the accumulations of water dispersions have grown extensively within the crude oil by osmotic diffusion. The initial water-in-oil expands as low salinity water diffuses through the oil membrane. The water-in-oil merge and form larger water disperisions. The increased water phase within the crude causes the oil phase to expand, moving the crude oil-water interface towards the fracture.

8.4.3 Crude oil displacement by water dispersions

Expansion of residual crude oil is also apparent within matrix due to osmotic transport of low salinity water through an oil membrane as illustrated in Figure 8.21. The residual oil saturation in question is located within a pore connected by four pore throats surrounded by high saline brine, blue region in Figure 8.19.

In Figure 8.21 image I, water-in-oil is observed within the oil phase near pore throat A. After 1 day and 3 hours, image II, possible osmotic diffusion of low saline water into the initial water-in-oil form water dispersions within the crude and the oil phase expands towards the left adjacent pore by throat A. The supply and diffusion of water into the crude oil is observed through pore throat B. By image III, the pore is almost filled by growing water dispersions, and at image VI, almost 50 % of the oil surface area is displaced into the neighbouring pore.
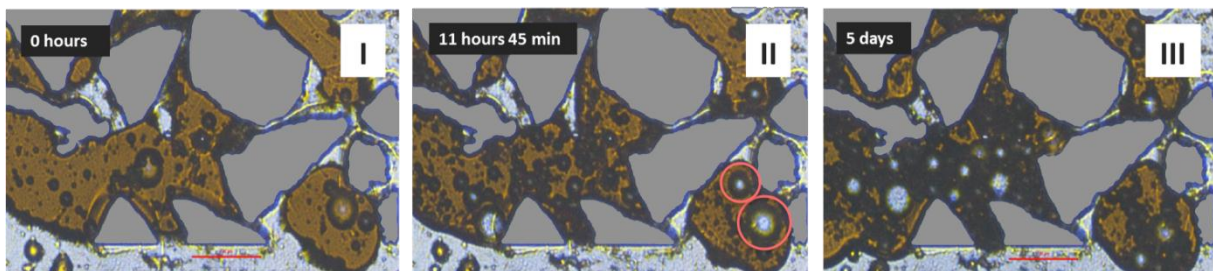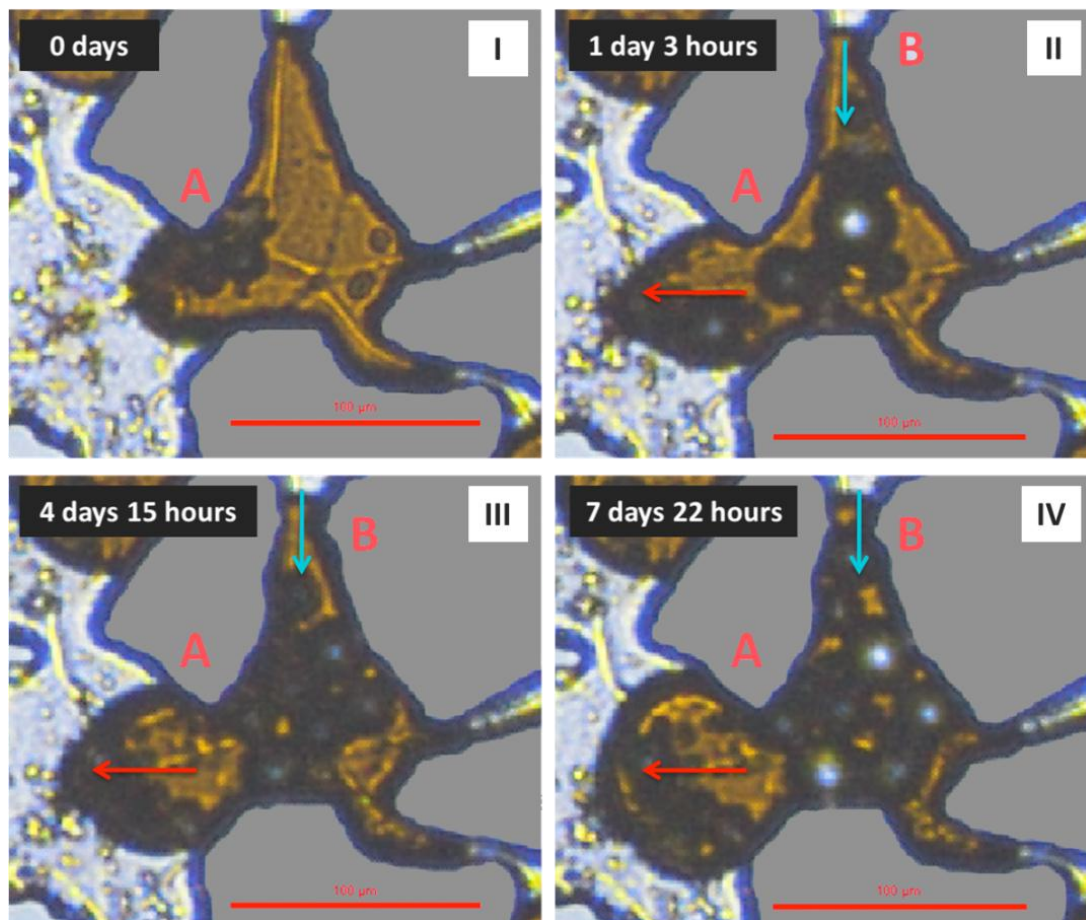
Figure 8.21 - Crude oil displacement by water dispersion growth. The brown phase is crude oil, the grey islands are grains, and the transparent phase is water saturation. Image I) Water cores are observed within the crude oil phase at pore throat A. Image II) Water dispersions grow within the crude supplied by low saline water through pore throat B. The oil phase starts to expand. Image III) Continuous water dispersion growth occurs within the oil phase. Image IV) A greater part of the oil phase is almost displaced into the adjacent pore through A. The length-scale in the lower part of the image represent 100 μm.

After creating a crude oil membrane in the matrix, continuous or residual, mobilization of oil is detected. The difference in the effective transport mechanisms between scenarios seems to be related to the magnitude of the oil membrane. In a continuous crude oil system, the high salinity brine is mainly distributed along the water-wet grains of the matrix, and water diffusion by film flow is a major mechanism. This is a slow process as illustrated in Figure 8.15. In a residual oil system, larger surfaces are covered with brine and direct dilution takes place when low salinity water is injected. As the water saturation in matrix reaches equilibrium, the remaining high salinity brine resides within the crude phase as water-in-oil. Osmosis becomes the main transport mechanisms, and increased water dispersion is observed.

8.5 Observed Mechanisms during Osmotic Diffusion

When implementing a salinity gradient in a system primary drained with oil, effects resembling osmotic diffusion were observed. From the baseline experiments provided for both refined oil and crude oil experiments, no fluid interactions were detected in the absence of an apparent salinity gradient (*cf.* Figure 8.1 and 8.2).

The first set of experiments was performed using refined oils n-Heptane and n-Hexane to investigate the effect of osmosis when applying a salinity contrast between the aqueous phases. According to Sandengen and Arntzen (2013), oil exhibits the characteristic properties of a semi-permeable membrane transporting non-polar water molecules, no ions, through the oil phase.

As the baseline tests showed no sign of fluid-fluid interactions or oil mobilization, it was assumed that the potential osmotic effect would be one of the primary mechanisms present during a tertiary waterflood of reduced salinity concentration. In the micromodel, the generally accepted LSE by wettability alteration is not applicable to the strongly water-wet system as oil droplets will not adhere to or spread across the surface of the water-wet grains. The proposed effects of fines migration, MIE or electrical double layer expansion by Tang and Morrow (1999), Lager *et al.* (2006) and Lightelm *et al.* (2009) are not evident as they rely on mixed-wet to oil-wet conditions for favourable oil mobilization and recovery.

When implementing LSW to a refined oil system, two processes were observed 1) increased water dispersions and water droplet growth in matrix and 2) residual oil displacement and mobilization in both matrix and fracture.

8.5.1 Water dispersions and water droplet growth in matrix

The highest salinity gradient was established between the brine and injected low salinity water in systems initially saturated by Brine B. Based on research by Ellila (2012) a high difference in salinity concentration will yield a high chemical potential between the aqueous phases increasing water flux through the oil membrane. The increased water flux cause water dispersions to grow within the oil as low salinity water diffuses through the membrane from areas with high chemical potential (low salinity) to areas of low chemical potential (high salinity). The difference in chemical potential induces water transport until equilibrium is reached and the contrast is reduced to zero by dilution.

In addition to water dispersions, water droplet growth along the pore wall was observed across the matrix field of view, as the low salinity water travelled by diffusion film flow coating the matrix grains. In surface roughness, transport was obstructed and droplets continued to grow until the water film coated the surface. As long as there was a significant driving force for water to accumulate and grow into droplets, *i.e.* osmotic gradient, water droplet growth would repeatedly occur as observed in Figure 8.5. As the osmotic gradient diminished, the growth ceased as illustrated in Figure 8.7.

The presence of water dispersions and droplet growth in matrix was sensitive to oil composition. The refined oil with higher carbon number, n-Heptane, showed less effective water flux compared to the refined oil of lower carbon content, *i.e.* n-Hexane. In the experiment conducted with n-Heptane only some larger pores exhibited water dispersion growth and coalescence as shown in Figure 8.4. Water

dispersions and water droplet growth was seen to greater extent in the n-Hexane oil membrane (*cf.* Figure 8.5).

The greater water flux through the n-Hexane membrane is confirmed by the Stokes-Einstein equation (*cf.* section 3.4, equation 3.2). The equation states that the diffusion constant D_{AB}, for fluid A through B, is inversely proportional to membrane viscosity. Oil compositions with lower carbon numbers have lower viscosity and water through n-Hexane will therefore have a higher diffusion constant than for n-Heptane. Fick's law (*cf.* equation 3.1, section 3.4) shows that water flux is proportional to the diffusion constant. The water flux, or water dispersion and droplet growth, should therefore be greater in the system primary drained by n-Hexane.

In addition, another important observation can be made from the system mentioned. Due to the density difference between oil and water, as water-in-oil coalesce into larger dispersions, the drops descended towards the water-wet glass window and adhered to the glass surface. This loss of larger water dispersions within the oil phase, when water was spread across the glass surface, reduced the potential for oil expansion.

8.5.2   Oil displacement and mobilization in matrix and fracture

For systems initially saturated by Brine A, a low osmotic gradient was established between the aqueous phases. In the presence of a lower salinity gradient, water dispersions and droplet growth were to a lesser extent seen. However, movement of interfaces, oil displacement and mobilization was observed to the fracture.

The low saline water injected to the system travelled along the water-wet pore walls of the grains into regions of high salinity brine. This film-flow caused the initial brine phase to expand, and the surrounding oil was displaced as illustrated by the inaccessible brine expansion in matrix of Figure 8.9 and near fracture in Figure 8.11. The movement of interfaces and displacement processes caused the change seen in Figure 8.8.

Oil production through lower fracture was also observed, and two mobilization processes of oil to fracture were visualized from the same pore throat in Figure 8.12 and 8.13. When oil was produced through the lower fracture it flowed with the rate of the injected low salinity water (0.042 ml/h) towards the production channel. As the water-oil interface swept the matrix-fracture boundary, mobilized oil droplets were produced together with the rest. In some cases, capillary retained oil droplets (*cf.* Figure 8.13 droplet B and D), or immobile droplets were left in the fracture (*cf.* Figure 8.13 droplet E).

8.5.3   Crude oil water-dispersion growth and displacement

The results obtained from the refined oil experiments were extended to investigate the effect of osmotic diffusion through a reservoir composite crude oil. Brine A (5wt% NaCl) was used to represent formation brine, implementing a relatively low osmotic gradient when injecting low salinity water. Brine A was chosen as the majority of oil displacement and mobilization processes occurred at low brine concentration in the refined oil experiments. Two different experiments were performed, one with a continuous crude oil membrane across the matrix, and another with a discontinuous residual oil membrane.

In the continuous oil membrane experiment (*cf.* Figure 8.14) oil production to fracture was observed within field of view together with redistribution of fluids in matrix. Crude oil pores were relocated with brine, and brine filled pores became drained by crude oil from connected pores as documented in Figure 8.16. Water diffusion was also evident through the water film coating the matrix grains. Crude oil displacement processes inside matrix are illustrated in Figure 8.15 and 8.17. In addition, crude oil was produced to fracture as seen in Figure 8.18.

By creating a discontinuous crude oil membrane within matrix the residual oil was to a greater extent surrounded by high salinity brine as presented in Figure 8.19. Water diffusion through film flow would hence have lesser effect on oil mobilization. During LSW it was observed that diffusion of low saline water through the residual crude oil membrane was the main mechanism for oil expansion and mobilization. Because water is to a certain degree soluble in oil, initial brine as water-in-oil was located within the crude oil phase. When injecting low salinity water, an osmotic gradient was established between the water surrounding the residual oil saturation and the water-in-oil inside the crude. This caused increased diffusion of low saline water through the oil membrane into the high saline brine. The water-in-oil expanded and accumulated into water dispersions. As the water dispersions coalesced, the oil phase expanded as observed in Figure 8.19 and 8.20. The growth of water dispersions due to low salinity diffusion is assumed to be the same as the water micro-dispersions detected by Emadi and Sohrabi (2013). The osmotic diffusion mechanism transports low salinity water into high saline water-in-oil through the oil membrane, were they grow into water dispersions and coalescence into water droplets.

9 Miscible CO$_2$ Injection in Tight Shales

Continuous miscible CO$_2$ injection was performed to document potential oil production from tight reservoir shale saturated with n-Decane and Ekofisk crude oil. Eight experiments were conducted and representative recovery factors were obtained by calculating the cores' weight before and after CO$_2$ injection, and by measuring volumetric oil production at the outlet. From the visualized recovery history, dynamic production profiles were made to investigate both the effect of miscibility and displacement, and production potential in terms of pore volume CO$_2$ injected. The flow capacity of the shale samples was also determined by accounting for compressible Darcy flow at test conditions.

9.1 CO$_2$ Gas Permeability in Tight Shales

During miscible CO$_2$ injection one objective was to estimate the effective end-point permeability for CO$_2$ related to shale flow capacity. From laboratory experiments, shales are found greatly sensitive to changes in confinement pressure also known as overburden stress (Heller and Zoback, 2013). Both measurements of fracture and matrix permeability depend greatly on confinement pressure. As mentioned earlier by Organi *et al.* (2011), induced hydraulic fractures in shale reservoirs degrades in consequence of increasing overburden pressure influencing the permeability of the rock matrix.

Matrix permeability decreases in pore size under high confinement pressures. From results presented by Heller and Zoback (2013) on measuring shale permeability, matrix reductions were observed to improved gas permeability through the network. The observed improvement was associated with increased gas slippage and Knudsen diffusion as the porous network was reduced to micro-pore level. Estimates provided by Heller and Zoback (2013) showed slip-flow to be significant for total flow capacity at pore-pressures below 400 psi, supposedly exceeding Darcy flow through the low permeable shale.

Wasaki and Akkutlu (2014) investigated the complexity of matrix permeability in organic-rich shale of dual porosity. Effects were found related to; 1) stress dependent permeability transport in inorganic slits and 2) "free" diffusion transport in organic- rich pores. The Knudsen number (*cf.* section 2.2.3) determines gas transport. Stress dependent permeability is induced when confinement pressures increase and the inorganic slit-pores (*i.e.* micro-fissures and fractures) close. The surface area associated with pore walls is reduced and the previously negligible effect of adsorbed gas increases as mean path decreases. The inorganic pore network moves out of the Darcy regime at $K_n \leq 0.01$, into slip -and diffusion-flow. In organic-rich pores holding significant volumes of adsorbed and dissolved hydrocarbons, diffusive transport is induced as inorganic pores close with increased stress (Wasaki and Akkutlu, 2014).

Methods commonly used for determining permeability of shale are core-scale laboratory gas injection, crushed samples or mercury intrusion (Cui *et al.*, 2009). The practical use of gas injection in shale is however reduced due to low injectivity, time scale and complexity of measuring small pressure drops and flow rates. Cuttings or crushed samples are more commonly used. However, one disadvantage of performing permeability measurements on crushed samples is loss of the naturally occurring micro-fractures in shale (Heller and Zoback, 2013). The most accurate method would be that of mercury intrusion on whole unconfined samples.

Choice of gas composition for measuring permeability is dependent on pore size distribution in tight shale. As surface area decreases within micro -and meso pores, contact area for gas molecules will increase. Some shales have well-developed micro-pore systems with unique transport capabilities related to specific gases (Cui *et al.*, 2009). Hence, permeability measurements vary for gases of different molecular composition and size. Because the main components in shale are hydrocarbons, natural gas *i.e.* methane (CH_4) is the preferred choice. This is because methane molecules exhibit a stronger molecular sieving effect than molecules of the normally applied N_2 -or Helium gases. However, when using methane kerogen adsorption effects have to be accounted for (Cui *et al.*, 2009).

In this thesis, gas permeability for shale is measured in relation to miscible CO_2 injection for oil production. When applying CO_2 gas for measuring permeability, certain assumptions and corrections have to be made. These are discussed further in section 9.1.1.

Opdal (2014) and Bø (2014) performed effective gas permeability measurements on shale using CO_2 gas at the Dept. of Physics and Technology. The calculated permeabilities were based on measured values by Darcy's law for incompressible fluids, and showed great variations in the mD-range. However, one important observation was reported. Originally, shale cores were wrapped in aluminium foil to protect the core-holder's rubber-sleeve from CO_2 damage. When visualizing CO_2 flow through PET/CT images at Haukeland University Hospital (HUH), it was observed that the injected CO_2 bypassed the core along the aluminium foil. Hence, permeability measures were conducted without foil and the permeability values improved significantly in the µD-range. Opdal (2014) and Bø (2014) also confirmed the importance of high net confining pressures to enforce CO_2 flow through the core.

9.1.1 Assumptions when estimating shale permeability

The following assumptions were made when estimating shale permeability during miscible CO_2 injection.

Non-Darcy flow

Because pore sizes in tight shale formations are a thousand times smaller than in conventional reservoirs *e.g.* sandstone, gas flow is expected to be a combination of Knudsen and/or slip-flow. Hence, Darcy's law cannot be used directly and modified versions are generally applied accounting for non-Darcy behavior. The Knudsen number quantifies the effect of increased gas slippage against pore walls due to reductions in mean free path. Laminar flow by Darcy's equation resides within the viscous flow regime by Knudsen number. If slip-flow occurs, flow transitions from the viscous into the slip-flow regime require corrections by the Klinkenberg equation. These corrections are generally made at gas pressures below 10 bars (Zolotukhin and Ursin, 2000).

Effects of inertia and turbulence will alter the conditions for laminar Darcy flow if high flow rates are applied in the viscous regime. At high rates, increased pressure drops across the core identify the presence of inertia. Gas permeability will in this case deviate from Darcy conditions, and versions modified by the Forchheimer equation are applied. When estimating CO_2 gas permeability, potential effects of inertia or slip-flow has to be accounted for as liquid and supercritical CO_2 are highly compressible through the micro -and macro pores of the network.

The miscible CO_2 injections performed in this thesis were applied at constant differential pressure and at low flow rates ranging from 2.1 ml/h – 26.2 ml/h. It was reasoned that with induced rates being this low the effects of inertia would be insignificant. In addition, all injections were performed at absolute pressures above 160bar (2000 psi), which should make the Klinkenberg effect negligible. These assumptions are supported by the findings of Swami and Clarkson (2012), and Sanaei *et al.* (2014), who report deviations from Darcy permeability at pressures below 5000 psi and 2000 psi respectively. Above these levels, the ratio of apparent gas permeability to Darcy permeability is observed to be close to 1. The experiments performed in this thesis apply pressures above 2000 psi which is the lower limit estimated by Sanaei *et al.* (2014). Hence, the permeability measurements by CO_2 injection were only modified for compressibility applying Darcy's law for compressible gases (*cf.* equation 2.5, section 2.2.3).

Gas Compressibility Factor
Darcy's law for compressible gases assumes ideal gas behaviour at low pressures for a mean pressure relationship to be valid (Ahmed, 2006). However, CO_2 is a real gas, and real gases behave differently. The deviation from the ideal gas law increases with increased pressure and temperature, and varies with the composition of the gas (Ahmed, 2006). A change from moderate to high pressures will hence influence its volumetric properties, and corrections have to be made for compressibility. A correction factor called gas-compressibility factor (Z-factor) is introduced to account for real gas behavior.

By applying the gas properties for CO_2, the Standing-Katz chart can be used to determine the Z-factor (Skarestad and Skauge, 2012). However, the chart is generally related to natural gases and can only be applied if the fraction of non-hydrocarbons is less than 5%.The CO_2 used in this thesis is a non-hydrocarbon gas with purity > 99,999% CO_2 (*cf.* Table 5.1 section 5.1) and a correction factor for compressibility is therefore not accounted for. It is assumed that the Z-factor is equal to 1 and that CO_2 behave as an ideal gas.

Effective End-point Permeability of CO_2
Darcy's law for gas compressibility was applied to calculate the end-point effective permeability for CO_2 (*cf.* Equation 2.5). The permeability was calculated using the 50 last readings of injection rate and differential pressure (logged by the SP-pump and ESI-transducers) after oil production had ceased. The geometric shale properties are found in Table 5.2, section 5.3.

When calculating the effective end-point permeability changes in viscosity and density of CO_2 across the core were accounted for. As the pressure is lower at the outlet, the rate of CO_2 will be higher downstream. Hence, the end-point effective permeability was calculated at both upstream and downstream conditions, and an effective permeability value across the core was calculated for each sample.

The absolute permeability of a porous medium is related to effective and relative permeability by the equation,

$$K = \frac{K_e}{K_r} \tag{9.1}$$

Where K is the absolute permeability of shale (D), K_e is the CO_2 effective end-point permeability (D), and K_r is the CO_2 relative permeability (D) (Zolotukhin and Ursin, 2000).

To relate the calculated effective end-point permeability of CO_2 to the absolute permeability of shale, assumptions were made regarding the end-point relative permeability. Generally, relative permeability values lie in the range 0-1 depending on the distribution of the saturating phase. Because CO_2 is the only phase flowing at the end of production, an end-point relative permeability can be assumed.

Shale formations are mainly oil-wet (Fakoharenphol *et al.*, 2014), and in oil-wet reservoirs the end-point relative permeability of water at residual oil saturation is generally greater than 0.5 (Zolotukhin and Ursin, 2000). Because mobility is higher for gas than water, end-point relative permeability of gas (K_{rg}) is assumed to be $0.5 > K_{rg} > 1$. Hence, a minimum and maximum range is provided for the absolute shale permeability at 0.5 and 1 respectively. The results of the permeability calculations are shown in Table 9.1, section 9.1.2.

9.1.2 Evaluation of shale permeability measurements

Unconventional shales correspond to source rocks of low permeability, overlaying or underlying hydrocarbon reservoirs. The low matrix permeability and diffusivity potential creates a mass-transport barrier between the ~2.0 µm pore throat size of reservoir rock and ~0.05 µm size of low permeable shale (Nelson, 2009). The characterization of permeability in terms of pore throat size is given in orders of magnitude, and a reduction in throat size corresponds approximately to two orders of reduction in permeability (Nelson, 2009). In this thesis, if the pore throats are assumed to be maximum 1 µm (macro-pores by Kuila *et al.*, (2012) section 2.2.2), the permeability values will be in the range from micro -to nano-Darcy.

Table 9.1 lists the absolute permeability values for the 8 experiments conducted. The average permeability value for each sample is highlighted in red, blue and green for shale core 12iA, 3i and 4i respectively.

Table 9.1 - Absolute permeability measurements of shale cores 12iA, 3i and 4i

Core ID	Differential pressure [bar] ±0.57	Absolutt shale permeability [µD]		
		Maximum (K_{rg} = 0.5)	Minimum (K_{rg} = 1.0)	Uncertainty[1]
12iA_1	77.86	0.0055	0.0028	± 3.0E-5
12iA_2	79.74	0.0027	0.0014	± 1.0E-5
12iA_3	72.33	0.0038	0.0019	± 2.0E-5
12iA_4	70.04	0.0013	0.00064	± 1.0E-5
12iA		= 0.0033	=0.0017	=± 3.0E-5
3i_1	29.52	0.025	0.013	± 2.0E-4
3i_2	70.88	0.020	0.010	± 6.0E-5
3i		=0.023	=0.011	=± 2.0E-4
4i_1	67.76	0.0077	0.0038	± 4.0E-5
4i_2	69.16	0.0081	0.0041	± 4.0E-5
4i		=0.0079	=0.0039	=± 4.0E-5

1) *Uncertainty is calculated by equation A3, Appendix A. Uncertainty is set as the highest individual error.*

Shale absolute permeabilities were estimated to be in the $10^{-2}\mu$D-range. Shale sample 12iA was calculated to have the lowest absolute permeability with a maximum value of 0.0033±3E-5µD (*cf.* Table 9.1). Sample 4i showed a moderate value of 0.0079±4E-5 µD, and sample 3i yielded the highest permeability of 0.023±2E-4 µD (uncertainty values associated with instrumental errors are calculated to be low). The varying permeability values for the 12iA n-Decane experiments in Table 9.1 are due to the high oil recovery during CO_2 injection. When the gas flow is obstructed by less residual oil, the effective end-point CO_2 permeability will increase.

Some conclusions can be drawn between shale flow capacity and structural compositions by comparing the results to the CT-scans provided by Graue *et al.* (2014) in section 5.3. An image montage of CT scans for shale 3i is shown in Figure 5.6. The image shows straight laminations dominating throughout the sample, and no distinct high-density zones are observed. For shale sample 4i (*cf.* Figure 5.7) regions of higher density are seen together with laminations progressing through the core. Shale 12iA however (*cf.* Figure 5.8) shows a structural composition of patchy high-density zones in a tight texture without the prominent laminations of shale 3i and 4i. This is in agreement with the samples being extracted from different sections or layers of the shale formation.

The high permeability values in cores 3i and 4i indicate that their laminated structures favor fluid flow. In addition to laminations, core 4i has areas of higher density, which in turn may hinder flow resulting in the moderate permeability. For 12iA the absence of laminations and the presence of patchy areas of high density appears to be responsible for the low permeability. As shale 3i exhibits the highest flow capacity, recovery potential from this reservoir region is assumed to be highest.

Based on the formation structure from which the samples were extracted (*cf.* section 5.3) it is suggested that shale 3i may be related to the middle section of producible sand -and siltstone reservoir rock where permeability is sufficiently high to induce flow. Shale 4i of moderate permeability may originate from the lower section constituting a source rock of high organic content. Hence, the composition of the tight textured matrix in shale 12iA of lowest permeability, with no structures for flow, may belong to the upper shale layer, composing a seal for the two underlying formations.

To have knowledge of the estimated permeability values, will be of importance when describing flow behavior during miscible CO_2 injection and oil recovery performance. Darcy's law for compressible fluids is further applied by making the assumptions of section 9.1.1 when calculating the effective CO_2 permeability during miscible CO_2 injection in section 9.4.

9.2 Repeated Oil Saturation of Shale Cores

The shale samples had to be re-saturated between the experiments prior to performing miscible CO_2 injection. The three samples were re-saturated several times, mainly by crude oil (shale 3i and 4i) but also with n-Decane (shale 12iA).

The results of the 3D-saturation of shale cores are shown in Table 9.2. Maximum saturation in terms of 100% pore volume for shale core 12iA appears to be overestimated for all re-saturations: more oil enters the core than theoretically possible. This overestimation was not observed in shale cores 3i and 4i. The uncertainty associated with saturation values for 12iA is related to the core porosity. The porosity was set to 5% because accurate porosity data was not provided. Based on the achieved oil saturations from weight measurements listed in Table 9.2 a porosity of 5% looks underestimated in this case.

For shale cores 3i and 4i the estimated porosity values (~4.8% and ~4.5% respectively) shows better agreement. From Table 9.2 the first re–saturations by crude oil yields 79% and 77% oil saturation respectively for core 3i and 4i. During miscible CO_2 injection, it is unlikely to obtained 100% oil recovery and small amounts of residual oil within the porous network may exist after production. The achieved re-saturations depend on the amount of oil present before the re-saturation step. This may be observed from the saturation values during the second re-saturation of shale 3i and 4i: 4% and 15% lower oil saturation was achieved compared to the first saturation.

Table 9.2 - Results from re-saturations of shale cores, including saturation fluid and temperature conditions

Core ID	Saturation fluid	Temperature [°C]	Volume oil injected [ml] [1]	Oil saturation [%PV] [1]
12iA_1	n-Decane	25	1.57 ± 1E-02	112 ± 1E-02
12iA_2	n-Decane	25	1.72 ± 1E-02	123 ± 1E-02
12iA_3	n-Decane	60	1.75 ± 1E-02	125 ± 1E-02
12iA_4	Ekofisk crude oil	60	1.58 ± 1E-02	113 ± 3E-02
3i_1	Ekofisk crude oil	60	1.63 ± 3E-02	79 ± 2E-02
3i_2	Ekofisk crude oil	60	1.54 ± 3E-02	75 ± 2E-02
4i_1	Ekofisk crude oil	60	1.54 ± 3E-02	77 ± 2E-02
4i_2	Ekofisk crude oil	60	1.23 ± 3E-02	62 ± 2E-02

[1] Uncertainties are calculated by equation A4 and A5 in Appendix A.

The samples were also exposed to some damage and fragmentation during the experiments, and may have reduced bulk -and pore volumes. This will reduce the volume accessible during re-saturation. The saturation values were used when calculating oil recovery during miscible CO_2 injection, and the estimated recoveries are presented as follows.

9.3 Oil Recovery by Mass Balance and Volumetric Production

During miscible CO_2 injection, estimates of oil recovery were calculated and quantified by both mass balance and volumetric production. The production results are tabulated in Table 9.3.

The oil displaced during miscible CO_2 injection is flashed at the outlet when measuring volumetric production, and the amount of oil produced is recorded as a function of time. However, because of the small pore volumes containing oil in shale (≤ 2.00 ml, *cf.* Table 5.2) potential recovery at the outlet is associated with large uncertainty. If the oil produced by miscible CO_2 is obstructed within tubing and fittings, or if there are leakages in the system, small quantities of oil might be lost and remain undetected at the production outlet. To provide a separate, independent estimate of oil recovery, the cores were weighed before and after CO_2 injection to calculate oil production from changes in mass. The difference in recovery between the two methods is called "production difference".

Table 9.3 - Oil production calculations with mass balance and volumetric measurements during miscible CO_2 injection in tight shale

Core ID	By mass balance[1]		By volume[1]		Production difference[1] [%OOIP]
	Oil produced [ml]	R_f [%OOIP]	Oil produced [ml]	R_f [%OOIP]	
12iA_1	1.79 ± 3E-02	114.04 ± 2E-02	1.40 ± 5E-02	99.7 ± 5.2	14.3 ± 5.4
12iA_2	1,79 ± 3E-02	104.00 ± 2E-02	1.45 ± 5E-02	103.3 ± 5.3	0.7 ± 5.5
12iA_3	1.68 ± 3E-02	96.06 ± 2E-02	1.00 ± 5E-02	71.2 ± 4.5	24.8 ± 4.7
12iA_4	1.49 ± 4E-02	92.37 ± 4E-02	0.45 ± 5E-02	32.1 ± 3.8	60.3 ± 5.2
3i_1	1.58 ± 4E-02	97.04 ± 3E-02	1.60 ± 5E-02	77.5 ± 3.6	19.5 ± 4.8
3i_2	1.39 ± 4E-02	89.84 ± 3E-02	0.40 ± 5E-02	19.4 ± 2.5	70.5 ± 3.9
4i_1	1.17 ± 7E-02	75.78 ± 3E-02	0.40 ± 5E-02	20.0 ± 2.6	55.8 ± 3.9
4i_2	1.27 ± 3E-02	102.94 ± 3E-02	0.45 ± 5E-02	22.5 ± 2.6	80.4 ± 4.3

[1] Uncertainties are calculated by equation A4 and A5 in Appendix A.

Continuous miscible CO_2 injection in tight shale is commonly assumed to yield little oil recovery due to low injectivity and low permeability of the rock. As seen from Table 9.3, high recovery factors were obtained by the measured weight differences ranging from 76-114% while recovery factors obtained by visually reading off the volume exhibited a larger range. The oil recoveries listed in Table 9.3 is discussed in detail below, focusing on the difference between oil recovery calculated by mass balance and volumetric measures. Temperature effects and influence of oil phase is also discussed.

9.3.1 Recovery by Mass Balance

The recovery factors obtained by weight reduction of shale cores 12iA_1 and 12iA_2 (*cf.* Table 9.3) appear to exceed 100%OOIP. In both tests the core was saturated with n-Decane and CO_2 injection was conducted at room temperature (25°C). It was observed that the produced oil phase was not clear, indicating that the n-Decane may have mixed with heavier compounds from residual crude oil. This may have mobilized previously immobile residual oil and resulted in a production higher than 100%.

A density measurement of the produced n-Decane/crude oil mix would provide a better estimate of recovery, but the small volume produced made accurate density measurements difficult. By correcting for n-Decane density the remaining uncertainty would be related to porosity. More accurate porosity values could then be estimated for 100% saturation in terms of PV (*cf.* equation 7.1).

Shale core 4i_2 also shows a recovery value exceeding 100%OOIP. Contrary to the experiments performed with n-Decane, it was observed that the produced oils during the crude oil experiments were lighter in composition than the crude oil injected during saturation. Ekofisk crude is a black and

heavy-component oil (*cf.* Table 5.1), but the oil phase produced was light brown. One explanation could be that the small pores and tight matrix of the shale samples acted as filters during saturation, passing only the lighter volatile components of the crude, excluding the heavier components. If a lighter crude composition was initially present, the saturation values calculated in section 7.2.3 could be underestimated (*cf.* Equation 7.1). Hence, more oil could be recovered as more oil saturated the sample.

The filter-theory was later abandoned by new experiments in a modified setup with shorter tubing and improved cooling system (ref. master student Arthur Uno Rognmo).This was done after finding oil components in downstream tubing and the back pressure regulator during inspection, *i.e.* the heavier components had precipitated on the tube wall during de-pressurization, which corresponded with the observation of light brown oil being produced. Experiments performed in the modified setup resulted in production of black crude of initial composition. Hence, the high recovery value for shale 4i_2 appears to be the result of increased miscibility and mobilization of residual crude oil rater than uncertainties in oil density/saturation.

Oil recovery estimations based on mass reduction have a higher uncertainty from experimental inconsistency compared to instrumental uncertainty. In these cases, the uncertainties are more related to the density and porosity values when calculating oil saturation before and after CO_2 injection. The uncertainty in density, especially for experiments with n-Decane, has not been quantified and the porosity values were only estimated. In addition, several re-pressurizations and injections of CO_2 were performed during the experiments resulting in varying recovery performance (%OOIP) proportional to the amount of CO_2 injected.

9.3.2   Volumetric Oil Recovery

Estimation of recoverable oil during CO_2 injection in shale by volumetric production indicated lower recovery factors (%OOIP) compared to mass balance calculations (*cf.* Table 9.3). In addition, the volumetric values exhibit higher instrumental uncertainty to the values obtained by weight reduction. As the volumetric oil recovery was related to the pore volume of the given sample, not the change in saturation, higher uncertainties were associated with measuring the small volumetric quantities by instrumental and human errors than by the experimental uncertainties during mass balance. The discrepancy in recovery by volume and mass balance is indicated by "production difference" in Table 9.3. The production difference shows a greater dependence on the instrumental uncertainties related to the volumetric recovery than to those by mass balance.

Production difference

The bar diagram in Figure 9.1 shows total recovery by volume superimposed on recovery by mass balance for the various tests. The y-axis shows recovery factor (%OOIP) for the 8 CO_2 injections performed on the three shale samples. The red bars represent recovery from tests with shale sample 12iA, and the blue and green show recovery from samples 3i and 4i, respectively. The production difference is mainly related to precipitation of heavier components as the system pressure sinks below individual MMPs for the miscible phase.
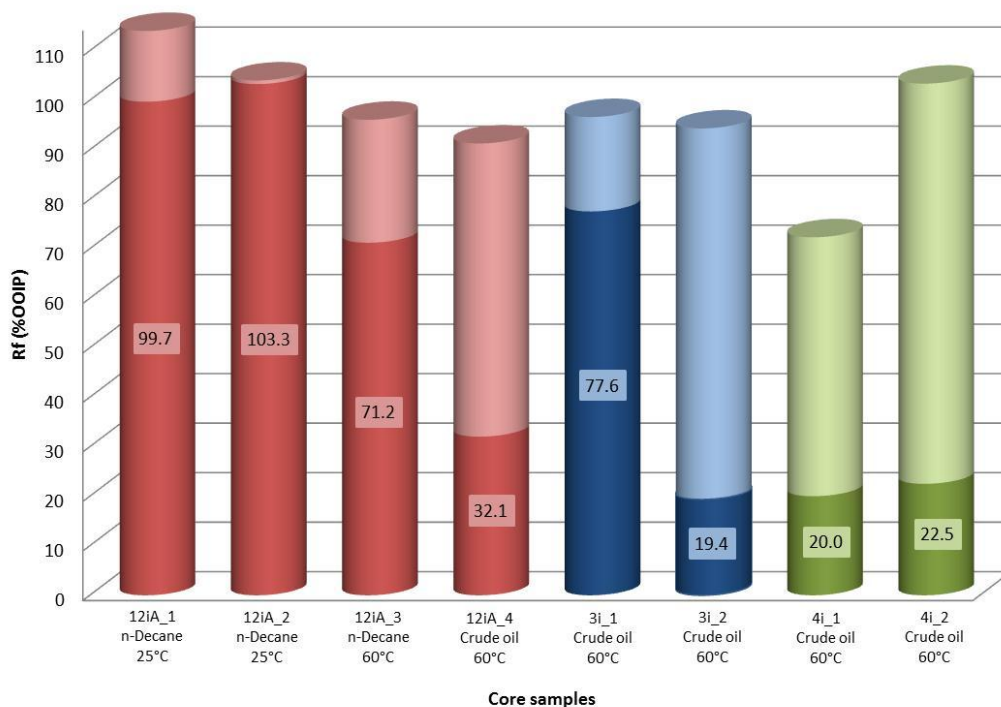
Figure 9.1 - Total oil recovery during CO_2 injection for the three shale samples by mass balance and volumetric production. The red bars show the recoveries from shale 12iA, both n-Decane and crude oil. The blue bars represent crude oil recovery from shale 3i, and green bars represent the same for 4i. Total recovery by weight difference is illustrated by the overall height of the bar. The section in heavy color is recovery obtained from volumetric production marked with representative values. The lighter areas on the bar graphs illustrate the production difference between the two methods

N – Decane production

The two n-Decane tests on shale 12iA at 25°C show less production difference than the n-Decane and crude oil test at 60°C. At room temperature n-Decane will be first-contact miscible with the injected liquid CO_2 at pressures above 90 bar (Ahmed, 2013), and will remain in solution at 150 bar until they are produced to atmosphere through the BPR.

As mentioned previously, the injected n-Decane seems to be soluble with residual crude inside the porous network, and hence the amount of oil recovered by mass balance exceeds OOIP. The difference between mass and volumetric production for shale 12iA_1 is greater than for 12iA_2, which might be attributed to higher amounts of heavy components being released as the crude and n-Decane mixture consists of hydrocarbons with various MMPs. The second n-Decane test 12iA_2 represents a better correlation between recovery by mass balance and produced volume because residual crude oil has already been partially produced.

A CO_2 injection test Shale 12iA_3 with n-Decane was also performed at 60°C to investigate the miscibility effect on recovery at elevated temperature. The result shows a reduced oil recovery compared to results at 25°C and an increase in production difference. Miscibility with residual crude increases with temperature hence the heavier components are separated by the reduction in pressure and temperature when produced.

88

Crude oil production

Experiments with Ekofisk crude oil saturated cores were performed on all shale samples at 60°C to determine recovery potential closer to reservoir conditions. Pressures above 200bar were applied during all CO_2 injections to obtain miscibility between supercritical CO_2 and crude oil. The results from CO_2 injection in crude oil saturated cores are shown in the Figure 9.1 for tests 12iA_4, 3i_2, 4i_1 and 4i_2. The trend observed for all crude oil experiments is that total recovery in terms of mass balance is high, between 75% (4i_1) to 103% OOIP (4i_2), but recovery in terms of volumetric production is low, between 19.4% (3i_2) to 32% OOIP (12iA_4). The difference in production is mainly related to the different MMPs for the various crude oil components.

One exception to the crude oil trend was observed for shale 3i_1. This sample gave oil recovery of 97%OOIP by mass balance, and 77% by measured volumetric production (*cf.* Table 9.3). When performing miscible CO_2 injection a leak was detected through the inlet valve 4 (*cf.* Figure 7.1). In pressurizing the system with CO_2 the inlet and outlet valves 4 and 6 were closed until opened for applying a differential pressure across the core. Molecular diffusion may have occurred because of this valve leakage, mixing CO_2 with crude oil until miscibility is achieved before opening the valves. When production is initiated the miscible bank of crude and CO_2 is displaced towards production. Hence, some heavy crude is lost due to MMP variations (*cf.* Figure 9.1), but a higher recovery is achieved because of the established miscibility.

Production profiles for both n-Decane and crude oil experiments are discussed in the following section to investigate displacement efficiency during the miscible CO_2 injections.

9.4 Dynamic Production

Oil production was recorded during both liquid and supercritical CO_2 injection by measuring oil flashed at the outlet as a function of time and injected CO_2 pore volume. Time zero was set at the first sign of production at the outlet.

Profiles illustrating dynamic production are presented below for 5 experiments were production data was collected. Note that total recovery for the dynamic production profiles are not consistent with recovery measured by volumetric production. The dynamic production data gives the amount produced during CO_2 injection, while the volumetric data includes the additional amount obtained when de-pressurizing the system. Fundamental n-Decane tests are described prior to the crude oil experiments, the latter at simulated reservoir conditions.

N – Decane production

Tests were performed with n-Decane to investigate oil production from low permeable shale by first-contact miscible CO_2 injection. The injected CO_2 was liquid at 100bar and 25°C with a mobility ratio close to one with n-Decane. Subsequently, system temperature was increased to 60°C to create a less favourable mobility ratio. These tests were performed as a foundation for subsequent crude oil experiments, where mobility ratio between supercritical CO_2 and crude would deviate further from unity.

Figure 9.2 shows the recovery profiles for the first-contact miscible CO_2 and n-Decane displacements at 25 °C and 60 °C (12iA_2 and 12iA_3) versus the pore volume liquid CO_2 injected.
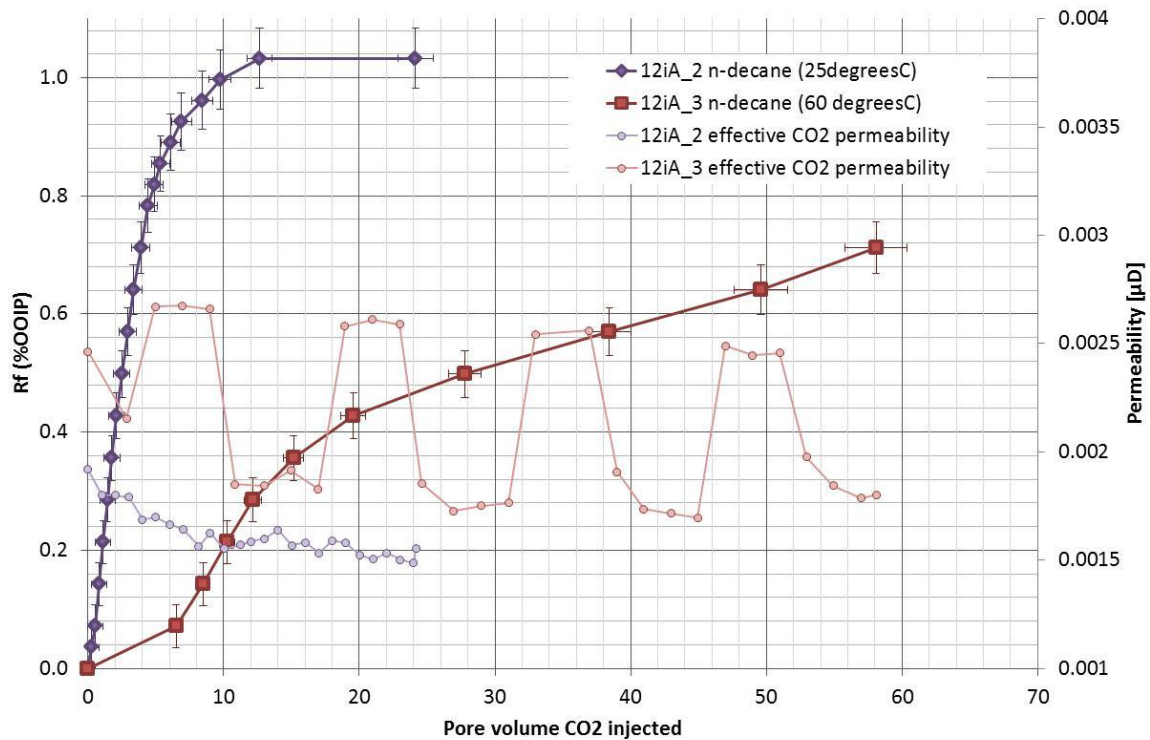

Figure 9.2 - n-Decane recovery performance for shale 12iA_2 and 12iA_3 versus pore volume CO_2 injected. The experiments were conducted at 25 °C and 60 °C, respectively. The solid squared graphs, in purple and red, show recovery factors for 12iA_2 and 12iA_3 respectively. The secondary y-axis on the left shows the effective permeability of CO_2 for each miscible displacement illustrated by the circled dots in light purple and light red. Error bars are presented indicating uncertainty in recovery and pore volume injected. The errors are higher at the end of recovery as oil production decreases and the injected pore volume CO_2 increases.

12iA_2

The total recovery for 12iA_2 at 25 °C was observed to exceed 100% with maximum recovery observed after approximately 12 pore volumes (PVs) of liquid CO_2 injected. Because liquid CO_2 was first contact miscible with n-Decane the two liquids were produced together as one hydrocarbon phase. The mobility ratio between the phases was close to unity, providing optimal microscopic displacement.

By direct miscibility, the front saturations flowed with constant velocity illustrated by the linear performance during the first 1-4 PVs CO_2 injected (Figure 9.2). Near 80% recovery (%OOIP) was obtained at this time. From 4-12 PVs CO_2 injected, the recovery entered a transition zone producing decreased amounts of n-Decane. The injected CO_2 eventually dominated the pore space when the bulk part of recoverable oil was produced. Over 100% recovery (%OOIP) was obtained for the test. Section 9.3.2 explains the reason for the overestimation. Effective permeability of CO_2 remained relatively constant throughout the displacement process. The minor decline indicates that the CO_2 injection rate and differential pressure were reaching a steady state after initial pressurization.

<u>12iA_3</u>

An adverse mobility ratio was established by increasing the temperature to 60°C in a subsequent injection test (12iA_3). Total recovery of 70%OOIP was observed after approximately 58PVs CO_2 injected. This equalled 46 PVs CO_2 more compared to n-Decane at 25°C (12iA_2). The curve (*cf.* Figure 9.2) indicates that the experiment was terminated before maximum recovery was reached.

At elevated temperature, the mobility ratio exceeds one as the viscosity of n-Decane is decreased (*cf.* Table 5.1) and the viscosity of liquid CO_2 increases (*cf.* Figure 4.3/Table 5.1). The unfavourable mobility ratio causes a long tail production. After breakthrough in Figure 9.2, 6PVs of CO_2 were injected before a continuous production developed. Subsequently, the production moved into a transition zone. After approximately 28PVs CO_2 injected the recovery showed a linear relationship indicating that constant amounts of n-Decane were being produced.

At 60°C, the higher effective CO_2 permeability (*cf.* Figure 9.2) indicated that the CO_2 injection rate was increased through the core and channelling had most likely occurred prior to miscibility. Because of the reduced viscosity of n-Decane and increased viscosity of CO_2, the CO_2 flowed through the channelled paths in favour of displacing the surrounding oil. With continuous CO_2 injection molecular diffusion will serve as the main recovery mechanism. A shift in recovery is observed by the transition zone (*cf.* Figure 9.2) and n-Decane production increases due to molecular diffusion. Sudden increases and decreases in CO_2 injection rate caused variations in the effective CO_2 permeability. The reason is unclear but assumed to be related to fluctuations in the SP-pump when injecting CO_2. However, the development remained stable.

<u>CO_2 Quantities Injected</u>

To obtain the presented recoveries for 12iA_2 (>100%OOIP) and 12iA_3 (70%OOIP), substantial amounts of CO_2 had to be injected. For 12iA_1, over 10PVs CO_2 were flooded before production ceased, and equivalently for 12iA_3 58PVs were required. In view of the small pore volume of oil in shale, it would be of interest to know why so large quantities (PVs) of CO_2 are needed for maximum oil recovery. The quantity of oil produced from shale is determined by the distribution and connectivity of organic matter, and it is widely accepted that shale has a matrix with varying degrees of interconnectivity between organics and inorganics (Vega *et al.* 2013). Storage for hydrocarbons lie within the porosity of the organic matter (Curtis *et al.* 2014), but for flow to occur the organics have to be connected to some degree.

Vega *et al.* (2013) assumed that the different density areas in shale could indicate predominantly organic and inorganic matter matrices. Research was performed applying full field transmission X-ray microscopy (TXM), and organic and inorganic matter was identified based on the relationship between X-ray adsorption and density.

In section 5.3 (*cf.* Figure 5.8) an image montage of CT-scans taken for shale 12iA is provided. The sample consists of a tight-textured low density matrix with patchy regions of high-density. If the zones of higher density consitiutes the organic content of the rock, the long tailed recovery could be explained based on molecular diffusion into these low permeability high-density regions, hence explaining the amount PVs of CO_2 required for recovering the producible oil. Results from Vega et al. (2013) however, indicated that the darker low-density areas were organic kerogen, while the lighter

high-density areas represented inorganic pyrite. Hence, the slow diffusion process could not be concluded based on reduced accessibility to oil saturated high-density regions in shale.

However, shale 12iA exhibited the lowest flow capacity with CT-scans revealing a tight textured matrix. If unidentified micro-fractures exist through the core (cannot be concluded based on the CT-scans) channelling may be induced. Because of the tight texture, molecular diffusion will be slow and high supplies of CO_2 are required for counter-current production. In laminated shales *i.e* samples 3i and 4i, the recovery process may be favoured by molecular diffusion occurring faster between laminations. However, fundamental experiments with n-Decane were not performed for shale 3i and 4i, and the issue cannot be concluded without further experimentation.

Based on the n-Decane experiments, oil was produced by first-contact miscible CO_2 injection. To assess recovery at reservoir conditions, molecular diffusion was investigated in crude oil saturated cores by supercritical CO_2 injection.

Crude oil production

Due to positive results from the fundamental n-Decane tests, the experimental conditions were changed to simulate reservoir by saturating the samples with Ekofisk crude oil. The CO_2 injections were performed at pressures above 200bar and 60°C. Hence, under these conditions, CO_2 was in supercritical state (*cf.* Figure 4.2, section 4.2.1). Due to composition and temperature, the viscosity of crude oil is greater than n-Decane (12iA_3) and a larger mobility ratio was expected. This could lead to early breakthrough with molecular diffusion being the main recovery mechanism. The experimental objective was to determine displacement, quantities of oil produced and CO_2 required for maximum oil recovery.

The following graphs represent the dynamic production of crude oil from shale cores 12iA_4, 3i_2 and 4i_2 at 60 °C by supercritical CO_2 injection illustrated in Figure 9.3.
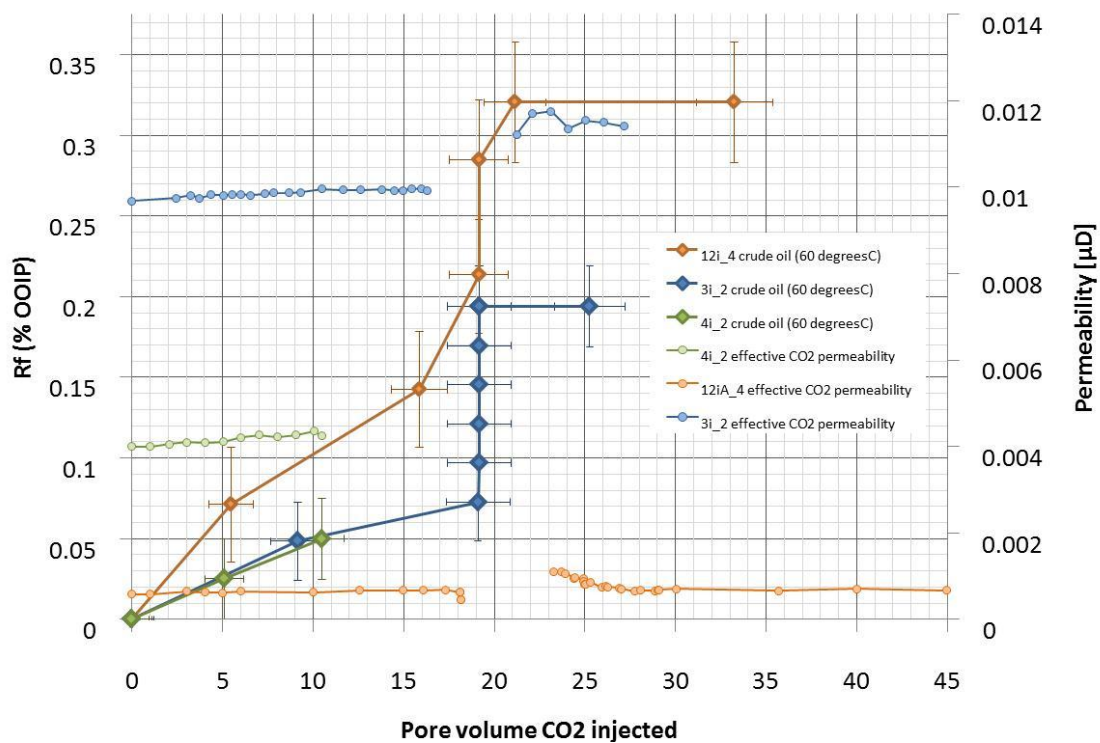

Figure 9.3 - Crude oil recovery performance for shale cores 12iA_4, 3i_2 and 4i_2 versus pore volume supercritical CO_2 injected. The experiments are performed at 60 °C. Recovery performance for 12iA_4, 3i_2 and 4i_2 are shown by the squared dots in yellow, blue and green respectively. The secondary y-axis on the left shows the effective permeability of supercritical CO_2 for miscible displacement 4i_2 illustrated by the circled dots in light green. Error bars are presented indicating uncertainty in recovery and injected pore volume. The errors are higher at the end of recovery as oil production decreases and the injected pore volume CO_2 increases.

12iA_4, 3i_2 and 4i_2

From section 9.3.2, the recovery factors for the representative experiments 12iA_4, 3i_2 and 4i_2 showed a great difference in production measured by mass balance compared to volumetric recovery. This production difference is also observed in the dynamic production profiles of Figure 9.3. Compared to the earlier n-Decane experiments (12iA_2 and 12iA_3), a greater production difference was observed with crude oil.

Miscibility between supercritical CO_2 and crude oil is not immediately achieved upon first contact when injecting CO_2. To obtain miscibility, the supercritical CO_2 and crude rely on a process of chemical exchange between the phases called multiple-contact miscibility (Terry, 2001). During multiple-contact miscibility, a transition zone occurs at the boundary between the CO_2 and crude oil where the two phases are miscible. As the injected supercritical CO_2 contacts the crude oil a chemical exchange of intermediate components takes place through molecular diffusion. The intermediate gas components diffuse into the crude oil creating a lighter oil phase, which to a greater extent is miscible with the crude. Behind the transition zone a constant supply of supercritical CO_2 mix with residual crude, and in front, the crude continuously change composition until mobility is established towards the production outlet.

The type of multiple-contact miscibility described above is called condensing-gas-drive. If there are sufficient amounts of CO_2 available to supply condensing intermediates to the displacement process, there is a great potential for oil not to be left behind at the end of production (Terry, 2001). However, the low recoveries indicated by the production profiles in Figure 9.3 suggest that substantial amounts of CO_2 are required to produce crude from the small pore volume of shales.

Describing recovery performance in terms of displacement efficiency is difficult based on the obtained production profiles in Figure 9.3. Initially, the dynamic production increased steadily for injections 3i_2 and 4i_2 until 10PVs of CO_2 injected. For test 4i_2, the effective permeability of CO_2 showed a stabile flow until injection was stopped due to shortage of CO_2. For tests 12iA_4 and 3i_2 the accumulator was re-pressurized to increase recovery in a second CO_2 injection test.

The system was isolated (inlet valve 4 was closed) when refilling the accumulator (*cf.* Figure 7.1), and the effective permeability for CO_2 could not be determined as observed from the permeability graphs 3i_2 and 12iA_4 (*cf.* Figure 9.3). However, assuming that the CO_2 rate was zero within the system, there was still a differential pressure across the core to induce flow towards production and produce oil, as observed in the recovery profiles for shale 12iA_4 and 3i_2. When restarting the CO_2 injection after refilling the accumulator, no additional oil production was observed from either shale core because the majority of crude components had precipitated out of the condensing-gas-drive solution due to pressure decrease below MMPs.

Another trend is seen in Figure 9.3. 12iA_4 showed a higher recovery performance compared to 3i_2 and 4i_2. In earlier discussions, it was assumed that molecular diffusion in 12iA would occur at a slower rate than for 3i and 4i due to abscence of laminations. Based on the current graph correlation, the tight matrix and low permeability of shale 12iA seems to develop better multiple-contact miscibility. The results of Figure 9.3 suggest that molecular diffusion across laminations might be a slower process.

3i_1

One exception to the dynamic crude oil trend was observed for test 3i_1. The supercritical CO_2 experiment was discussed earlier in section 9.3.2 because it obtained a high volumetric recovery compared to the other crude oil experiments. It was suggested that molecular diffusion was the main mechanism behind the high recovery through a leaking inlet valve. During initial pressurization the supercritical CO_2 came in contact with the crude oil creating miscibility. Because the system was securely closed downstream, the miscible oil phase was first produced when the outlet valve was opened. Oil recovery exhibits a linear increase after breakthrough between 2-4PVs injected, similar to the first-contact miscible n-Decane test (12iA_2). After this, a transition zone is developed where molecular diffusion aids recovery through a long tail production until 24PVs are injected. The crude oil recovery performance for shale 3i_1 is illustrated in Figure 9.4.
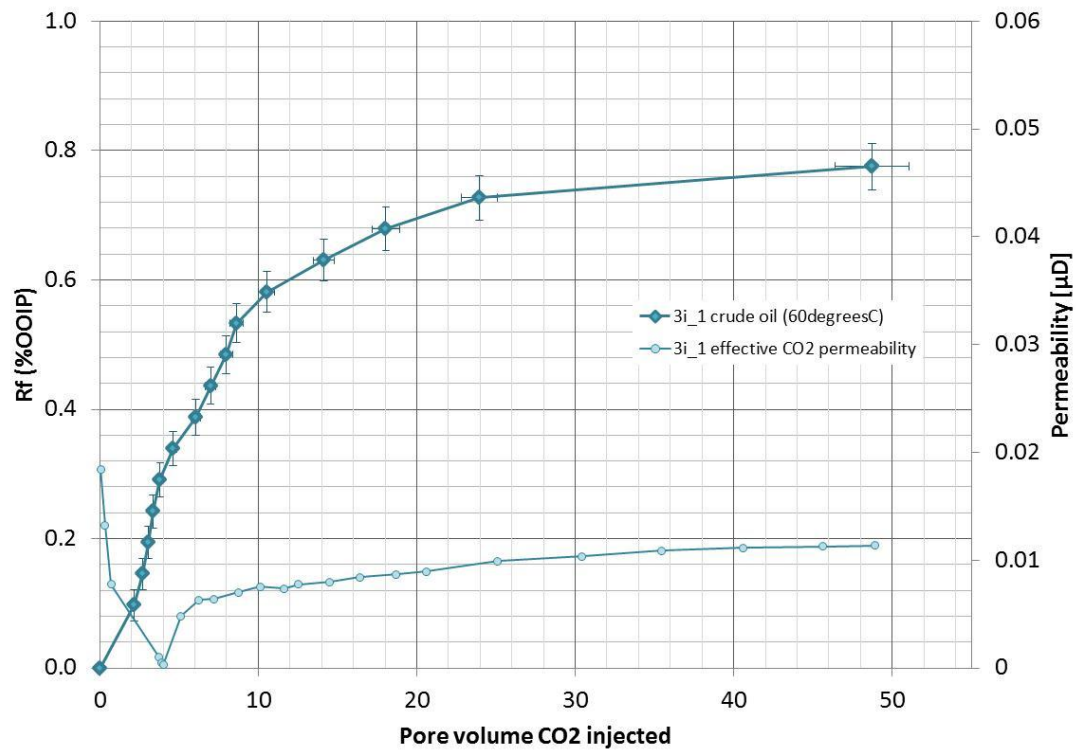
Figure 9.4 - Crude oil recovery performance for shale cores 3i_1 versus pore volume supercritical CO$_2$ injected. The experiment was performed at 60 °C. The squared dots in turquoise show recovery performance. The secondary y-axis shows the effective permeability of supercritical CO$_2$ for the miscible displacement illustrated by the circled dots in light turquoise. Error bars are presented indicating uncertainty in recovery and pore volume injected. The errors are higher at the end of recovery as oil production decreases and the injected pore volume CO$_2$ increases.

From Figure 9.4 it can be seen that the first sign of production is observed before CO$_2$ reached a stabilized effective permeability condition through the core. Because miscibility is achieved prior to opening the valve, the pressure build-up moves the miscible solution with constant velocity and the curve shows linear recovery before reaching the transition zone.

9.5 Evaluating Possible Recovery Mechanisms

During the fundamental n-Decane experiments, oil was produced through the small pore volume of shale 12iA by miscible CO_2 injection. At experimental conditions of 25°C and 100bar, first contact miscibility was established with a mobility ratio close to one. Under these conditions, 12 PVs CO_2 were injected before reaching maximum recovery and optimal microscopic displacement efficiency (*cf.* Figure 9.2). By changing test conditions to 60°C and 100bar for the next n-Decane test, an adverse mobility ratio was established between CO_2 and n-Decane, having respectively increased and decreased viscosity. Maximum recovery was not obtained after 58 PVs CO_2 injected and the experiment was ended (*cf.* Figure 9.2). Early breakthrough was observed at both 25°C and 60°C and recovery shifted into a long tailed production when the mobility ratio between the phases was increased. Large quantities of CO_2 were required to recover the producible oil by molecular diffusion.

Crude oil tests were carried out at 60°C and minimum 200bar to develop miscibility between the composite crude oil and supercritical CO_2. At experimental conditions, mobility ratio between the supercritical CO_2 and crude oil was assumed to be more unfavourable compared to the 60°C n-Decane experiment (12iA_3). All three tests (12iA_4, 3i_2 and 4i_2) showed early breakthrough and a slowly increasing recovery due to molecular diffusion and developed multiple-contact miscibility.

Descrepancies were observed when describing displacement efficiency for crude oil experiments 12iA_4 and 3i_2. When the systems were isolated during refilling of CO_2, the differential pressure slowly decreased and heavier crude oil components precipitated out of the condensing-gas-drive as pressures declined below MMPs. By the second CO_2 injection, no additional recovery was observed. However, during the shutdown period, oil was still recovered (*cf*. Figure 9.3) because of the apparent differential pressure across the core.

During crude oil recovery, 12iA showed higher production potential compared to 3i and 4i, even with significantly lower matrix permeability. Discussions regarding molecular diffusion were re-evaluated, and it was proposed that a tight-textured low-permeable matrix provided better means for multiple-contact miscibility. In addition, high recovery was observed when molecular diffusion was set to develop miscibility in a closed downstream crude oil system. The additional pressure build-up caused increased recovery when the miscible phase was eventually produced prior to continuous CO_2 injection.

By recording oil recovery as a function of time and PV injected, the effect of molecular diffusion as a potential oil recovery mechanism was evaluated through both miscible n-Decane and multiple-contact miscible crude oil experiments. The total production in terms of %OOIP is shown collectively for both n-Decane and crude oil experiments versus time in Figure 9.5.

Due to first contact miscibility, endpoint recovery is higher for n-Decane experiments than for crude oil, with the exception of shale 3i_1 (*cf.* Figure 9.5). The recovery performance indicates that the molecular diffusion process is significantly time dependent, especially through the small pore volume of shales. Accurate representation of crude oil recovery is required without heavy component release, to determine the effective crude oil displacement process. Generally, and based on the recovery efficency estimates, mass balance measurements show miscible CO_2 to be an effective oil recovery mechanism with the ability to provide high oil recovery factors for shale.
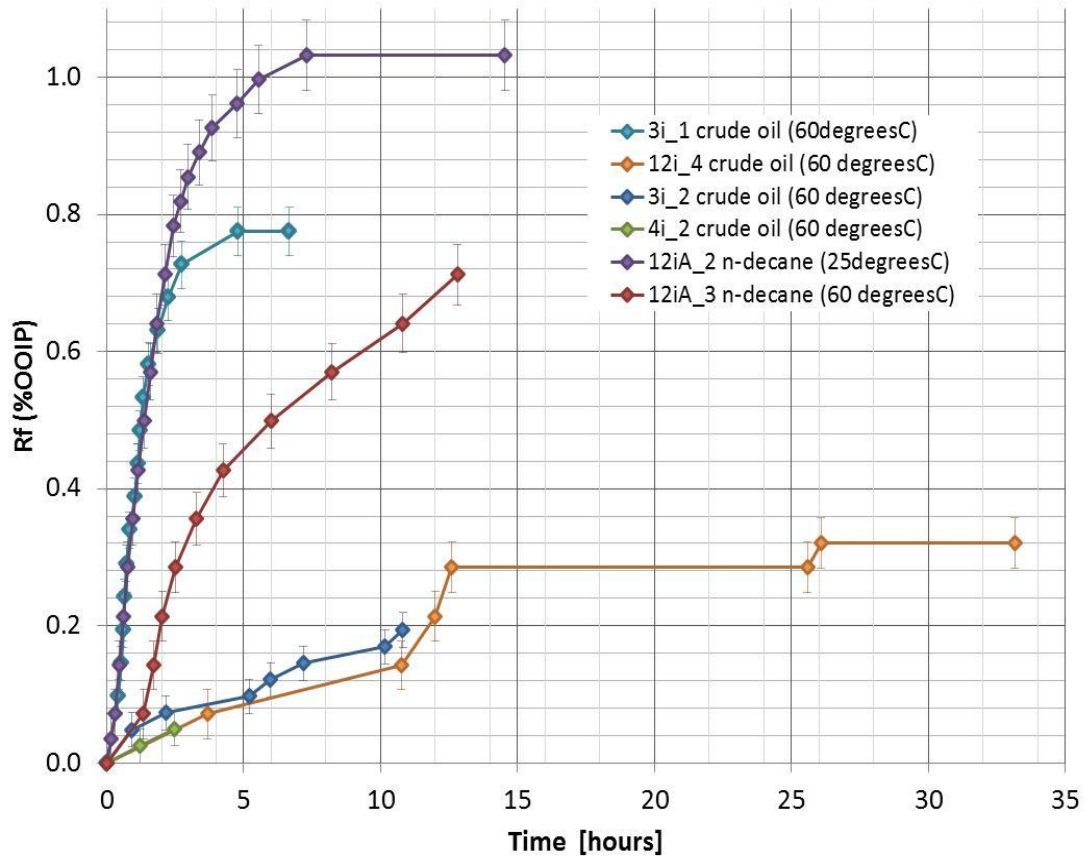
Figure 9.5- N-Decane and crude oil recovery for all 5 cores documented during dynamic production. The graph shows recovery factor (%OOIP) as a function of time (hours). Error bars are presented indicating uncertainty in recovery.

10 Conclusions

Based on the experimental study of diffusive oil recovery techniques during LSW in sandstones and miscible CO_2 injection in shales the following conclusions were made.

10.1 Osmotic Diffusion during Low Salinity Waterflooding

- Diffusive water transport was observed in micromodels of Berea sandstone when visualizing potential low salinity effects by LSW in a system initially saturated with high salinity brine. The diffusive water transport was observed as both film-flow along water-wet grains and osmotic diffusion through the oil phase.

- In the absence of a salinity gradient no fluid-fluid interactions or diffusive water transport was observed. With a salinity gradient between the initial high salinity brine and the injected low salinity water, effects of osmosis were observed through the oil phase depending on the difference in chemical potential and salinity concentration. The oil appeared to behave as an effective semi-permeable membrane for transporting low salinity water into high salinity regions, confirming the findings by Sandengen and Arntzen (2013).

- The first set of tests through a refined oil membrane revealed two effective processes by the diffusive water transport, 1) increased water dispersion and droplet growth in matrix and 2) residual oil displacement and mobilization in both matrix and fracture.

- The higher salinity gradient (*i.e.* high salinity brine of 20wt% NaCl) gave increased water dispersions -and droplet growth in matrix by osmotic diffusion and water film-flow between the high and low salinity phases. However, sensitivity to oil compositions of higher carbon number reduced the growth effect (*i.e.* n-Heptane). The lowest salinity gradient (*i.e.* high salinity brine of 5wt% NaCl) gave increased movement of interfaces, displacement and oil mobilization to fracture by water film-flow. Less sensitivity to oil composition was observed, but the processes occurred more frequently in less viscous oil (*i.e.* n-Hexane).

- The second set of tests with Ekofisk crude oil showed both diffusive water film-flow and osmotic diffusion through a continuous oil membrane and residual oil membrane respectively. Oil was mobilized and produced to fracture and fluids were re-distributed in matrix of the continuous crude oil system, while oil expansion and consequently displacement was observed through the residual oil membrane.

10.2 Miscible CO_2 Injection in Tight Shales

- Permeability estimates by Darcy's law for compressible fluids, under the discussed and provided assumptions for gas flow in shale, provided absolute permeability values in the 10^{-2}µD-range for the tight shale samples. The maximum average permeability was calculated to 0.023±2E-4 µD for shale 3i, 0.0079±4E-5 µD for shale 4i, and 0.0033±3E-5µD for 12iA. Correlating permeability values for the presented shale samples to structural CT-scans favoured structural laminations for increased flow capacity and lower flow in structures with high-density zones and tight textured matrixes.

- Two independent estimates of recovery were performed to quantify oil production 1) mass balance and 2) volumetric production during miscible CO_2 injection. Oil recovery by mass balance proved to be the better method based directly on change in sample weight before and after miscible CO_2 injection.

- Oil recovery by mass balance yielded high recovery factors from 76% to 114%OOIP. Recovery exceeded 100%OOIP for the n-Decane experiments because of additional production of immobile residual crude oil. Errors associated with density of the produced fluids and the porosity estimate of the cores provide basis for large experimental uncertainties. Volumetric production exhibited a greater range of recovery from 19.4%OOIP by crude oil to 103.3%OOIP by n-Decane production. The overall recovery was less compared to mass balance results because of large uncertainties relating to visualization of the small oil volumes produced (≤ 2.00ml).

- Fundamental CO_2 injections in n-Decane tests show high recovery by both mass balance (from 96% to 114%OOIP) and volumetric production (from 71.2% to 103.3%OOIP) due to system pressures above MMP for n-Decane. Crude oil recovery show great differences between mass balance (from 75% to 103%OOIP) and volumetric production (from 19.4% to 32%OOIP) due to variable MMPs for heavy crude oil components.

- Miscibility by molecular diffusion is an effective recovery mechanism by CO_2 injection during both first-contact experiments with n-Decane and multiple-contact experiments with crude oil in shale. This conclusion is based on mass balance values. The effect of molecular diffusion is especially important for enhanced recovery if an unfavourable mobility ratio causes early gas breakthrough.

- Experiments performed were influenced by experimental uncertainties related to fluid density, rock porosity, precipitation of crude components and low solution gas drives, during miscible CO_2 injection. The difference between mass balance and volumetric production is a result of precipitation of heavier components from the miscible phases in the downstream system when pressure sinks below individual MMPs. Improvements were made by adjusting the setup to shorter lengths of tubing and by adding a more effective cooling system.

11 Future Work

The following future work should be considered based on the presented results by LSW in sandstone micromodels and miscible CO_2 injection in shale:

11.1 Low Salinity Waterflooding

- The effect of elevated temperature on osmotic diffusion in brine/oil -systems by LSW should be studied for increased water flux through the semi-permeable oil membrane. When increasing temperature, the viscosity of the oil membrane will be reduced leading to improved mobility of water dispersions and droplet growth, especially important with high viscosity crude oils. An interesting observation would be if the transport mechanisms reported here would cause increased oil expansion and mobilization in systems more equal to reservoir conditions. Direct changes in matrix saturation and quantities of mobilized oil could be evaluated.

- Osmotic effects and water diffusion by LSW should be documented in shorter time frames to examine fluid-fluid interactions more accurately. This will assist in describing the abrupt changes of oil displacement and mobilization in more detail.

- By aging crude oil in micromodels and establishing a mixed-wet to oil-wet surface preference, the LSE of wettability alterations can be investigated relative to osmotic diffusion making an attempt to verify the LSE of Tang and Morrow (1997), Lager *et al.* (2006) and Ligthelm *et al.* (2009) and determine contribution.

- Low salinity brine with some degree of salinity should be considered to investigate the effect on osmotic behavior.

- The diffusion constant, D, for the low salinity water through various oil membranes should be calculated to quantify the extent of osmotic diffusion.

11.2 Miscible CO_2 Injection

- Quantification of oil recovery by miscible CO_2 injection in tight shales should continue in the re-designed laboratory setup to obtain better correlation between the mass balance and volumetric quantities of produced oil. Especially important will be to document the injected PVs CO_2 required to reach maximal oil recovery. The quantities of CO_2 required could be a factor when deciding on continuous miscible CO_2 injection for EOR in tight shale reservoirs.

- To develop better miscibility between injected CO_2 and crude oil, longer cores should be considered compared to the 1.5" cores applied in this thesis. Longer cores will give larger volumes for developing multiple-contact miscibility before breakthrough occurs. Using for example stacked cores will lead to improved miscibility. Research is currently ongoing at the Dept. of Physics and Technology.

- Based on experimental observations (valve leakage), molecular diffusion will to a degree establish miscibility before continuous CO_2 injection. The effect of shut-in periods prior to continuous CO_2 injection should be investigated for CO_2 in direct contact with crude saturation. The amount of PVs CO_2 needed to reach maximum recovery could be determined. Such a system might be more feasible in the field than one with direct continuous CO_2 injection.

- More accurate ways of determining gas permeability in shale should be considered. By CO_2 injection better values can be obtained by correcting for gas compressibility. In addition, the Forchheimer equation can be applied to correct for inertia effects, assuming that the small cross-sectional area of the shale pores induce larger local rates than what is recognized by the CO_2 injection rate.

- Other gases such as CH_4 or N_2 can be applied to determine permeability based on their affinity to the pore space distribution in shale. Results with re-assessed permeability values can be compared to the values for shale flow capacity presented here.

- To investigating the effect of molecular diffusion by miscible CO_2 injection, both liquid and supercritical CO_2 can be applied for both first-contact and multiple-contact miscibility through micromodel visualization. Visualization may reveal the effect of precipitation of heavy components as system pressures drop below individual MMPs for the miscible phase.

12 References

Ahmed, A. N. (2013). *En eksperimentell studie av CO2 injeksjon for økt oljeutvinning i oppsprukket kalk.* Master oppgave i reservoarfysikk: Institutt for fysikk og teknologi, Universitetet i Bergen.

Ahmed, T. (2006). *Reservoir Engineering .* Gulf Professional Publishing: Elsevier Inc.

Alvarado, V., & Manrique, E. (2010). *Enhanced Oil Recovery: Field Planning and Development Strategies.* Gulf Professional Publishing.

Austad, T., RezaeiDoust, A., & Puntervold, T. (2010). *Chemical Mechanism of Low Salinity Water Flooding in Sandstone Reservoirs.* SPE 129767: Society of Petroleum Engineers.

Basak, P. (1977). Non-Darcy Flow and its Implications to Seepage Problems. *Journal of the Irrigation and Drainage Division, Vol. 3, Issue 4* , 459-473.

Berg, J. C. (2010). *An Introduction to Interfaces and Colloids, The Bridge to Nanoscience.* World Scientific Publishing Co. Pte. Ltd.

Bjørlykke, K., & Jahren, J. (2010). Sandstones and Sandstone Reservoirs. In K. Bjørlykke, *Petroleum Geoscience: From Sedimentary Environments to Rock Physics* (pp. 113-140). Springer.

Bodi, T. (2012). Gas Flow in the Nano Size Pore Channels of Tight and Non Conventional Gas Storage Formations. In *Geosciences and Engineering, Vol 1, No. 1* (pp. 49-63). Geosciences and Engineering.

Boussour, S., Cissokho, M., Cordier, P., Bertin, H., & Hamon, G. (2009). *Oil Recovery by Low Salinity Brine Injection: Laboratory Results on Outcrop and Reservoir Cores.* SPE 124277: Society of Petroleum Engineers.

Brattekås, B. (2014). *Conformance Control for Enhanced Oil Recovery in Fractured Reservoirs.* Ph.D. Thesis: University of Bergen.

Buchgraber, M., Castanier, L. M., & Kovscek, A. R. (2012). *Microvisual Investigation of Foam Flow in Ideal Fractures: Role of Fracture Aperture and Surface Roughness.* SPE 159430: Society of Petroleum Engineers.

Bø, K. (2014). *Mobilty Control for CO2 EOR in Heterogeneous Reservoirs.* Master Thesis: Department of Physics and Technology, University of Bergen.

Campbell, B. T., & Orr, F. M. (1985). Flow Visualization for CO2 / Crude Oil Displacements. *SPE Journal October 1985* , 665-678.

Chang, R. (2008). *General Chemistry, The Essential Concepts, 5th Edition.* McGraw-Hill Companies Inc.

Chatzis, I., Morrow, N. R., & Lim, H. T. (1983). Magnitude and Detailed Structure of Residual Oil Saturation. *SPE Journal* , 311-336.

Chen, C., Balhoff, M., & Mohanty, K. K. (2014). *Effect of Heterogeneity on Primary Recovery and CO2 Huff 'n 'Puff Recovery in Shale-Oil Reservoirs.* SPE 164553: Society of Petroleum Engineers.

Crawford, P. M., Biglarbigi, K., & Dammer, A. R. (2008). *Advances in World Oil Shale Production Techniques.* Denver: SPE 116570, Society of Petroleum Engineers.

Cui, X., Bustin, A. M., & Bustin, R. M. (2009). Measurements of Gas Permeability and Diffusivity of Tight Reservoir Rocks: Different Approaches and Their Applications. *Geofluids, Vol 9, Issue 3* , 208-223.

Curtis, M. E., Goergen, E. T., Jemigen, J. D., Sondergeld, C. H., & Rai, C. S. (2014). *High-Resolution Mapping of the Distribution and Connectivity of Organic matter in Shales.* SPE 170787 MS: Society of Petroleum Engineers.

da Silva, F. V., & Belery, P. (1989). *Molecular Diffusion in Naturally Fractured Reservoirs: A Decisive Recovey Mechanism.* SPE 19672: Society of Petroleum Engineers.

Delgado, J. P. (2007). Longitudal and Transverse Dispersion in Porous Media. *TRANS ICHEMI, Vol.85 (A9)* , pp. 1245-1252.

Dong, C., & Hoffman, B. T. (2013). *Modeling Gas Injection into Shale Oil Reservoirs in the Sanish Field, North Dakota.* SPE 168827: Society of Petroleum Engineers.

Eide, Ø., Fernø, M. A., & Graue, A. (2013). *Visualization of CO2 EOR by Diffusion in Fractured Chalk.* SPE 170920 MS: Society of Petroleum Engineers.

Ellila, G. (2012). *Cappilary Forces and Osmotic Gradients in Salt Water-Oil Systems.* M.Sc Thesis: NTNU, Trondheim, Norway.

Emadi, A., & Sohrabi, M. (2013). *Visual Investigation of Oil Recovery by Low salinity Water Injection: Formation of Water Micro-Dispersions and Wettability Alterations.* Centre for Enhanced Oil Recovery and CO2 Solutions: Institute of Petroleum.

Enick, R. M., Olsen, D., Ammer, J., & Schuller, W. (2012). *Mobility and Conformance Control for CO2 EOR via Thickeners, Foams, and Gels - A Literature Review of 40 Years of Research and Pilot Tests.* SPE 154122: Society of Petroleum Engineers.

Fakcharoenphol, P., Kurtoglu, B., Kazemi, H., Charoenwongsa, S., & Yu-Shu, W. (2014). *The Effect of Osmotic Pressure on Improved Oil Recovery from Fractured Shale Formations.* SPE 198998 MS: Society of Petroleum Engineers.

Farouq, S. M., & Thomas, S. (1989). *The Promise and Problems of Enhanced Oil Recovery Methods.* Regina: Petroleum Society of CIM.

Fernø, M. (2012). *Enhanced Oil Recovery in Fractured Reservoirs.* Retrieved from Introduction to Enhanced Oil Recovery (EOR) Processes and Bioremediation of Oil-Contaminated Sites, Dr. Laura Romero-Zeròn (Ed.), ISBN: 978-953-51-0629-6, InTech, Available from: http://www.intechopen.com/books/introduction-to-enhanced-oil-recovery-eor-processes-and-bioremediation-of-oil-contaminated-sites/enhanced-oil-recovery-in-fractured-reservoirs

Follesø, H. N. (2012). *Fluid Displacements during Multiphase Flow Visualized at the Pore Scale using Micromodels.* Master Thesis: University of Bergen.

Gamadi, T. D., Sheng, J. J., Soliman, M. Y., Menouar, H., Watson, M. C., & Emadibaladehi, H. (2014). *An Experimental Study of Cyclic CO2 Injection to Improve Shale Oil Recovery.* SPE 169142 MS: Society of Petroleum Engineers.

Gauteplass, J., Follesø, H. N., Graue, A., Kovscek, A. R., & Fernø, M. A. (2013). *Visualization of Pore-level Displacement Mechanisms During CO2 Injection and EOR Processes.* IOR 2013 - 17th European Symposium on Improved Oil Recovery, St. Petersburg, Russia: European Association of Geoscientists and Engineers (EAGE).

Ghorayeb, K., & Firoozabadi, A. (2001). Features of Convection and Diffusion in Porous Media for Binary Systems. *Journal of Canadian Petroleum Volume 40, No. 2* , 21-28.

Graue, A., Fernø, M. A., Fredriksen, S., Lysne, M., & Rognmo, A. U. (2014). *EOR in Tight Rocks.* Progress report : Dept. of Physics and Technology, University of Bergen, Norway.

Graue, A., Viksund, B. G., & Baldwin, B. A. (1999). Reproducable Wettability Alteration of Low-Permeable Outcrop Chalk. *SPE Reservoir Evaluation & Engineering, Vol 2, Issue 2* , 134-140.

Hart, J., Guymer, I., Jones, A., & Stovin, V. (2012). *Longitudal Dispersion Coefficients within Turbulent and Transitional Pipe Flow.* Poland, Export Citation BibTeX: University of Warwick.

Haugen, Å., Mani, N., Svenningsen, S., Brattekås, B., Graue, A., Ersland, G., et al. (2014). Miscible and Immiscible Foam Injection for Mobility Control and EOR in Fractured Oil-Wet Carbonate Rocks. *Transport in Porous Media, Vol 104, No. 1* , 109-131.

Heller, R., & Zoback, M. (2013). *Laboratory Measurements of Matrix Permeability and Slippage Enhanced Permeability in Gas Shales.* SPE 168856: Society of Petroleum Engineers.

Hornbrook, J. W., Castanier, L. M., & Pettit, P. A. (1991). *Observation of Foam/Oil Interactions in a New High-Resolution Micromodel.* SPE 22631: Society of Petroleum Engineers.

Huang, H., & Ayoub, J. (2008). *Applicability of the Forchheimer Equation for Non-Darcy Flow in Porous Media.* SPE 102715: Society of Petroleum Engineers.

Høgnesen, E. J., Strand, S., & Austad, T. (2005). *Waterflooding of Preferential Oil-Wet Carbonates: Oil Recovery Related to Reservoir Temperature and Brine Composition.* SPE 94166: Society of Petroleum Engineers.

Høyland, M. D. (2014). *Measurements and visualization of hydrate growth in porous media.* Master Thesis: Department of Physics and Technology, University of Bergen.

IEA. (2013). Redrawing the Energy Climate Map. *World Energy Outlook Special Report 2013* , 28.

Iglauer, S. (2011). *Dissolution Trapping of Carbon Dioxide in Reservoir Formation Brine - A Carbon Storage Mechanism.* Retrieved from Mass Transfer - Advanced Aspects, Dr. Hironori Nakajima (Ed.), ISBN: 978-953-307-636-2, Intech, Available from: http://www.intechopen.com/books/mass-transfer-advanced-aspects/dissolution-trapping-of-carbon-dioxide-in-reservoir-formation-brine-a-carbon-storage-mechanism

Ketcham, R. A., & Carlson, W. D. (2001). Acquistion, optimization and interpretation of X-ray computed tomography imagery: applications to the geosciences. In *Computers & Geosciences* (pp. 381-400). Elsevier Science Ltd.

Kovscek, A. R., Tang, G. Q., & Vega, B. (2008). *Experimental Investigation of Oil Recovery from Siliceous Shale by CO2 Injection.* SPE 115679: Society of Petroleum Engineers.

Kuila, U., & Prasad, M. (2013). Specific Surface Area and Pore-Size Distribution in Clays and Shales. In *Geophysical Prospecting: Rock Physics for Reservoir Exploration, Characterisation and Monitoring, Vol 61, Issue 2* (pp. 341-362). European Association of Geoscientists & Engineers (EAGE).

Lager, A., Webb, K. J., Black, C. J., Singleton, M., & Sorbie, K. S. (2006). *Low Salinity Oil Recovery - An Experimental Investigation.* International Symposium in Trondheim, Norway, SCA2006-36: Society of Core Analysts.

Lager, A., Webb, K. J., Collins, I. R., & Richmond, D. M. (2008). *LoSal Enhanced Oil Recovery: Evidence of Enhanced Oil Recovery at the Reservoir Scale.* SPE 113976 MS: Society of Petroleum Engineers.

Lake, L. W. (1989). *Enhanced Oil Recovery.* Englewood Cliffs, New Jersey: Prentice Hall Incorporated.

Lambert, M. R., Marino, S. D., Anthony, T. L., Calvin, M. W., Gutierrez, S., & Smith, D. P. (1996). *Implementing CO2 Floods: No More Delays!* SPE 35187: Society of Petroleum Engineers.

Latil, M. (1980). *Enhanced Oil Recovery.* Paris: Editions Technip .

Ligthelm, D. J., Gronsveld, J., Hofman, J. P., Brussee, N. J., Marcelis, F., & van der Linde, H. A. (2009). *Novel Waterflooding Statgey by Manipulation of Injection Brine Composition.* SPE 119835: Society of Petroleum Engineers.

Melzer, L. S. (2012). *Carbon Dioxide Enhanced Oil Recovery (CO2 EOR): Factors Involved in Adding Carbon Capture, Utilization and Storage (CCUS) to Enhanced Oil Recovery.* Texas, USA.

Morrow, N., & Buckley, J. (2011). *Improved Oil Recovery by Low-Salinity Waterflooding.* SPE 129421: Society of Petroleum Engineers.

Morsy, S., Sheng, J. J., & Soliman, M. Y. (2013). *Improving Hydraulic Fracturing of Shale Formations by Acidizing.* SPE 165688: Society of Petroleum Engineers.

Nelson, P. H. Pore-throat sizes in sandstones, tight sandstones, and shales. In *AAPG Bulletin, V. 93, No. 3 (March 2009)* (pp. 329 - 340). The American Association of Petroleum Geologists.

NIST. (2011). *The National Institute of Standards and Technology Chemistry WebBook*. Retrieved 08 28, 2014, from http://webbook.nist.gov/chemistry/

NPD. (2014). Storage Options with EOR. *Compiled CO2 Storage Atlas for the Norwegian Continental Shelf* , Chapter 8.

Opdal, I. O. (2014). *Mobility Control by CO2-foam Injection for Integrated EOR.* Master Thesis: Department of Physics and Technology, University of Bergen.

Orangi, A., Nagarajan, N. R., Honarpour, M. M., & Rosenzweig, J. (2011). *Unconventional Shale and Gas-Condensate Reservoir Production, Impact of Rock, Fluid and Hydraulic Fractures.* SPE 140536: Society of Petroleum Engineers.

Perkins, T. K., & Johnston, O. C. (1963). *A Review of Diffusion and Dispersion in Porous Media.* SPE 480: Society of Petroleum Engineers.

Picha, M. S. (2007). *Enhanced Oil Recovery by Hot CO2 Flooding.* SPE 105425: Society of Petroleum Engineers.

Rangel-German, E. R., & Kovscek, A. R. (2006). A Micromodel Investigation of Two-phase Mixture-fracture Transfer Mechanisms. *Water Resources Research, Vol. 42, W03401.* The American Geophysical Union.

RezaeiDoust, A., Puntervold, T., Strand, S., & Austad, T. (2009). Smart Water as Wettability Modifier in Carbonate and Sandstone: A Discussion of Similarities/Differences in the Chemical Mechanisms. *Energy Fuels 2009, 23 (9)* , 4479-4485.

Romanuka, J., Hofman, J. P., Ligthelm, D. J., Suijkerbuijk, B. J., Marcelis, A. M., Oedai, S., et al. (2012). *Low Salinity EOR in Carbonates.* SPE 153869: Society of Petroleum Engineers.

Sanaei, A., Jamili, A., & Callard, J. (2014). *Effects of non-Darcy Flow and Pore Proximety on Gas Condensate Production from Nanopore Unconventional Resources.* Retrieved from 5th International Conference on Porous Media and Their Applications in Science, Engineering and Industry, Eds. ECI Symposium Series, Volume (2014). See: http://dc.engconfintl.org/porous_media_V/33

Sandengen, K., & Arntzen, O. J. (2013). *Osmosis During Low Salinity Waterflooding.* IOR 2013 - 17th European Symposium on Improved Oil Recovery, St. Petersburg, Russia: European Association of Geologists and Engineers (EAGE).

Skarestad, M., & Skauge, A. (2012). *Fluid Properties and Recovery Methods.* Compendium, Reservoarteknikk II, PTEK 213: University of Bergen, Norway.

Skrettingland, K., Holt, T., Tweheyo, M. T., & Skjevrak, I. (2010). *Snorre Low Salinety Water Injection - Core Flooding Experiments and Single Well Field Pilot.* SPE 129877: Society of Petroleum Engineers.

Swami, V., Clarkson, C. R., & Settari, A. (. (2012). *Non Darcy Flow in Shale Nanopores: Do We Have the Final Answer.* SPE 162665: Society of Petroleum Engineers.

Tang, G. Q., & Morrow, N. R. (1999). Influence of Brine Composition and Fines Migration on Crude/Oil/Brine/Rock Interactions and Oil Recovery. *Journal of Petroleum Science and Engineering 24 (1999)* , 99-111.

Tang, G. Q., & Morrow, N. R. (1997). *Salinity, Temperature, Oil Composition, and Oil Recovery by Waterflooding.* SPE 36680 PA: Society of Petroleum Engineers.

Ahmed, A. N. (2013). *En eksperimentell studie av CO2 injeksjon for økt oljeutvinning i oppsprukket kalk.* Master oppgave i reservoarfysikk: Institutt for fysikk og teknologi, Universitetet i Bergen.

Ahmed, T. (2006). *Reservoir Engineering .* Gulf Professional Publishing: Elsevier Inc.

Alvarado, V., & Manrique, E. (2010). *Enhanced Oil Recovery: Field Planning and Development Strategies.* Gulf Professional Publishing.

Austad, T., RezaeiDoust, A., & Puntervold, T. (2010). *Chemical Mechanism of Low Salinity Water Flooding in Sandstone Reservoirs.* SPE 129767: Society of Petroleum Engineers.

Basak, P. (1977). Non-Darcy Flow and its Implications to Seepage Problems. *Journal of the Irrigation and Drainage Division, Vol. 3, Issue 4* , 459-473.

Berg, J. C. (2010). *An Introduction to Interfaces and Colloids, The Bridge to Nanoscience.* World Scientific Publishing Co. Pte. Ltd.

Bjørlykke, K., & Jahren, J. (2010). Sandstones and Sandstone Reservoirs. In K. Bjørlykke, *Petroleum Geoscience: From Sedimentary Environments to Rock Physics* (pp. 113-140). Springer.

Bodi, T. (2012). Gas Flow in the Nano Size Pore Channels of Tight and Non Conventional Gas Storage Formations. In *Geosciences and Engineering, Vol 1, No. 1* (pp. 49-63). Geosciences and Engineering.

Boussour, S., Cissokho, M., Cordier, P., Bertin, H., & Hamon, G. (2009). *Oil Recovery by Low Salinity Brine Injection: Laboratory Results on Outcrop and Reservoir Cores.* SPE 124277: Society of Petroleum Engineers.

Brattekås, B. (2014). *Conformance Control for Enhanced Oil Recovery in Fractured Reservoirs.* Ph.D. Thesis: University of Bergen.

Buchgraber, M., Castanier, L. M., & Kovscek, A. R. (2012). *Microvisual Investigation of Foam Flow in Ideal Fractures: Role of Fracture Aperture and Surface Roughness.* SPE 159430: Society of Petroleum Engineers.

Bø, K. (2014). *Mobilty Control for CO2 EOR in Heterogeneous Reservoirs.* Master Thesis: Department of Physics and Technology, University of Bergen.

Campbell, B. T., & Orr, F. M. (1985). Flow Visualization for CO2 / Crude Oil Displacements. *SPE Journal October 1985* , 665-678.

Chang, R. (2008). *General Chemistry, The Essential Concepts, 5th Edition.* McGraw-Hill Companies Inc.

Chatzis, I., Morrow, N. R., & Lim, H. T. (1983). Magnitude and Detailed Structure of Residual Oil Saturation. *SPE Journal* , 311-336.

Chen, C., Balhoff, M., & Mohanty, K. K. (2014). *Effect of Heterogeneity on Primary Recovery and CO2 Huff 'n 'Puff Recovery in Shale-Oil Reservoirs.* SPE 164553: Society of Petroleum Engineers.

Crawford, P. M., Biglarbigi, K., & Dammer, A. R. (2008). *Advances in World Oil Shale Production Techniques.* Denver: SPE 116570, Society of Petroleum Engineers.

Cui, X., Bustin, A. M., & Bustin, R. M. (2009). Measurements of Gas Permeability and Diffusivity of Tight Reservoir Rocks: Different Approaches and Their Applications. *Geofluids, Vol 9, Issue 3* , 208-223.

Curtis, M. E., Goergen, E. T., Jemigen, J. D., Sondergeld, C. H., & Rai, C. S. (2014). *High-Resolution Mapping of the Distribution and Connectivity of Organic matter in Shales.* SPE 170787 MS: Society of Petroleum Engineers.

da Silva, F. V., & Belery, P. (1989). *Molecular Diffusion in Naturally Fractured Reservoirs: A Decisive Recovey Mechanism.* SPE 19672: Society of Petroleum Engineers.

Delgado, J. P. (2007). Longitudal and Transverse Dispersion in Porous Media. *TRANS ICHEMI, Vol.85 (A9)* , pp. 1245-1252.

Dong, C., & Hoffman, B. T. (2013). *Modeling Gas Injection into Shale Oil Reservoirs in the Sanish Field, North Dakota.* SPE 168827: Society of Petroleum Engineers.

Eide, Ø., Fernø, M. A., & Graue, A. (2013). *Visualization of CO2 EOR by Diffusion in Fractured Chalk.* SPE 170920 MS: Society of Petroleum Engineers.

Ellila, G. (2012). *Cappilary Forces and Osmotic Gradients in Salt Water-Oil Systems.* M.Sc Thesis: NTNU, Trondheim, Norway.

Emadi, A., & Sohrabi, M. (2013). *Visual Investigation of Oil Recovery by Low salinity Water Injection: Formation of Water Micro-Dispersions and Wettability Alterations.* Centre for Enhanced Oil Recovery and CO2 Solutions: Institute of Petroleum.

Enick, R. M., Olsen, D., Ammer, J., & Schuller, W. (2012). *Mobility and Conformance Control for CO2 EOR via Thickeners, Foams, and Gels - A Literature Review of 40 Years of Research and Pilot Tests.* SPE 154122: Society of Petroleum Engineers.

Fakcharoenphol, P., Kurtoglu, B., Kazemi, H., Charoenwongsa, S., & Yu-Shu, W. (2014). *The Effect of Osmotic Pressure on Improved Oil Recovery from Fractured Shale Formations.* SPE 198998 MS: Society of Petroleum Engineers.

Farouq, S. M., & Thomas, S. (1989). *The Promise and Problems of Enhanced Oil Recovery Methods.* Regina: Petroleum Society of CIM.

Fernø, M. (2012). *Enhanced Oil Recovery in Fractured Reservoirs.* Retrieved from Introduction to Enhanced Oil Recovery (EOR) Processes and Bioremediation of Oil-Contaminated Sites, Dr. Laura Romero-Zeròn (Ed.), ISBN: 978-953-51-0629-6, InTech, Available from: http://www.intechopen.com/books/introduction-to-enhanced-oil-recovery-eor-processes-and-bioremediation-of-oil-contaminated-sites/enhanced-oil-recovery-in-fractured-reservoirs

Follesø, H. N. (2012). *Fluid Displacements during Multiphase Flow Visualized at the Pore Scale using Micromodels.* Master Thesis: University of Bergen.

Gamadi, T. D., Sheng, J. J., Soliman, M. Y., Menouar, H., Watson, M. C., & Emadibaladehi, H. (2014). *An Experimental Study of Cyclic CO2 Injection to Improve Shale Oil Recovery.* SPE 169142 MS: Society of Petroleum Engineers.

Gauteplass, J., Follesø, H. N., Graue, A., Kovscek, A. R., & Fernø, M. A. (2013). *Visualization of Pore-level Displacement Mechanisms During CO2 Injection and EOR Processes.* IOR 2013 - 17th European Symposium on Improved Oil Recovery, St. Petersburg, Russia: European Association of Geoscientists and Engineers (EAGE).

Ghorayeb, K., & Firoozabadi, A. (2001). Features of Convection and Diffusion in Porous Media for Binary Systems. *Journal of Canadian Petroleum Volume 40, No. 2* , 21-28.

Graue, A., Fernø, M. A., Fredriksen, S., Lysne, M., & Rognmo, A. U. (2014). *EOR in Tight Rocks.* Progress report : Dept. of Physics and Technology, University of Bergen, Norway.

Graue, A., Viksund, B. G., & Baldwin, B. A. (1999). Reproducable Wettability Alteration of Low-Permeable Outcrop Chalk. *SPE Reservoir Evaluation & Engineering, Vol 2, Issue 2* , 134-140.

Hart, J., Guymer, I., Jones, A., & Stovin, V. (2012). *Longitudal Dispersion Coefficients within Turbulent and Transitional Pipe Flow.* Poland, Export Citation BibTeX: University of Warwick.

Haugen, Å., Mani, N., Svenningsen, S., Brattekås, B., Graue, A., Ersland, G., et al. (2014). Miscible and Immiscible Foam Injection for Mobility Control and EOR in Fractured Oil-Wet Carbonate Rocks. *Transport in Porous Media, Vol 104, No. 1* , 109-131.

Heller, R., & Zoback, M. (2013). *Laboratory Measurements of Matrix Permeability and Slippage Enhanced Permeability in Gas Shales.* SPE 168856: Society of Petroleum Engineers.

Hornbrook, J. W., Castanier, L. M., & Pettit, P. A. (1991). *Observation of Foam/Oil Interactions in a New High-Resolution Micromodel.* SPE 22631: Society of Petroleum Engineers.

Huang, H., & Ayoub, J. (2008). *Applicability of the Forchheimer Equation for Non-Darcy Flow in Porous Media.* SPE 102715: Society of Petroleum Engineers.

Høgnesen, E. J., Strand, S., & Austad, T. (2005). *Waterflooding of Preferential Oil-Wet Carbonates: Oil Recovery Related to Reservoir Temperature and Brine Composition.* SPE 94166: Society of Petroleum Engineers.

Høyland, M. D. (2014). *Measurements and visualization of hydrate growth in porous media.* Master Thesis: Department of Physics and Technology, University of Bergen.

IEA. (2013). Redrawing the Energy Climate Map. *World Energy Outlook Special Report 2013* , 28.

Iglauer, S. (2011). *Dissolution Trapping of Carbon Dioxide in Reservoir Formation Brine - A Carbon Storage Mechanism.* Retrieved from Mass Transfer - Advanced Aspects, Dr. Hironori Nakajima (Ed.), ISBN: 978-953-307-636-2, Intech, Available from: http://www.intechopen.com/books/mass-transfer-advanced-aspects/dissolution-trapping-of-carbon-dioxide-in-reservoir-formation-brine-a-carbon-storage-mechanism

Ketcham, R. A., & Carlson, W. D. (2001). Acquistion, optimization and interpretation of X-ray computed tomography imagery: applications to the geosciences. In *Computers & Geosciences* (pp. 381-400). Elsevier Science Ltd.

Kovscek, A. R., Tang, G. Q., & Vega, B. (2008). *Experimental Investigation of Oil Recovery from Siliceous Shale by CO2 Injection.* SPE 115679: Society of Petroleum Engineers.

Kuila, U., & Prasad, M. (2013). Specific Surface Area and Pore-Size Distribution in Clays and Shales. In *Geophysical Prospecting: Rock Physics for Reservoir Exploration, Characterisation and Monitoring, Vol 61, Issue 2* (pp. 341-362). European Association of Geoscientists & Engineers (EAGE).

Lager, A., Webb, K. J., Black, C. J., Singleton, M., & Sorbie, K. S. (2006). *Low Salinity Oil Recovery - An Experimental Investigation.* International Symposium in Trondheim, Norway, SCA2006-36: Society of Core Analysts.

Lager, A., Webb, K. J., Collins, I. R., & Richmond, D. M. (2008). *LoSal Enhanced Oil Recovery: Evidence of Enhanced Oil Recovery at the Reservoir Scale.* SPE 113976 MS: Society of Petroleum Engineers.

Lake, L. W. (1989). *Enhanced Oil Recovery.* Englewood Cliffs, New Jersey: Prentice Hall Incorporated.

Lambert, M. R., Marino, S. D., Anthony, T. L., Calvin, M. W., Gutierrez, S., & Smith, D. P. (1996). *Implementing CO2 Floods: No More Delays!* SPE 35187: Society of Petroleum Engineers.

Latil, M. (1980). *Enhanced Oil Recovery.* Paris: Editions Technip .

Lie, S. H. (2013). *Diffusion as an Oil Recovery Mechanism During CO2 Injection in Fractured Reservoirs.* Master thesis: Department of Physics and Technology, University of Bergen.

Ligthelm, D. J., Gronsveld, J., Hofman, J. P., Brussee, N. J., Marcelis, F., & van der Linde, H. A. (2009). *Novel Waterflooding Stategy by Manipulation of Injection Brine Composition.* SPE 119835: Society of Petroleum Engineers.

Melzer, L. S. (2012). *Carbon Dioxide Enhanced Oil Recovery (CO2 EOR): Factors Involved in Adding Carbon Capture, Utilization and Storage (CCUS) to Enhanced Oil Recovery.* Texas, USA.

Morrow, N., & Buckley, J. (2011). *Improved Oil Recovery by Low-Salinity Waterflooding.* SPE 129421: Society of Petroleum Engineers.

Morsy, S., Sheng, J. J., & Soliman, M. Y. (2013). *Improving Hydraulic Fracturing of Shale Formations by Acidizing.* SPE 165688: Society of Petroleum Engineers.

Nelson, P. H. Pore-throat sizes in sandstones, tight sandstones, and shales. In *AAPG Bulletin, V. 93, No. 3 (March 2009)* (pp. 329 - 340). The American Association of Petroleum Geologists.

NIST. (2011). *The National Institute of Standards and Technology Chemistry WebBook*. Retrieved 08 28, 2014, from http://webbook.nist.gov/chemistry/

NPD. (2014). Storage Options with EOR. *Compiled CO2 Storage Atlas for the Norwegian Continental Shelf* , Chapter 8.

Opdal, I. O. (2014). *Mobility Control by CO2-foam Injection for Integrated EOR.* Master Thesis: Department of Physics and Technology, University of Bergen.

Orangi, A., Nagarajan, N. R., Honarpour, M. M., & Rosenzweig, J. (2011). *Unconventional Shale and Gas-Condensate Reservoir Production, Impact of Rock, Fluid and Hydraulic Fractures.* SPE 140536: Society of Petroleum Engineers.

Perkins, T. K., & Johnston, O. C. (1963). *A Review of Diffusion and Dispersion in Porous Media.* SPE 480: Society of Petroleum Engineers.

Picha, M. S. (2007). *Enhanced Oil Recovery by Hot CO2 Flooding.* SPE 105425: Society of Petroleum Engineers.

Rangel-German, E. R., & Kovscek, A. R. (2006). A Micromodel Investigation of Two-phase Mixture-fracture Transfer Mechanisms. *Water Resources Research, Vol. 42, W03401.* The American Geophysical Union.

RezaeiDoust, A., Puntervold, T., Strand, S., & Austad, T. (2009). Smart Water as Wettability Modifier in Carbonate and Sandstone: A Discussion of Similarities/Differences in the Chemical Mechanisms. *Energy Fuels 2009, 23 (9)* , 4479-4485.

Romanuka, J., Hofman, J. P., Ligthelm, D. J., Suijkerbuijk, B. J., Marcelis, A. M., Oedai, S., et al. (2012). *Low Salinity EOR in Carbonates.* SPE 153869: Society of Petroleum Engineers.

Sanaei, A., Jamili, A., & Callard, J. (2014). *Effects of non-Darcy Flow and Pore Proximety on Gas Condensate Production from Nanopore Unconventional Resources.* Retrieved from 5th International Conference on Porous Media and Their Applications in Science, Engineering and Industry, Eds. ECI Symposium Series, Volume (2014). See: http://dc.engconfintl.org/porous_media_V/33

Sandengen, K., & Arntzen, O. J. (2013). *Osmosis During Low Salinity Waterflooding.* IOR 2013 - 17th European Symposium on Improved Oil Recovery, St. Petersburg, Russia: European Association of Geologists and Engineers (EAGE).

Skarestad, M., & Skauge, A. (2012). *Fluid Properties and Recovery Methods.* Compendium, Reservoarteknikk II, PTEK 213: University of Bergen, Norway.

Skrettingland, K., Holt, T., Tweheyo, M. T., & Skjevrak, I. (2010). *Snorre Low Salinety Water Injection - Core Flooding Experiments and Single Well Field Pilot.* SPE 129877: Society of Petroleum Engineers.

Swami, V., Clarkson, C. R., & Settari, A. (. (2012). *Non Darcy Flow in Shale Nanopores: Do We Have the Final Answer.* SPE 162665: Society of Petroleum Engineers.

Tang, G. Q., & Morrow, N. R. (1999). Influence of Brine Composition and Fines Migration on Crude/Oil/Brine/Rock Interactions and Oil Recovery. *Journal of Petroleum Science and Engineering 24 (1999)* , 99-111.

Tang, G. Q., & Morrow, N. R. (1997). *Salinity, Temperature, Oil Composition, and Oil Recovery by Waterflooding.* SPE 36680 PA: Society of Petroleum Engineers.

Terry, R. E. (2001). Enhanced Oil Recovery. In R. A. Meyers, *Encyclopedia of Physical Science and Technology 3rd Edition, Vol. 18* (pp. 503-518). Academic Press.

Tzimas, E., Georgakaki, C., Cortez, G., & Peteves, S. D. (2005). *Enchanced Oil Recovery using Carbon Dioxide in the European Energy System.* DG JRC Institute for Energy: Office for Official Publications of the European Communities.

Vega, B., Andrews, J. C., Liu, Y., Xradia, J. G., & Kovscek, A. (2013). *Nanoscale Visualization of Gas Shale Pore and Textural Features.* SPE 168825: Society of Petroleum Engineers.

Vega, B., O'Brien, W. J., & Kovscek, A. R. (2010). *Experimental Investigation of Oil Recovery From Siliceous Shale by Miscible CO2 Injection.* SPE 135627: Society of Petroleum Engineers.

Wasaki, A., & Akkutlu, Y. (2014). *Permeability of Organic-rich Shale.* SPE 170830 MS: Society of Petroleum Engineers.

Webb, K. J., Black, C. J., & Al-Ajeel, H. (2004). *Low Salinity Oil Recovery - Log-Inject-Log.* SPE 89379: Society of Petroleum Engineers.

Woody, F., Blunt, M., & Castanier, L. (1996). *Pore Level Visualization of Foam Flow in a Silicon Micromodel.* SUPRI TR 100: Stanford University.

Yellig, W. F., & Metcalfe, R. S. (1980). Determination and Prediction of CO2 Minimum Miscibility Pressures. *Journal of Petroleum Technology* , 160-171.

Zeng, Z., & Griegg, R. (2006). A Criterion for Non-Darcy Flow in Porous Media. *Transport in Porous Media, Vol 63, Issue 1* , 57-69.

Zitha, P., Felder, R., Zornes, D., Brown, K., & Mohanty, K. (2011). *Increasing Hydrocarbon Recovery Factors.* SPE Technology Updates: Society of Petroleum Engineers.

Zolotukhin, A. B., & Ursin, J. R. (2000). *Introduction to Petroleum Reservoir Engineering.* Kristiansand: Høyskoleforlaget AS - Norwegian Academic Press.

Appendix A – Uncertainty Estimation

A calculated measurement e.g. y is generally a function of different measures $x_1, x_2, x_3, \dots, x_i$ with related uncertainties $S_{x_1}, S_{x_2}, S_{x_3}, \dots, S_{x_i}$: $\qquad y = f(x_1, x_2, x_3, \dots, x_i)$.

Calculating uncertainty: Mean

Independent variables $x, y, z, \dots, i$ have arithmetical means $\bar{x}, \bar{y}, \bar{z}, \dots, \bar{\imath}$.
For a data set containing the measured values $x_1, x_2, x_3, \dots, x_N$ an arithmetic value $\bar{x}$ can be calculated by:

$$\bar{x} = \frac{x_1 + x_2 + x_3 + \dots + x_N}{N} = \frac{1}{N} \sum_{i=1}^{N} x_i \qquad (A1)$$

Where N is the number of values within the data set.

When calculating mean the uncertainty can be estimated using the max-min theorem. By the max-min theorem uncertainty $S_{\bar{x}}$ is calculated by:

$$S_{\bar{x}} \approx \frac{W_N}{\sqrt{N}} = \frac{x_{max} - x_{min}}{\sqrt{N}} \quad \text{for } 3 \leq N \leq 11 \qquad (A2)$$

Calculating uncertainty: Addition and subtraction

If a value R is calculated by either addition or subtraction of independent variables $x, y, z, \dots, i$, where each independent variable provides an additional uncertainty $S_x, S_y, S_z, \dots, S_{x_i}$ then the uncertainty for the calculated variable R, denoted S_R, can be calculated by:

$$S_R = \sqrt{\left(\frac{\delta R}{\delta x} S_x\right)^2 + \left(\frac{\delta R}{\delta y} S_y\right)^2 + \left(\frac{\delta R}{\delta z} S_z\right)^2 + \dots + \left(\frac{\delta R}{\delta i} S_i\right)^2} \qquad (A3)$$

This is the general form for calculating uncertainty related to addition and subtraction.

The above equation partially derived in respect to $x, y, z, \dots, i$ gives the simplified version:

$$S_R = \sqrt{(S_x)^2 + \left(S_y\right)^2 + (S_z)^2 + \dots + (S_i)^2} \qquad (A4)$$

This is the compiled form applied when calculating uncertainty in this thesis.

Calculating uncertainty: Quotient or product

If a value R is calculated as either a quotient or product of the independent variables $a^2 x, b^2 y, c^2 z, \dots, n^2 i$, given that $a^2, b^2, c^2, \dots, n^2$ are constants and $x, y, z, \dots, i$ are the independent variables, where each independent variable provides an additional uncertainty $S_x, S_y, S_z, \dots, S_i$ then the uncertainty for the calculated variable R, denoted S_R, can be calculated by:

$$\frac{S_R}{R} = \sqrt{\left(a \frac{S_x}{x}\right)^2 + \left(b \frac{S_y}{y}\right)^2 + \left(c \frac{S_z}{z}\right)^2 + \dots + \left(n \frac{S_i}{i}\right)^2} \qquad (A5)$$

Instrumental and Experimental Source of Errors

A total uncertainty estimate is generally caused by various errors. These can be either instrumental or experimental.

Instrumental uncertainties

Instrumental uncertainties are determined by the precision of the instrument in use. Errors related to instrumental uncertainties are random effects that occur in operating the instrument or in relation to how well the instrument is calibrated.

Table A1 - Instrumental uncertainties used in this thesis.

Parameter/instrument	Uncertainty
Caliper	$\pm 0.002 cm$
Pressure Transducers (ESI-USB)	$\pm 0.10\% \, FS \, (400 bar)$
Weight	$\pm 0.01 gr$
Injection rate accuracy (Quizix SP-5200)	0.20%
Pressure accuracy (Quizix QX-6K-SS)	± 0.83
Cumulative vol. inj. Accuracy (Quizix SP-5200)	0.20%
Production cylinder	$\pm 0.05 ml$

Experimental uncertainties

Experimental uncertainties are generally determined by errors that afflict experimental measures. One important experimental uncertainty is related to systematic errors that influence or produce consistent deviations in a set of measurements.

The following experimental uncertainties were observed in this thesis related to the miscible CO_2 injections in shale:
- Estimates of porosity affecting the value of 3D-oil saturation.
- Variation in density of the produced n-Decane during miscible CO_2 injection.
- The precipitation of heavy crude oil components from the miscible oil/CO_2 phase during oil production.
- Reduced solution-gas drive during crude oil production.

In this thesis, the above systematic errors are much larger than the instrumental uncertainties calculated. Hence, the instrumental uncertainties become overall insignificant in estimating measured values.

Assumptions

The effect of assumptions may also contribute to uncertainty. This is especially the case for the absolute permeability measurements performed on shale in this thesis were Darcy-flow, ideal gas behavior and effective end-point permeability of CO_2 were assumed. This type of uncertainty is not easy to recognise, and generally one has to determine the relative effect of the assumption, whether it increases, decreases or randomly affects the results presented.

Appendix B – Nomenclature

E	Reservoir displacement efficiency
E_D	Microscopic displacement efficiency
E_{vol}	Macroscopic displacement efficiency
E_A	Area sweep
E_V	Vertical sweep
N_c	Capillary number
i	Denoting displacing fluid
j	Denoting displaced fluid
v	Fluid rate (ml/s)
μ	Viscosity $(Pa \cdot s)$
σ	Interfacial tension
θ	Wetting angle
M	Mobility ratio
λ	Mobility of fluid
k_r	Relative permeability (D)
K_n	Knudsen number
K	Absolute permeability (D)
q	Injection rate (ml/h)
L	Length (m)
Δp	Differential pressure (Pa)
D	Darcy (unit for permeability)
Q_g	Gas flow rate (ml/h)
A	Cross-sectional area (m ^{2})
k_g	Gas permeability(D)
p	Pressure(Pa)
Q_e	Economic cut off rate
N_{pi}	Cumulative recovery
$N_{p,max}$	Maximum cumulative recovery
J	Flux of low salinity water (mol/s·m^2)
D_{AB}	Diffusion constant for" A" in "B" (m/s)
$\delta C_A/\delta x$	Concentration gradient for" A" across distance "x" (mol/m)
z	Diffusion distance (m)
u	Fluid velocity (ml/s)
S_o	Oil saturation
m_d	Dry weight (g)
m_s	Saturated weight (g)
V_b	Bulk volume (ml)
φ	Porosity core angle (%)
ρ_o	Density of oil (g/ml)
$\%wt$	Weight percent
K_e	Effective permeability (D)
K_{rg}	Gas relative permeability (D)
R_f	Recovery factor (%)

Appendix C – Abbreviations

OOIP   Original oil in place
EOR   Enhanced oil recovery
LSW   Low salinity waterflooding
LSE   Low salinity effect
UoB   University of Bergen
US   United States
OPEC   Organization of oil producing countries
PVT   Pressure, volume and temperature
IOR   Improved oil recovery
NPV   Net present value
EUR   Expected ultimate recovery
BP   British Petroleum
COBR   Crude-oil/brine/rock
MIE   Multi-component ion exchange
NCS   Norwegian continental shelf
CCS   Carbon capture and storage
WAG   Water alternating gas
MMP   Minimum miscibility pressure
SEM   Scanning electron microscopy
CT   Computed tomography
BFC   Boundary flow condition
DP   Diagonal production
HP   Horizontal production
HDP   Horizontal and diagonal production
BPR   Back pressure regulator
2D   Two-dimentional
3D   Three-dimentional
PV   Pore volumes
TMX   Transmission X-ray microscopy
DRIE   Deep-reactive ion etching